2012

Copper-Cobalt Catalysts for Conversion of Syngas to Ethanol and Higher Alcohols

Miranda Louise Smith
Louisiana State University and Agricultural and Mechanical College

COPPER-COBALT CATALYSTS FOR CONVERSION OF SYNGAS TO ETHANOL AND HIGHER ALCOHOLS

A Dissertation

Submitted to the Graduate Faculty of the
Louisiana State University and
Agricultural and Mechanical College
in partial fulfillment of the
requirements for the degree of
Doctor of Philosophy

in

The Gordon A. and Mary Cain Department of Chemical Engineering

by
Miranda Smith
B.S., Mississippi State University, 2008
August 2012

Acknowledgments

My parents have my deepest gratitude for their never-failing love, support, encouragement, and wisdom. Their faith in me and investment in my education have enabled me to progress thus far.

I also thank the educators at Lake Castle, Pope John Paul II High School, Mississippi State, and LSU who have instructed me over the years. In particular, I want to recognize Mrs. Arlene Romo, the best kindergarten teacher ever.

My advisor, Dr. Spivey, has been a constant source of sound guidance. When he is in the office, his door is always open, and no matter how busy he is, he finds time for his students. Thanks also to the committee members (Dr. Griffin, Dr. Flake, Dr. Stanley, Dr. Plummer, and Dr. Maverick) for their time and feedback.

I appreciate everyone at LSU who has helped make this work possible. Dr. Spivey's other students, past and present, have been my colleagues, collaborators, and friends. Paul Rodriguez and Joe Bell, along with their assistants in the chemical engineering machine shop, have worked miracles on my behalf on many occasions. Ellen Stevens has always been ready to help coordinate the financial aspects of my work.

The user facilities at CAMD and Oak Ridge National Laboratory have opened new opportunities for my research. The CAMD experiments were made possible by the assistance of Dr. Amitava Roy and Greg Merchan. Also, Dr. Andrew Campos kindly shared his experience with the *in situ* XANES setup. At ORNL, Dr. Viviane Schwartz and Dr. Andrew Payzant were helpful in preparing the *in situ* XRD experiments. In addition, Kimberly Hutchison (North

Carolina State University, Department of Soil Science) helpfully conducted ICP analysis of these catalysts.

Finally, I am grateful to the Louisiana Board of Regents for providing my fellowship, to the Chemical Engineering Department for additional support, and to the Center for Atomic Level Catalyst Design, an Energy Frontier Research Center sponsored by the U.S. Department of Energy, for funding this research.

Table of Contents

List of Tables

List of Figures

Abstract

Higher alcohols produced by catalytic conversion of synthesis gas are potential octane enhancers for transportation fuels. Copper-cobalt catalysts have emerged as alternatives to the ethanol-selective, but expensive, rhodium-based ones. The reducibility of the catalyst and the CO adsorption mode are important factors in directing the selectivity of CO hydrogenation toward methanol, hydrocarbons, or higher alcohols. In this study, Cu/SiO_2, Co/SiO_2, and bimetallic $CuCo/SiO_2$ catalysts, as well as their tin-promoted analogues, were synthesized and characterized by TPR, *in situ* XRD, *in situ* XANES, and *in situ* DRIFTS.

Cobalt addition to Cu/SiO_2 created an amorphous fraction of CuO that was more easily reducible than crystalline CuO. CO adsorption on copper sites, in terms of adsorption frequency and stability, was similar regardless of the presence or absence of cobalt. CO adsorbed on copper was thermally unstable, desorbing below typical CO hydrogenation temperatures. Copper addition to Co/SiO_2 increased reducibility of Co_3O_4, and to greater extent of the intermediate CoO, which in Co/SiO_2 was less readily reduced due to interaction with the support. In general, linearly adsorbed CO bound more strongly to the cobalt sites of $CuCo/SiO_2$ than of Co/SiO_2. Thus, on $CuCo/SiO_2$, CO could dissociate at the same sites where it also linearly adsorbed, leading to increased probability of CO insertion and ethanol formation. A second type of site on Co/SiO_2 was responsible for direct CO dissociation, leading to high activity and hydrocarbon selectivity on this catalyst, as well as faster deactivation.

The main effect of Sn addition was to increase dispersion of copper and cobalt on all the catalysts. This increased the reducibility of copper species and decreased that of cobalt species. On $CuCoSn/SiO_2$, copper promoted cobalt reduction, such that this catalyst was both well

reduced and highly dispersed. Sn addition increased the amount and stability of CO adsorbed on copper and cobalt sites of $CuCoSn/SiO_2$ and on copper sites of $CuSn/SiO_2$. However, the CO hydrogenation activity of the Sn-promoted catalysts decreased relative to the Sn-free catalysts. Fischer-Tropsch type chain growth became less favorable upon Sn addition, but CO insertion was still favored on $CuCoSn/SiO_2$, making this catalyst more ethanol-selective than $CuCo/SiO_2$.

Chapter 1: Introduction

1.1. Research Objectives

To study the roles of the two components in bimetallic copper-cobalt catalysts; to study the effect of tin addition to copper-cobalt catalysts. Properties to be considered include component reducibility and dispersion, CO adsorption, activity for CO hydrogenation, and selectivity to ethanol and C_{2+} oxygenates.

1.2. Engineering Relevance of Project

According to International Energy Outlook 2011 [1], published by the U.S. Energy Information Administration, global energy consumption is forecast to increase from 505 quadrillion Btu in 2008 to 619 quadrillion Btu in 2020, then to 770 quadrillion Btu in 2035—an increase of 53% over 27 years. Use of liquid fuels, specifically, is expected to rise from 85.7 million barrels per day in 2008 to 97.6 in 2020 and 112.2 in 2035. At the same time, production of unconventional liquid fuels is predicted to increase from 3.9 million barrels per day in 2008 to 13.1 million barrels per day in 2035, reaching 12% of the total liquids supply at that time.

1.3. Rationale for Studying Syngas Conversion to Ethanol and Higher Alcohols

One strategy for producing unconventional liquid fuels is catalytic reaction of syngas generated by reforming of natural gas or gasification of coal or biomass. Indeed, one advantage of this process is that it does not require any specific carbon feedstock [2,3]. Woody plants and grasses, which can be grown on marginal lands with little agricultural input by way of pesticides and fertilizers, can be used [4,5]. Even agricultural and forestry residues are acceptable [6,7]. This flexibility with respect to feedstock distinguishes the syngas route from, for example, fermentation of sugars from corn and sugar cane to yield bioethanol.

Syngas reactions lead to a variety of products, including CO_2, methane, Fischer-Tropsch hydrocarbons, and oxygenates. Of these products, the higher oxygenates (predominantly ethanol) are the main focus of this work.

As an additive to gasoline, ethanol increases the octane number and reduces emissions of CO, hydrocarbons, and particulates [8]. Despite having only about 68% of the energy content of gasoline per unit volume [8], ethanol increases the combustion *efficiency* of the fuel due its oxygen content [9,10]. Ethanol is fully miscible with gasoline but can be extracted by small amounts of water, leading to phase separation and corrosion. The presence of other higher alcohols, such as iso-propanol and 1-butanol, in the blend can help prevent this problem [9].

Due to its ease of transportation and storage, ethanol can also serve as a hydrogen carrier. Reforming and/or partial oxidation of ethanol at the point of use can supply hydrogen to power a fuel cell [11-17]. For example, steam reforming can provide up to 6 moles of H_2 per mole of ethanol. Direct ethanol fuel cells are also being explored [18,19].

In addition to these practical reasons for studying ethanol synthesis, the reaction is also interesting from a fundamental point of view. Though thermodynamically favorable, CO hydrogenation to ethanol (Equation 1.1) is less favorable than the methanation reaction (Equation 1.2).

$$2CO\ (g) + 4H_2\ (g) \rightarrow C_2H_5OH\ (g) + H_2O\ (g) \qquad (1.1)$$

$$\Delta H^\circ_r = -126.8\ \text{kJ/mol of CO reacted}$$

$$\Delta G^\circ_r = -110.6\ \text{kJ/mol of CO reacted}$$

$$CO\ (g) + 3H_2\ (g) \rightarrow CH_4\ (g) + H_2O\ (g) \qquad (1.2)$$

$$\Delta H^\circ_r = -205.9\ \text{kJ/mol of CO reacted}$$

$$\Delta G^\circ_r = -141.9\ \text{kJ/mol of CO reacted}$$

The selectivity to ethanol and higher alcohols is generally low due to competition from methanation and hydrocarbon formation. This is undoubtedly a major reason that the higher alcohol synthesis technology has not been commercially viable beyond the pilot scale [20]. In order to achieve high ethanol yield, methane formation must be kinetically limited, whereas sites that favor ethanol synthesis must be present on the catalyst. This will require a better understanding of the types of sites that catalyze formation of different products, from a mechanistic point of view.

1.4. Rationale for Selecting Copper-Cobalt Catalysts

Heterogeneous catalysts studied for conversion of syngas to oxygenates can be classified into four main types [21-23]: (1) rhodium-based catalysts, (2) copper-based modified methanol synthesis catalysts, (3) modified molybdenum-based catalysts, and (4) modified Fischer-Tropsch catalysts.

Rhodium-based catalysts, with appropriately chosen promoters, supports, and reaction conditions, are capable of producing ethanol with selectivities exceeding 30% [24-33]. Even so, net ethanol yields are typically too low to justify the use of the precious metal rhodium at the loadings required for these catalysts [34].

Copper-based catalysts, when promoted by alkali or other basic elements, produce mixtures of methanol, ethanol, propanol and branched alcohols like isobutanol [35-39]. These catalysts give low hydrocarbon selectivities (typically below 15%), but methanol is generally the principal oxygenate [35,39,40]. For these catalysts, ethanol is an intermediate, and its formation is the limiting step in the formation of C_{3+} alcohols [23,34,36,41-43]. That is, formation of the first C-C bond is the most difficult; subsequent conversion to propanol is more rapid.

Modified molybdenum-based catalysts, when promoted by alkali or transition metals, produce mainly linear alcohols and hydrocarbons [44-49]. In some cases the condensation of lower alcohols to form branched products is also observed [44,45]. These catalysts are sulfur-resistant and are often sulfided [44-48,50,51]. However, MoS_2-based catalysts require cofeeding of H_2S to maintain the sulfide state and stabilize the product distribution; this has the undesired effect of sulfur incorporation into the reaction products [52].

Modified Fischer-Tropsch catalysts typically contain Fe, Ru, Co, or Ni in combination with Cu, other transition metals, or rare earth oxides [53-60]. These catalysts give a mixture of linear alcohols and hydrocarbons, where methane is a major byproduct. Despite the high hydrocarbon selectivities of the modified Fischer-Tropsch catalysts, their high ethanol yields give an incentive to try to overcome this disadvantage [34]. In particular, the copper-cobalt family of catalysts favors high ethanol yield [61,62].

1.5. Rationale for Tin Addition to Copper-Cobalt Catalysts

Tin is a common promoter in transition metal catalysts for selective hydrogenation of the C=O bond in unsaturated carbonyl compounds [63-68]. The increased selectivity toward hydrogenation of the carbonyl group relative to the olefinic bond is due to enhanced adsorption at the carbonyl group upon tin addition. The possibility that tin might also promote adsorption of CO, favorably affecting the balance and interaction of CO, C, and CH_x surface species, has prompted the present investigation of tin addition to copper-cobalt catalysts.

1.6. Outline of the Dissertation

Chapter 1 provides the necessary background and context for conversion of syngas to ethanol and higher alcohols, including the rationale for studying this reaction and for focusing on

copper-cobalt catalysts. Justification is also offered for studying tin addition to the copper-cobalt system.

Chapter 2 summarizes work in the published literature dealing with syngas conversion to ethanol and higher alcohols, with emphasis on copper-cobalt catalysts. Prior findings on the mechanism and active sites are discussed, together with catalyst preparation, supports, and promoters.

Chapters 3-5 are written in journal style. **Chapter 3** has been published in a peer-reviewed journal [69] and discusses the reduction behavior of monometallic and bimetallic copper- and cobalt-based catalysts, as explored by temperature programmed reduction (TPR), *in situ* X-ray diffraction (XRD), and *in situ* X-ray absorption near edge structure (XANES). **Chapter 4**, also published in a peer-reviewed journal [70], deals with CO adsorption behavior of the same catalysts, particularly during exposure to syngas at elevated temperatures, and correlates the CO adsorption behavior with catalytic performance for CO hydrogenation. **Chapter 5** focuses on Sn addition to copper, cobalt, and copper-cobalt catalysts—specifically, on how Sn addition affects reduction behavior, dispersion, and CO adsorption of both copper and cobalt in each catalyst. This chapter has been submitted for review to *Catalysis Science & Technology*.

Chapter 6 summarizes the main conclusions of the original research presented in **Chapters 3-5** and recommends strategies for future work.

1.7. References

1. U.S. Department of Energy, E. I. A. 2011.
2. Digman, B.; Joo, H. S.; Kim, D.-S. *Environ. Prog. Sustainable Energy* **2009**, *28*, 47.
3. Wender, I. *Fuel Process. Technol.* **1996**, *48*, 189.

4. Hill, J.; Nelson, E.; Tilman, D.; Polasky, S.; Tiffany, D. *P. Natl. Acad. Sci. USA* **2006**, *103*, 11206.

5. Robbins, M. P.; Evans, G.; Valentine, J.; Donnison, I. S.; Allison, G. G. *Prog. Energy Combust. Sci.* **2012**, *38*, 138.

6. Kumar, A.; Jones, D. D.; Hanna, M. A. *Energies* **2009**, *2*, 556.

7. Ragauskas, A. J.; Williams, C. K.; Davison, B. H.; Britovsek, G.; Cairney, J.; Eckert, C. A.; Frederick, W. J.; Hallett, J. P.; Leak, D. J.; Liotta, C. L.; Mielenz, J. R.; Murphy, R.; Templer, R.; Tschaplinski, T. *Science* **2006**, *311*, 484.

8. Kumar, S.; Singh, N.; Prasad, R. *Renew. Sust. Energ. Rev.* **2010**, *14*, 1830.

9. Surisetty, V. R.; Dalai, A. K.; Kozinski, J. *Appl. Catal., A* **2011**, *404*, 1.

10. Lynd, L. R.; Cushman, J. H.; Nichols, R. J.; Wyman, C. E. *Science* **1991**, *251*, 1318.

11. Bshish, A.; Yakoob, Z.; Narayanan, B.; Ramakrishnan, R.; Ebshish, A. *Chem. Pap.* **2011**, *65*, 251.

12. Deluga, G. A.; Salge, J. R.; Schmidt, L. D.; Verykios, X. E. *Science* **2004**, *303*, 993.

13. Iulianelli, A.; Basile, A. *Catal. Sci. Technol.* **2011**, *1*, 366.

14. Haryanto, A.; Fernando, S.; Murali, N.; Adhikari, S. *Energy Fuels* **2005**, *19*, 2098.

15. Moharana, M. K.; Peela, N. R.; Khandekar, S.; Kunzru, D. *Renew. Sust. Energ. Rev.* **2011**, *15*, 524.

16. Ioannides, T. *J. Power Sources* **2001**, *92*, 17.

17. Zhang, B. C.; Tang, X. L.; Li, Y.; Cai, W. J.; Xu, Y. D.; Shen, W. J. *Catal. Commun.* **2006**, *7*, 367.

18. Wang, H. S.; Abruna, H. D. In *Fuel Cells and Hydrogen Storage*; Bocarsly, A., Mingos, D. M. P., Eds.; Springer: New York, 2011; Vol. 141, p 33.

19. Antolini, E. *J. Power Sources* **2007**, *170*, 1.

20. Fang, K.; Li, D.; Lin, M.; Xiang, M.; Wei, W.; Sun, Y. *Catal. Today* **2009**, *147*, 133.

21. Xiaoding, X.; Doesburg, E. B. M.; Scholten, J. J. F. *Catal. Today* **1987**, *2*, 125.

22. Kiennemann, A.; Boujana, S.; Diagne, C.; Chaumette, P.; Ichikawa, M.; Koerts, T.; Dejong, K. P. *Stud. Surf. Sci. Catal.* **1993**, *75*, 1479.

23. Spivey, J. J.; Egbebi, A. *Chem. Soc. Rev.* **2007**, *36*, 1514.

24. Arakawa, H.; Fukushima, T.; Ichikawa, M.; Natsushita, S.; Takeuchi, K.; Matsuzaki, T.; Sugi, Y. *Chem. Lett.* **1985**, 881.

25. Burch, R.; Hayes, M. J. *J. Catal.* **1997**, *165*, 249.

26. Hu, J. L.; Wang, Y.; Cao, C. S.; Elliott, D. C.; Stevens, D. J.; White, J. F. *Catal. Today* **2007**, *120*, 90.

27. van der Lee, G.; Schuller, B.; Post, H.; Favre, T. L. F.; Ponec, V. *J. Catal.* **1986**, *98*, 522.

28. Yu-hua, D.; De-An, C.; Khi-Rui, T. *Appl. Catal.* **1987**, *35*, 77.

29. Gronchi, P.; Tempesti, E.; Mazzocchia, C. *Appl. Catal., A* **1994**, *120*, 115.

30. Haider, M. A.; Gogate, M. R.; Davis, R. J. *J. Catal.* **2009**, *261*, 9.

31. Subramanian, N. D.; Gao, J.; Mo, X.; Goodwin, J. G., Jr.; Torres, W.; Spivey, J. J. *J. Catal.* **2010**, *272*, 204.

32. Yin, H. M.; Ding, Y. J.; Luo, H. Y.; Yan, L.; Wang, T.; Lin, L. W. *Energy Fuels* **2003**, *17*, 1401.

33. Yin, H. M.; Ding, Y. J.; Luo, H. Y.; Zhu, H. J.; He, D. P.; Xiong, J. M.; Lin, L. W. *Appl. Catal., A* **2003**, *243*, 155.

34. Subramani, V.; Gangwal, S. K. *Energy Fuels* **2008**, *22*, 814.

35. Bourzutschky, J. A. B.; Homs, N.; Bell, A. T. *J. Catal.* **1990**, *124*, 52.

36. Herman, R. G. *Catal. Today* **2000**, *55*, 233.

37. Apesteguia, C. R.; DeRites, B.; Miseo, S.; Soled, S. *Catal. Lett.* **1997**, *44*, 1.

38. Verkerk, K. A. N.; Jaeger, B.; Finkeldei, C. H.; Keim, W. *Appl. Catal., A* **1999**, *186*, 407.

39. Xu, M. T.; Gines, M. J. L.; Hilmen, A. M.; Stephens, B. L.; Iglesia, E. *J. Catal.* **1997**, *171*, 130.

40. Hilmen, A. M.; Xu, M. T.; Gines, M. J. L.; Iglesia, E. *Appl. Catal., A* **1998**, *169*, 355.

41. Nunan, J. G.; Bogdan, C. E.; Klier, K.; Smith, K. J.; Young, C. W.; Herman, R. G. *J. Catal.* **1989**, *116*, 195.

42. Smith, K. J.; Anderson, R. B. *J. Catal.* **1984**, *85*, 428.

43. Klier, K.; Beretta, A.; Sun, Q.; Feeley, O. C.; Herman, R. G. *Catal. Today* **1997**, *36*, 3.

44. Bian, G. Z.; Fan, L.; Fu, Y. L.; Fujimoto, K. *Appl. Catal., A* **1998**, *170*, 255.

45. Bian, G. Z.; Fan, L.; Fu, Y. L.; Fujimoto, K. *Ind. Eng. Chem. Res.* **1998**, *37*, 1736.

46. Gunturu, A. K.; Kugler, E. L.; Cropley, J. B.; Dadyburjor, D. B. *Ind. Eng. Chem. Res.* **1998**, *37*, 2107.

47. Lee, J. S.; Kim, S.; Lee, K. H.; Nam, I. S.; Chung, J. S.; Kim, Y. G.; Woo, H. C. *Appl. Catal., A* **1994**, *110*, 11.

48. Liu, Z. Y.; Li, X. G.; Close, M. R.; Kugler, E. L.; Petersen, J. L.; Dadyburjor, D. B. *Ind. Eng. Chem. Res.* **1997**, *36*, 3085.

49. Xiang, M.; Li, D.; Xiao, H.; Zhang, J.; Li, W.; Zhong, B.; Sun, Y. *Catal. Today* **2008**, *131*, 489.

50. Li, X. G.; Feng, L. J.; Liu, Z. Y.; Zhong, B.; Dadyburjor, D. B.; Kugler, E. L. *Ind. Eng. Chem. Res.* **1998**, *37*, 3853.

51. Li, Z. R.; Fu, Y. L.; Jiang, M. *Appl. Catal., A* **1999**, *187*, 187.

52. Christensen, J. M.; Mortensen, P. M.; Trane, R.; Jensen, P. A.; Jensen, A. D. *Appl. Catal., A* **2009**, *366*, 29.

53. Takeuchi, K.; Matsuzaki, T.; Arakawa, H.; Sugi, Y. *Appl. Catal.* **1985**, *18*, 325.

54. Hamada, H.; Kuwahara, Y.; Kintaichi, Y.; Ito, T.; Wakabayashi, K.; Iijima, H.; Sano, K. *Chem. Lett.* **1984**, 1611.

55. Kintaichi, Y.; Kuwahara, Y.; Hamada, H.; Ito, T.; Wakabayashi, K. *Chem. Lett.* **1985**, 1305.

56. Razzaghi, A.; Hindermann, J. P.; Kiennemann, A. *Appl. Catal.* **1984**, *13*, 193.

57. Inoue, M.; Miyake, T.; Takegami, Y.; Inui, T. *Appl. Catal.* **1984**, *11*, 103.

58. Fujimoto, K.; Oba, T. *Appl. Catal.* **1985**, *13*, 289.

59. Kiennemann, A.; Barama, A.; Boujana, S.; Bettahar, M. M. *Appl. Catal., A* **1993**, *99*, 175.

60. Zhao, N.; Xu, R.; Wei, W.; Sun, Y. H. *React. Kinet. Catal. Lett.* **2002**, *75*, 297.

61. Stiles, A. B.; Chen, F.; Harrison, J. B.; Hu, X. D.; Storm, D. A.; Yang, H. X. *Ind. Eng. Chem. Res.* **1991**, *30*, 811.

62. Hutchings, G. J. *S. Afr. J. Chem.* **1986**, *39*, 65.

63. Riguetto, B. A.; Rodrigues, C. E. C.; Morales, M. A.; Baggio-Saitovitch, E.; Gengembre, L.; Payen, E.; Marques, C. M. P.; Bueno, J. M. C. *Appl. Catal., A* **2007**, *318*, 70.

64. Margitfalvi, J. L.; Tompos, A.; Kolosova, I.; Valyon, J. *J. Catal.* **1998**, *174*, 246.

65. Margitfalvi, J. L.; Vankó, G.; Borbáth, I.; Tompos, A.; Vértes, A. *J. Catal.* **2000**, *190*, 474.

66. Pouilloux, Y.; Autin, F.; Guimon, C.; Barrault, J. *J. Catal.* **1998**, *176*, 215.

67. Ferretti, O. A.; Bournonville, J. P.; Mabilon, G.; Martino, G.; Candy, J. P.; Basset, J. M. *J. Mol. Catal.* **1991**, *67*, 283.

68. Vicente, A.; Lafaye, G.; Especel, C.; Marecot, P.; Williams, C. T. *J. Catal.* **2011**, *283*, 133.

69. Smith, M. L.; Campos, A.; Spivey, J. J. *Catal. Today* **2012**, *182*, 60.

70. Smith, M. L.; Kumar, N.; Spivey, J. J. *J. Phys. Chem. C* **2012**, *116*, 7931.

Chapter 2: Literature Review of Copper-Cobalt Catalysts for Higher Alcohol Synthesis

2.1. Historical Context

Copper-cobalt catalysts for CO hydrogenation to ethanol and higher alcohols came to prominence in the 1980s. Early work focused on identification of the mechanism and active sites, along with understanding the roles of the components. Meanwhile, research also gradually turned to such topics as the roles of promoters and supports, and the influence of reaction conditions on catalytic performance. More recently, work has focused on controlling particle size and structure during catalyst synthesis.

2.2. Mechanism of Higher Alcohol Synthesis over Copper-Cobalt Catalysts

A generalized mechanism of higher alcohol synthesis on modified Fischer-Tropsch catalysts is shown in Figure 2.1 [1,2]. According to this scheme, higher alcohols form via acyl or carboxylate intermediates when a C_1 oxygenated species (CO, formyl, or formate) is inserted into a surface hydrocarbon group. The mechanism also accounts for the formation of methanol (by direct hydrogenation of the C_1 oxygenate entity), of methane (by hydrogenation of CH_x formed after dissociative adsorption of CO), and of hydrocarbons (by chain growth and hydrogenation). The carbon number of the higher alcohols formed also depends on this chain growth step.

This mechanism has been supported by chemical trapping studies on copper-cobalt-aluminum-zinc-sodium catalysts [3]. These studies show, for example, that addition of dichloromethane or dichloroethane to the syngas reaction leads to increased ethanol or propanol levels, respectively, due to scavenging of C_1 oxygenate surface species. Coupling of methanol, formaldehyde, or formic acid with diiodomethane or dichloromethane also yields ethanol.

Reaction of the same C_1 oxygenates with dichloroethane yields propanol and propanal. However, coupling of C_2 oxygenates with dichloromethane or diiodomethane does not lead to propanol or propanal. These experiments demonstrate that higher alcohols form by addition of a C_1 oxygenate to a hydrocarbon chain, not addition of a C_1 hydrocarbon to an oxygenate chain.

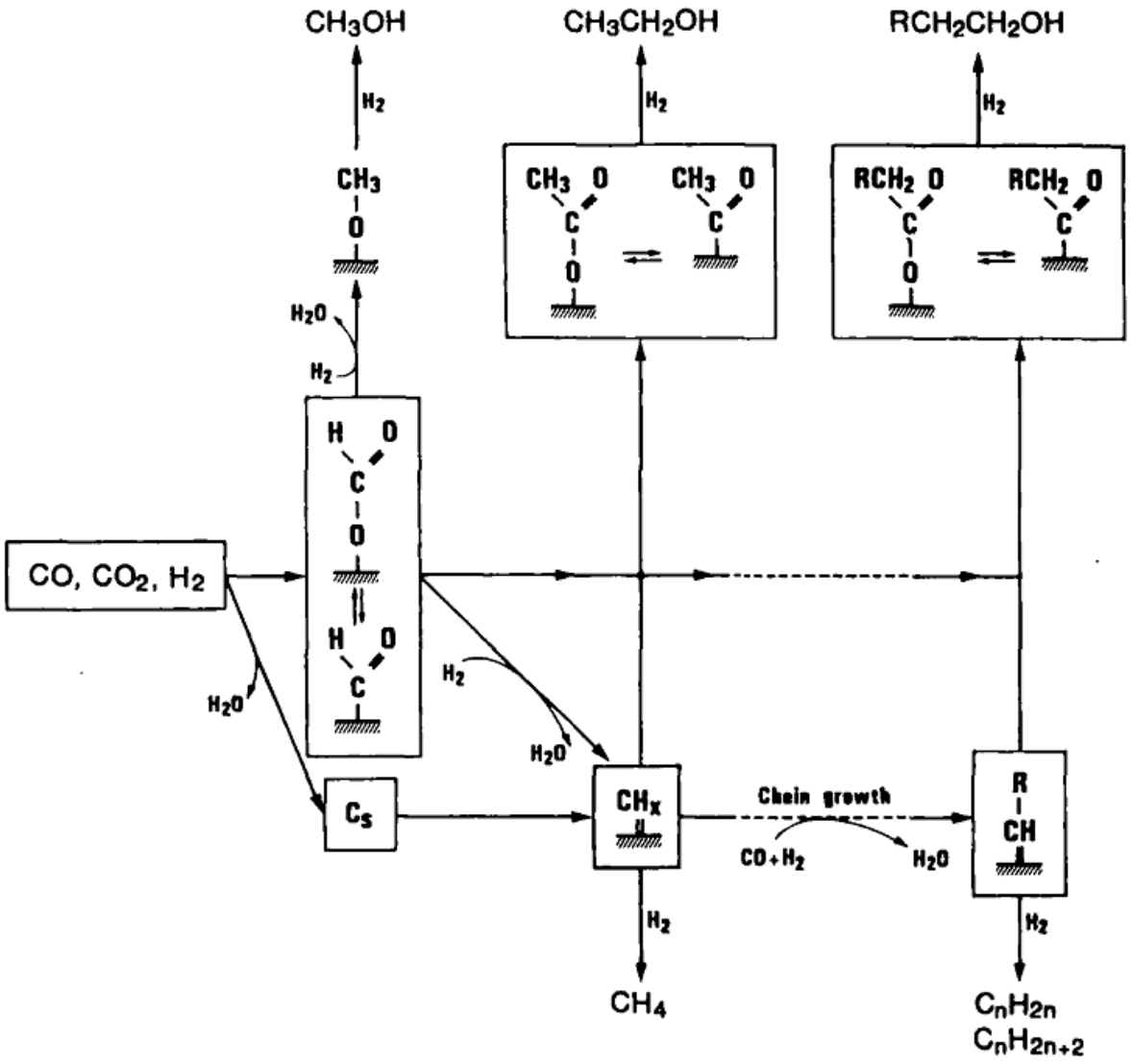

Figure 2.1. Mechanism of higher alcohol synthesis on copper-cobalt catalysts [1,2]. Reprinted with permission from (Chaumette, P.; Courty, P.; Kiennemann, A.; Kieffer, R.; Boujana, S.; Martin, G. A.; Dalmon, J. A.; Meriaudeau, P.; Mirodatos, C.; Holhein, B.; Mausbeck, D.; Hubert, A. J.; Germain, A.; Noels, A. *Ind. Eng. Chem. Res.* **1994**, *33*, 1460). Copyright (1994) American Chemical Society.

Pathways to higher alcohols based on homologation or condensation of lower alcohols do not appear to operate to a significant extent on copper-cobalt catalysts. Cofeeding methanol with syngas either does not significantly increase the ethanol concentration in the products [4] or increases it to a lesser extent than the isobutanol concentration [3]. The latter product is known to form by β-addition condensation pathways over alkali-promoted Cu/ZnO catalysts [5-7]. Without the added methanol, however, the alcohols produced by copper-cobalt catalysts are mostly of the linear, primary variety. Similarly, cofeeding of ethanol with syngas results in condensation or homologation products only when the ethanol concentration is much larger than can be produced under normal reaction conditions [4]. According to another study, ethanol cofeeding enhances higher alcohol synthesis most effectively on a CuZnCr catalyst; increasing cobalt content from 0 to 5 mol% in this formulation decreases both conversion of ethanol and yield of higher alcohols [8].

The evidence suggests that mechanisms based on incorporation of lower alcohols into higher ones, while not impossible on copper-cobalt catalysts, are unlikely to be major contributors to higher alcohol synthesis under normal conditions. The mechanism in Figure 2.1 is more consistent with the typical product spectrum from these catalysts—that is, a Schulz-Flory distribution of both alcohols and hydrocarbons.

2.3. Active Sites

Considering the wide array of products made possible by the mechanism in Figure 2.1, identification of the site or sites responsible for ethanol formation is a challenge. Indeed, much debate has centered on this problem in the literature.

One early model [9] included a cobalt core surrounded by a copper-cobalt alloy shell, despite the low solubility of copper in cobalt (about 10%). The cobalt sites of the alloy were

assumed to dissociate CO and grow the carbon chain, while the copper sites were thought to adsorb molecular CO and insert it into the metal-alkyl bond.

A contemporaneous report [10] showing that alcohols could be produced by a cobalt catalyst without copper in the formulation raised questions about the role of copper as the CO insertion site. Copper-cobalt alloy catalysts were found by some to be less active for oxygenate synthesis than partially reduced cobalt [11,12]. These studies proposed cobalt ions as the active sites for CO insertion and suggested the role of copper was to moderate the hydrogenation activity of cobalt so as to suppress hydrocarbon formation [12].

Other researchers [2,13] have suggested that bimetallic sites are more suitable for higher alcohol formation than ionic species, while acknowledging that the latter sites might possibly play a role. Of course, the existence of a strong copper-cobalt interaction does not preclude reoxidation of the metals to Co^{2+} and Cu^{+} or $Cu^{\delta+}$ during the reaction, which has in fact been observed [14].

The temperature range of higher alcohol synthesis has been sometimes observed to coincide with the existence of a cobalt carbide phase [15,16]. This suggested that the copper-cobalt alloy phase generated upon reduction served to promote formation of cobalt carbide, which then functioned as the CO insertion site. Metallic sites were responsible for CO dissociation. Similarly, the high activity, ethanol selectivity, and stability of perovskite-derived Co-Cu/La_2O_3-$LaFeO_3$ catalysts have been attributed to formation of highly dispersed Co_2C during the reaction [17].

Oxygenate production has also been correlated with increasing dispersion of metallic copper supported on a cobalt-containing spinel [18]. This result was attributed to electronic modification of copper through contact with the potassium-promoted cobalt-chromium spinel.

Active sites consisting of isolated cobalt atoms on metallic copper clusters have also been proposed. The tendency of such sites to adsorb multiple CO molecules was recognized on a CuCoZnAl catalyst and could lead to enhanced CO insertion [19].

Different studies disagree as to whether the chain growth probability factors (α) for hydrocarbons and alcohols are equal [20] or different [4]. Equal α's would imply a common site for hydrocarbon and alcohol formation. Boz [21] observed an alcohol α that was constant with respect to conversion and a decreasing hydrocarbon α that converged to the alcohol value at high conversion (Figure 2.2). One plausible explanation is that there are two types of sites for hydrocarbon formation, one of which becomes less active at high conversions. On the other hand, there is only one type of site for alcohol synthesis, a point later reiterated by Mahdavi et al. [22].

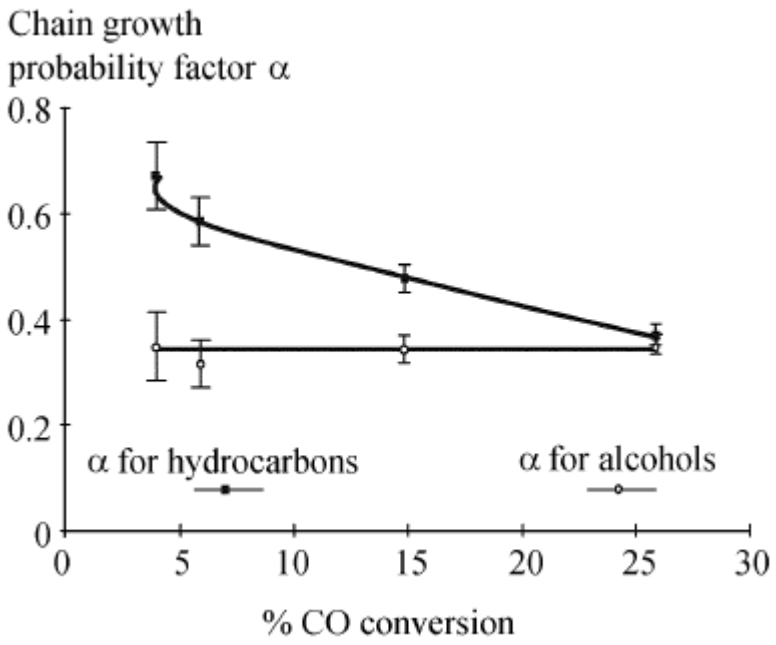

Figure 2.2. Changes in chain growth probability factor α with CO conversion over a $Co_2O_3/CuO/ZnO/Al_2O_3$+5% K_2O catalyst [21] (with kind permission from Springer Science and Business Media).

The determination of the active sites is further complicated by differing catalyst compositions in different studies. For example, when the copper-to-cobalt ratio is high, cobalt can act as a selective poison of methanol and/or higher alcohol synthesis at copper sites [23-25]. Only as its concentration increases does cobalt contribute to chain growth and higher alcohol synthesis (Figure 2.3) [26,27].

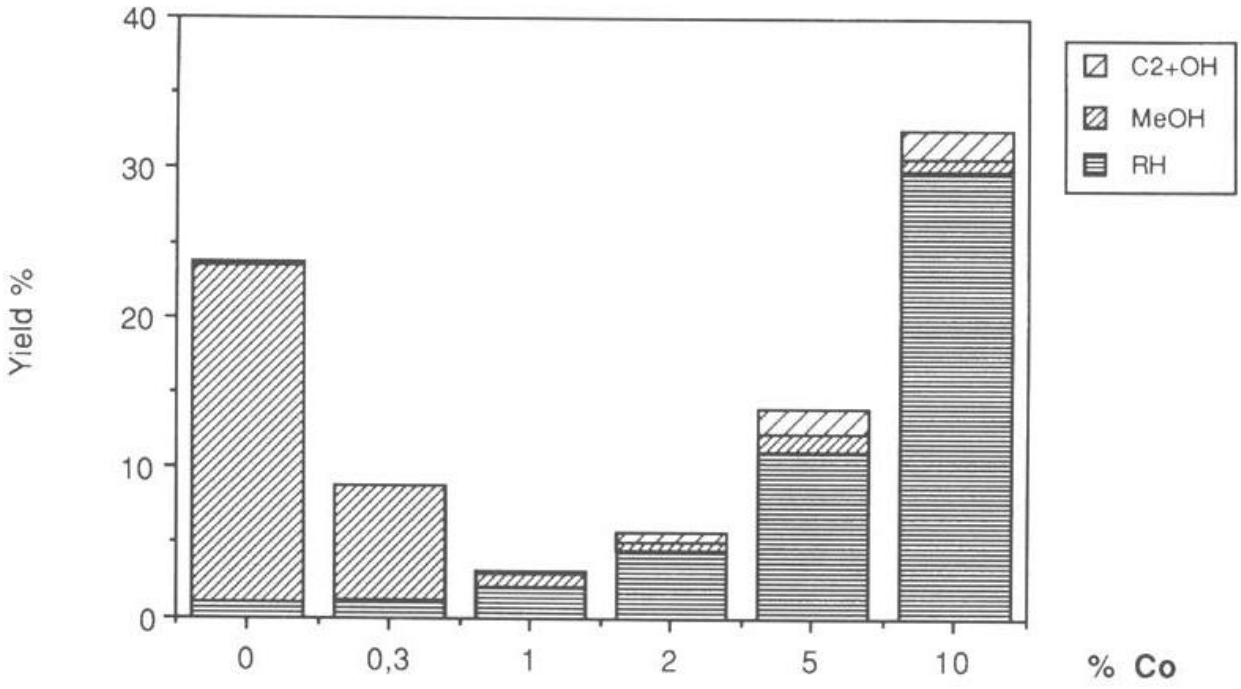

Figure 2.3. Promotional effect of Co on a $CuLa_2Zr_2O_7$ catalyst. Catalyst: x% Co/40% $CuLa_2Zr_2O_7$, calcined for 3 h at 700°C. Reaction conditions: CO + $2H_2$, gas flow 4 1 h^{-1} g_{cat}^{-1}, P = 6 MPa, T= 280°C [27]. Reprinted from Chu, W.; Kieffer, R.; Kiennemann, A.; Hindermann, J. P. *Appl. Catal., A* **1995**, *121*, 95, with permission from Elsevier.

In summary, a wide variety of sites have been proposed as having some involvement in the synthesis of ethanol and higher alcohols. These include copper-cobalt alloys, unalloyed but still interacting copper and cobalt metals, metallic cobalt interacting with cobalt ions, ionic copper and cobalt, cobalt carbide interacting with a metallic phase, dispersed copper supported on a cobalt-containing spinel, and cobalt atoms supported on copper clusters. In addition, the sites for hydrocarbon and alcohol formation may or may not be the same, depending on the reaction conditions.

2.4. Catalyst Preparation

Whatever the active sites of higher alcohol synthesis on copper-cobalt catalysts may be, their selective generation depends in part on the synthesis conditions. A number of papers dealing exclusively with the synthesis and conditioning of copper-cobalt materials have been published [28-35].

In addition, the effect of preparation parameters on catalytic performance has been investigated. For example, SiO_2-supported, co-impregnated catalysts have outperformed sequentially impregnated ones in terms of selectivity and space time yield to C_{2+} alcohols [36]. This result was ascribed to a stronger synergistic effect between copper and cobalt in the co-impregnated catalyst. Coprecipitated or citrate-derived CuCoAlZn catalysts were more active when calcined in oxygen or air than in nitrogen [37,38]. Calcination temperature is another important variable, which if too high leads to catalysts with reduced activity and high hydrocarbon selectivity [39,40]. An excessive calcination temperature reduces the active metal surface area [40] and preferentially destroys oxygenate-producing sites [39].

A recent trend in research on copper-cobalt catalysts has been the attempt, through advanced synthesis procedures or preparation of defined crystalline structures, to improve the dispersion or distribution of active materials in the catalysts.

For example, reactive grinding of lanthanum, copper, and cobalt oxides has been used to generate precursors with copper and cobalt atoms uniformly distributed in a perovskite lattice, which upon reduction transform to highly dispersed bimetallic Co-Cu alloys supported on La_2O_3 [41-43]. Increasing copper content in the original perovskite lattice was found to increase higher alcohol selectivity [41,44].

Other techniques have included post-treatment of coprecipitated or co-impregnated catalysts by glow discharge plasma [45-47], as well as reverse coprecipitation under ultrasound irradiation [45]. The plasma treatment increased the dispersion, specific surface area, surface content of active components, and CO adsorption capacity of the catalysts. It also increased CO conversion, alcohol yield, and C_{2+} alcohol selectivity. In the reverse coprecipitation procedure, an aqueous solution of catalyst precursors was added to the Na_2CO_3 precipitating solution under ultrasound irradiation. Compared to a conventionally coprecipitated catalyst, prepared by feeding the precursor solution and precipitating solution together into a beaker, the catalyst synthesized by reverse coprecipitation showed increased dispersion, surface area, surface enrichment of copper and cobalt, CO conversion, and C_{2+} alcohol selectivity.

Catalysts prepared by impregnation of bimetallic copper-cobalt complexes have also been studied [48,49]. For example, impregnation of a bimetallic cyanide complex onto alumina resulted in a catalyst with higher C_{2+} alcohol selectivity than one prepared by impregnation of nitrates [49]. This was attributed to a close interaction between copper and cobalt, originating from the precursor used. The high dispersion of cobalt might also be important for higher alcohol selectivity [48].

The use of pyrogallol as a complexing agent in the impregnation of copper and cobalt nitrates onto carbon nanotube (CNT)-modified silica gel has been shown to preferentially deposit metal ions onto the CNTs [50]. The resulting increases in CO conversion and C_{2+} alcohol selectivity (compared to catalysts prepared by aqueous impregnation of unmodified and CNT-modified silica gel) were attributed to improved distribution and interaction of copper and cobalt.

Subramanian et al. [51,52] prepared copper-cobalt nanoparticles with both core-shell and mixed-metal morphologies. The mixed-metal nanoparticles gave higher selectivity to ethanol

than ones with a cobalt core and copper shell [51]. However, nanoparticles with a copper core and cobalt shell gave still higher ethanol selectivity [52].

Though the advanced synthesis techniques allow some manipulation of catalyst structure, they also present some disadvantages. For example, some use nonstandard reagents and precursors that have to be specially prepared for this purpose [48,49]. Others give relatively low throughput, as only a few hundred milligrams of catalyst can be produced at one time. The catalysts discussed in this work have been prepared according to standard incipient wetness impregnation methods. The goal is to find ways to achieve high dispersion and favorable metals distribution without resorting to exotic synthesis techniques—e.g., through the choice of suitable supports and promoters.

2.5. Supports

Catalyst supports generally serve to stabilize the active species, modify their dispersion and reducibility, and sometimes facilitate electron transfer [53]. Only a couple of studies discuss support effects specific to copper-cobalt catalysts (some of which are listed in Table 2.1).

Mouaddib et al. [54,55] observed different product selectivities during CO hydrogenation when copper and cobalt were deposited on different supports. MgO favored methanol selectivity. TiO_2, CeO_2, and La_2O_3 led to hydrocarbons. These four supports gave C_{2+} alcohol selectivities of 8-15%. SiO_2 and ZrO_2 improved higher alcohol selectivity to values of 25-30%. The authors attributed the different selectivities to different surface compositions induced by the supports. The CeO_2-supported catalyst, for example, had a cobalt-rich surface, which led to hydrocarbons. The surface enrichment of copper on the MgO-supported catalyst led to its high methanol selectivity. The ZrO_2-supported catalyst, which was selective to higher alcohols, had a surface composed of both metals.

Table 2.1. Comparison of activities and selectivities of copper-cobalt catalysts on different supports [55,56]. Numbers in parentheses represent ethanol selectivities. Where the sum of selectivities < 100%, CO_2 makes up the balance.

		SiO_2	ZrO_2	TiO_2	MgO	La_2O_3
Ref. [55].	Temperature (°C)	250	250	250	250	250
	Activity (mmol/h/g_{cat})	0.44	1.39	3.37	0.79	0.63
	Selectivity					
	C_{2+} oxygenates	29	25	13	10	8
	MeOH	37	39	12	76	35
	Hydrocarbons	34	36	75	14	57
Ref. [56].	Temperature (°C)	280	280	250	250	280
	CO Conversion (%)	0.6	18.0	0.7	0.6	1.9
	Selectivity					
	C_{2+} oxygenates	21 (21)	16 (9)	24 (16)	36 (31)	25 (19)
	MeOH	38	3	15	20	26
	Hydrocarbons	42	77	55	44	48

Takeuchi et al. [56] studied the effect of support on Cu-Co-Zn catalysts. Cr_2O_3 and ZnO led to high selectivities toward methanol and CO_2. The highest conversions were obtained at 280°C from the catalysts supported on Al_2O_3 (31%) and ZrO_2 (18%), but these catalysts favored hydrocarbons and gave ethanol selectivities <10%. TiO_2 and La_2O_3 gave increased ethanol

selectivities of 16% and 19% at 250°C and 280°C, respectively. Catalysts supported on MgO or SiO_2 gave the highest ethanol selectivities, exceeding 20%.

The two studies are not in perfect agreement as to the effect of the various supports. For example, MgO leads predominantly to methanol according to Mouaddib et al. [55] but to ethanol according to Takeuchi et al. [56] However, both studies agree that SiO_2 is relatively effective at promoting higher oxygenate selectivity. This is one reason SiO_2 has been selected as the support for the catalysts in the present study.

2.6. Promoters

The most common promoters added to copper-cobalt catalysts are the alkali elements. Alkali cations suppress methanation [20,21,39,57,58] and alcohol dehydration [20]. Suppressed methanation could be due to a reduction in hydrogenation activity of cobalt, which would tend to stabilize CH_x species on the surface and increase the probability of their incorporation into higher molecular weight compounds [21,57,58]. In addition, alkali ions can promote adsorption of CO by interacting with its O atom as in Figure 2.4 [13,21,59] or by stabilizing cobalt carbonyl species [13]. Higher alcohol yield usually exhibits a maximum with increasing alkali loading [21,57], which could indicate blockage of active sites when the promoter is present in excess. Alkalization has the side effect of promoting carbon deposition [13,60,61]. In addition, water vapor, a reaction byproduct is capable of extracting the alkali elements [61].

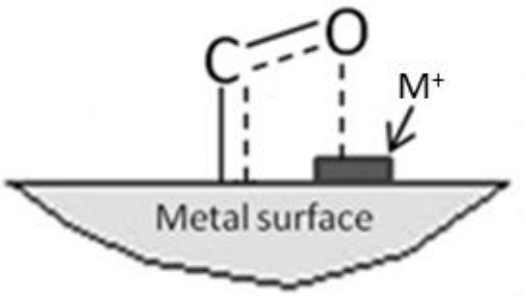

Figure 2.4. CO adsorption on a metal surface and interaction with a cationic promoter.

Zinc is another common ingredient in copper-cobalt catalyst formulations. Zinc is said to improve catalyst stability and decrease carbon deposition [13].

Certain other promoters—including manganese and molybdenum—have also been studied. Manganese decreases overall catalytic activity but promotes selectivity to higher alcohols, particularly n-propanol [62]. Molybdenum addition to copper-cobalt catalysts increases overall activity and alcohol yield [27,63]. This result has been attributed to increased hydrogen adsorption and hydrogenating power upon addition of molybdenum oxides [27]. Due to the altered hydrogenating power, however, the higher-alcohol-to-methanol ratio decreases. The effect of molybdenum is most beneficial when it is combined with copper and cobalt in a mixed phase [64].

Promotion of a copper-cobalt catalyst by herringbone-type CNTs is also reported to increase the concentration of adsorbed hydrogen, increasing the rate of surface hydrogenation reactions and overall catalytic activity [65,66]. The simultaneous increase in higher alcohol selectivity is explained by the stabilization of CoO(OH) species, which is the active cobalt species according to these authors.

Other potential promoters, even those frequently added to catalysts employed for related reactions, have yet to be studied for higher alcohol synthesis. For example, tin is known to enhance C=O group adsorption [67-72] and might be expected to do the same for the CO molecule. This would influence the quantity of associatively and dissociatively adsorbed CO and might increase selectivity toward CO insertion. In fact, the activation of the carbonyl group is often proposed to occur via interaction of its O atom with positively charged tin [68-70]. A similar interaction of CO with an oxophilic site gives rise to a tilted CO species (as in Figure 2.4), which is thought to favor both CO dissociation (by favoring surface bonding via C and O atoms) and insertion (by stabilizing acyl intermediates) on Rh catalysts and others [73-75].

2.7. Other Applications of Copper-Cobalt Catalysts

Besides the higher-alcohol synthesis, copper-cobalt catalysts have also been studied for such reactions as dehydrogenation of cyclohexanol [76], methyl acetate hydrogenolysis [77], and hydrogenation of unsaturated aldehydes to the corresponding alcohols [78,79]. The latter reaction is most relevant to this study and, interestingly, is one for which Sn promotion has been found to be beneficial.

2.8. Current Research Priorities

Though extensive research has been conducted on the identification of the active sites of copper-cobalt catalysts, most of this work has been done without the benefit of *in situ* spectroscopic techniques. For example, X-ray absorption and infrared spectroscopies have given valuable insights into the hydrogen reduction [80,81] and CO adsorption during syngas exposure [82] of cobalt-based Fischer-Tropsch catalysts. However, similar studies on copper-cobalt higher-alcohol synthesis catalysts are lacking. From the literature reviewed in the preceding sections, the nature of the CO insertion site (whether metallic or cationic) is debatable. Furthermore, the mode of CO adsorption—the balance of associatively and dissociatively adsorbed species, and the type of site associated with each—is crucial to higher alcohol selectivity. Therefore, detailed studies using *in situ* probes have been undertaken with the goal of relating these attributes to the activity and selectivity of the catalysts.

In addition, Sn has been explored as an alternative to alkali, zinc, manganese, and molybdenum promoters. In an effort to identify component interactions and synergisms, one-, two-, and three-component catalysts have been synthesized and characterized: Cu/SiO_2, Co/SiO_2, $CuCo/SiO_2$, $CuSn/SiO_2$, $CoSn/SiO_2$, and $CuCoSn/SiO_2$.

2.9. References

1. Chaumette, P.; Courty, P.; Kiennemann, A.; Ernst, B. *Top. Catal.* **1995**, *2*, 117.

2. Chaumette, P.; Courty, P.; Kiennemann, A.; Kieffer, R.; Boujana, S.; Martin, G. A.; Dalmon, J. A.; Meriaudeau, P.; Mirodatos, C.; Holhein, B.; Mausbeck, D.; Hubert, A. J.; Germain, A.; Noels, A. *Ind. Eng. Chem. Res.* **1994**, *33*, 1460.

3. Kiennemann, A.; Diagne, C.; Hindermann, J. P.; Chaumette, P.; Courty, P. *Appl. Catal.* **1989**, *53*, 197.

4. Pan, W. X.; Cao, R.; Griffin, G. L. *J. Catal.* **1988**, *114*, 447.

5. Nunan, J. G.; Bogdan, C. E.; Klier, K.; Smith, K. J.; Young, C. W.; Herman, R. G. *J. Catal.* **1989**, *116*, 195.

6. Smith, K. J.; Anderson, R. B. *J. Catal.* **1984**, *85*, 428.

7. Smith, K. J.; Young, C. W.; Herman, R. G.; Klier, K. *Ind. Eng. Chem. Res.* **1991**, *30*, 61.

8. Calafat, A.; Laine, J. *J. Catal.* **1994**, *147*, 88.

9. Bailliard-Letournel, R. M.; Cobo, A. J. G.; Mirodatos, C.; Primet, M.; Dalmon, J. A. *Catal. Lett.* **1989**, *2*, 149.

10. Blanchard, M.; Derule, H.; Canesson, P. *Catal. Lett.* **1989**, *2*, 319.

11. Baker, J. E.; Burch, R.; Hibble, S. J.; Loader, P. K. *Appl. Catal.* **1990**, *65*, 281.

12. Baker, J. E.; Burch, R.; Niu, Y. Q. *Appl. Catal.* **1991**, *73*, 135.

13. Dalmon, J. A.; Chaumette, P.; Mirodatos, C. *Catal. Today* **1992**, *15*, 101.

14. Chu, W.; Xiong, G. X.; Chen, H. R.; Sheng, S. S.; Guo, X. X. *React. Kinet. Catal. Lett.* **1995**, *56*, 331.

15. Volkova, G. G.; Krieger, T. A.; Plyasova, L. M.; Zaikovskii, V. A.; Yurieva, T. M. *Stud. Surf. Sci. Catal.* **1997**, *107*, 67.

16. Volkova, G. G.; Yurieva, T. M.; Plyasova, L. M.; Naumova, M. I.; Zaikovskii, V. I. *J. Mol. Catal. A: Chem.* **2000**, *158*, 389.

17. Fang, Y. Z.; Liu, Y.; Zhang, L. H. *Appl. Catal., A* **2011**, *397*, 183.

18. Sheffer, G. R.; Jacobson, R. A.; King, T. S. *J. Catal.* **1989**, *116*, 95.

19. Cao, R.; Pan, W. X.; Griffin, G. L. *Langmuir* **1988**, *4*, 1108.

20. Courty, P.; Durand, D.; Freund, E.; Sugier, A. *J. Mol. Catal.* **1982**, *17*, 241.

21. Boz, I. *Catal. Lett.* **2003**, *87*, 187.

22. Mahdavi, V.; Peyrovi, M. H.; Islami, M.; Mehr, J. Y. *Appl. Catal., A* **2005**, *281*, 259.

23. Wang, J.; Oukaci, R.; Wender, I.; Blackmond, D. G. *J. Catal.* **1995**, *153*, 100.

24. Elliott, D. J.; Pennella, F. *J. Catal.* **1986**, *102*, 464.

25. Elliott, D. J. *J. Catal.* **1988**, *111*, 445.

26. Courty, P.; Chaumette, P.; Raimbault, C.; Travers, P. *Rev. Inst. Fr. Pet.* **1990**, *45*, 561.

27. Chu, W.; Kieffer, R.; Kiennemann, A.; Hindermann, J. P. *Appl. Catal., A* **1995**, *121*, 95.

28. Di Cosimo, J. I.; Apesteguía, C. R. *J. Catal.* **1989**, *116*, 71.

29. Fierro, G.; Lo Jacono, M.; Inversi, M.; Dragone, R.; Porta, P. *Top. Catal.* **2000**, *10*, 39.

30. Marchi, A. J.; Dicosimo, J. I.; Apesteguia, C. R. *Catal. Today* **1992**, *15*, 383.

31. Marchi, A. J.; Apesteguia, C. R. *Appl. Clay Sci.* **1998**, *13*, 35.

32. Li, G. H.; Dai, L. Z.; Lu, D. S.; Peng, S. Y. *J. Solid State Chem.* **1990**, *89*, 167.

33. Velu, S.; Suzuki, K.; Hashimoto, S.; Satoh, N.; Ohashi, F.; Tomura, S. *J. Mater. Chem.* **2001**, *11*, 2049.

34. Morpurgo, S.; Lojacono, M.; Porta, P. *J. Mater. Chem.* **1994**, *4*, 197.

35. Porta, P.; Morpurgo, S.; Pettiti, I. *J. Solid State Chem.* **1996**, *121*, 372.

36. Deng, S. Y.; Chu, W.; Xu, H. Y.; Shi, L. M.; Huang, L. H. *J. Nat. Gas Chem.* **2008**, *17*, 369.

37. Baker, J. E.; Burch, R.; Golunski, S. E. *Appl. Catal.* **1989**, *53*, 279.

38. Di Cosimo, J. I.; Marchi, A. J.; Apesteguia, C. R. *J. Catal.* **1992**, *134*, 594.

39. Sheffer, G. R.; King, T. S. *Appl. Catal.* **1988**, *44*, 153.

40. Mahdavi, V.; Peyrovi, M. H. *Catal. Commun.* **2006**, *7*, 542.

41. Tien-Thao, N.; Alamdari, H.; Zahedi-Niaki, M. H.; Kaliaguine, S. *Appl. Catal., A* **2006**, *311*, 204.

42. Nguyen, T. T.; Zahedi-Niaki, M. H.; Alamdari, H.; Kaliaguine, S. *Int. J. Chem. React. Eng.* **2007**, *5*.

43. Tien-Thao, N.; Zahedi-Niaki, M. H.; Alamdari, H.; Kaliaguine, S. *Appl. Catal., A* **2007**, *326*, 152.

44. Tien-Thao, N.; Alamdari, H.; Kaliaguine, S. *J. Solid State Chem.* **2008**, *181*, 2006.

45. Shi, L. M.; Chu, W.; Deng, S. Y.; Xu, H. Y. *J. Nat. Gas Chem.* **2008**, *17*, 397.

46. Xu, H.-y.; Chu, W.; Shi, L.-m.; Zhang, H.; Deng, S.-y. *J. Fuel Chem. Technol.* **2009**, *37*, 212.

47. Xu, H.; Chu, W.; Shi, L.; Deng, S.; Zhang, H. *React. Kinet. Catal. Lett.* **2009**, *97*, 243.

48. Llorca, J.; Homs, N.; Rossell, O.; Seco, M.; Fierro, J. L. G.; de la Piscina, P. R. *J. Mol. Catal. A: Chem.* **1999**, *149*, 225.

49. Figueiredo, R. T.; Granados, M. L.; Fierro, J. L. G.; Vigas, L.; de la Piscina, P. R.; Homs, N. *Appl. Catal., A* **1998**, *170*, 145.

50. Feng, W.; Wang, Q.; Jiang, B.; Ji, P. *Ind. Eng. Chem. Res.* **2011**, *50*, 11067.

51. Subramanian, N. D.; Balaji, G.; Kumar, C. S. S. R.; Spivey, J. J. *Catal. Today* **2009**, *147*, 100.

52. Subramanian, N. D.; Kumar, C. S. S. R.; Watanabe, K.; Fischer, P.; Tanaka, R.; Spivey, J. J. *Catal. Sci. Technol.* **2012**.

53. Hindermann, J. P.; Deluzarche, A.; Kieffer, R.; Kiennemann, A. *Can. J. Chem. Eng.* **1983**, *61*, 21.

54. Mouaddib, N.; Perrichon, V.; Primet, M. *J. Chem. Soc. Faraday T. 1* **1989**, *85*, 3413.

55. Mouaddib, N.; Perrichon, V.; Martin, G. A. *Appl. Catal., A* **1994**, *118*, 63.

56. Takeuchi, K.; Matsuzaki, T.; Hanaoka, T.; Arawaka, H.; Sugi, Y. *Chem. Express* **1988**, *3*, 235.

57. Tien-Thao, N.; Hassan Zahedi-Niaki, M.; Alamdari, H.; Kaliaguine, S. *J. Catal.* **2007**, *245*, 348.

58. Xiaoding, X.; Doesburg, E. B. M.; Scholten, J. J. F. *Catal. Today* **1987**, *2*, 125.

59. de Aquino, A. D.; Cobo, A. J. G. *Catal. Today* **2001**, *65*, 209.

60. Xiaoding, X.; Mausbeck, D.; Scholten, J. J. F. *Catal. Today* **1991**, *10*, 429.

61. Xiaoding, X.; Scholten, J. J. F.; Mausbeck, D. *Appl. Catal., A* **1992**, *82*, 91.

62. Stiles, A. B.; Chen, F.; Harrison, J. B.; Hu, X. D.; Storm, D. A.; Yang, H. X. *Ind. Eng. Chem. Res.* **1991**, *30*, 811.

63. Chu, W.; Kieffer, R.; Klennemann, A. *React. Kinet. Catal. Lett.* **1992**, *48*, 627.

64. Kiennemann, A.; Boujana, S.; Diagne, C.; Chaumette, P.; Ichikawa, M.; Koerts, T.; Dejong, K. P. *Stud. Surf. Sci. Catal.* **1993**, *75*, 1479.

65. Dong, X.; Liang, X. L.; Li, H. Y.; Lin, G. D.; Zhang, P.; Zhang, H. B. *Catal. Today* **2009**, *147*, 158.

66. Zhang, H. B.; Dong, X.; Lin, G. D.; Liang, X. L.; Li, H. Y. *Chem. Commun.* **2005**, 5094.

67. Riguetto, B. A.; Rodrigues, C. E. C.; Morales, M. A.; Baggio-Saitovitch, E.; Gengembre, L.; Payen, E.; Marques, C. M. P.; Bueno, J. M. C. *Appl. Catal., A* **2007**, *318*, 70.

68. Margitfalvi, J. L.; Tompos, A.; Kolosova, I.; Valyon, J. *J. Catal.* **1998**, *174*, 246.

69. Margitfalvi, J. L.; Vankó, G.; Borbáth, I.; Tompos, A.; Vértes, A. *J. Catal.* **2000**, *190*, 474.

70. Pouilloux, Y.; Autin, F.; Guimon, C.; Barrault, J. *J. Catal.* **1998**, *176*, 215.

71. Ferretti, O. A.; Bournonville, J. P.; Mabilon, G.; Martino, G.; Candy, J. P.; Basset, J. M. *J. Mol. Catal.* **1991**, *67*, 283.

72. Vicente, A.; Lafaye, G.; Especel, C.; Marecot, P.; Williams, C. T. *J. Catal.* **2011**, *283*, 133.

73. Kiennemann, A.; Breault, R.; Hindermann, J. P.; Laurin, M. *J. Chem. Soc. Faraday T. 1* **1987**, *83*, 2119.

74. Sachtler, W. M. H.; Ichikawa, M. *J. Phys. Chem.* **1986**, *90*, 4752.

75. Ponec, V. *Catal. Today* **1992**, *12*, 227.

76. Cesar, D. V.; Perez, C. A.; Salim, V. M. M.; Schmal, M. *Appl. Catal., A* **1999**, *176*, 205.

77. Brands, D. S.; Poels, E. K.; Bliek, A. *Appl. Catal., A* **1999**, *184*, 279.

78. Marchi, A. J.; Gordo, D. A.; Trasarti, A. F.; Apesteguia, C. R. *Appl. Catal., A* **2003**, *249*, 53.

79. Reddy, B. M.; Reddy, G. K.; Rao, K. N.; Khan, A.; Ganesh, I. *J. Mol. Catal. A: Chem.* **2007**, *265*, 276.

80. Saib, A. M.; Borgna, A.; van de Loosdrecht, J.; van Berge, P. J.; Geus, J. W.; Niemantsverdriet, J. W. *J. Catal.* **2006**, *239*, 326.

81. Jacobs, G.; Ji, Y. Y.; Davis, B. H.; Cronauer, D.; Kropf, A. J.; Marshall, C. L. *Appl. Catal., A* **2007**, *333*, 177.

82. Prieto, G.; Martínez, A.; Concepción, P.; Moreno-Tost, R. *J. Catal.* **2009**, *266*, 129.

Chapter 3: Reduction Processes in Cu/SiO_2, Co/SiO_2, and $CuCo/SiO_2$ Catalysts*

3.1. Introduction

Catalysts based on copper and cobalt have been studied for hydrogenation of CO to mixtures of ethanol and higher alcohols. This reaction is thought to occur by a dual site mechanism: CO associatively adsorbed on one type of site is inserted into surface hydrocarbon species arising from CO dissociation on the other site [1,2]. Hydrogenation of the resulting intermediate yields the alcohol. The site pairs mainly responsible for alcohol synthesis are often proposed to be Cu^0 and Co^0 in close interaction or proximity [1,3,4], but have occasionally been identified as $Co^0/Co^{\delta+}$ pairs, with copper maintaining this state of reduction [5]. In fact, the nature of the active centers may depend on the activation conditions applied to the catalyst [6]. Therefore, it is important to understand reduction processes in both copper-cobalt catalysts and their monometallic counterparts.

Bulk unsupported CuO normally reduces in a single step to Cu^0, without formation of a Cu_2O intermediate [7,8]. Copper oxide becomes reducible at lower temperature when supported on silica than when unsupported, due to increased dispersion and greater reactivity toward H_2 [9-11]. Sometimes multiple peaks are observed during temperature programmed reduction (TPR) of Cu/SiO_2 catalysts. In such cases, some authors associate the lower temperature peak with reduction of a CuO phase of low crystallinity and small particle size, presumably forming Cu^0 directly. [11-14]. Others claim small CuO particles should interact with SiO_2, hindering reduction [10]. Moreover, if the area ratio of these TPR peaks is ~1:1, then the possibility of a sequential reduction, $CuO \rightarrow Cu_2O \rightarrow Cu$, must also be considered.

* Reprinted from Smith, M. L.; Campos, A.; Spivey, J. J. *Catal. Today* **2012**, *182*, 60, with permission from Elsevier.

Co/SiO_2 catalysts typically reduce in two steps: $Co_3O_4 \rightarrow CoO \rightarrow Co^0$ [15-17]. The second step, in particular, is impeded by support interactions that become important when the particle size is small [15]. Divalent cobalt species show increasing difficulty of reduction in the following order: Co^{2+} with little support interaction, Co^{2+} having slightly stronger interaction with SiO_2, cobalt hydrosilicates, and cobalt silicate [16]. Cobalt silicate, which is favored by high-pH preparation conditions, shows a TPR maximum at about 900°C [16].

TPR of unsupported, coprecipitated, air-calcined oxides of cobalt and copper shows that the presence of copper promotes the reduction of Co_3O_4 [18]. $CuCo/SiO_2$ catalysts usually show a single TPR peak at lower temperature than is typical for reduction of cobalt oxides [19-21]. Different authors have assumed a strong interaction between CuO and Co_3O_4 [18,19,21] or even formation of a $Cu_xCo_{3-x}O_4$ phase [18,20] to explain the promoting effect of copper on cobalt reduction.

Catalyst reduction pathways depend on preparation method, thermal treatment, and metal loading and can be quite complex even in monometallic systems. Addition of a second metal complicates the system even further. Therefore, a thorough characterization of the activation process is a prerequisite for understanding the nature of active species in each catalyst. The objective of this work is to apply complementary characterization techniques (TPR, *in situ* XRD, and *in situ* XANES) to study the effects of copper and cobalt upon each other during reduction of SiO_2-supported catalysts.

3.2. Materials and Methods

3.2.1. Catalyst Preparation

Three catalysts were prepared by incipient wetness impregnation of SiO_2 (PQ Corporation) with an aqueous solution of $Cu(NO_3)_2 \cdot 2.5\ H_2O$ alone, $Co(NO_3)_2 \cdot 6\ H_2O$ alone, or

both these salts together. The catalysts were dried overnight (17 h) at 100-105°C. They were calcined in a tube furnace in stagnant air by ramping at 4°C/min to 500°C and maintaining that temperature for 2 h.

The designations and nominal compositions, on a post-reduction basis, of the three catalysts are as follows: (1) Cu/SiO_2, 3.5 wt% Cu; (2) Co/SiO_2, 3.5 wt% Co; and (3) $CuCo/SiO_2$, 3.5 wt% Cu, 3.5 wt% Co.

3.2.2. Composition and Texture

The actual compositions of the calcined catalysts were determined by ICP-OES using a Perkin Elmer 2000 DV ICP-optical emission spectrometer.

Flow BET measurements were performed in an Altamira AMI-200 system. About 40 mg of calcined catalyst was pretreated in 30 sccm He at 150°C for 30 min. N_2 concentrations of 10%, 20%, and 30% in a He carrier were used for the adsorption. BET surface area was calculated based on N_2 adsorption at liquid nitrogen temperature.

3.2.3. Temperature Programmed Reduction (TPR)

TPR experiments were carried out in an Altamira AMI-200 system. The catalyst (45 mg) was dried in 30 sccm He at 120°C for 100 min. After cooling to room temperature, the catalyst was exposed to 30 sccm of 10% H_2/Ar flow as the temperature ramped at 10°C/min to 750°C. H_2 consumption was monitored by a thermal conductivity detector (TCD). Calibration of the TCD by TPR of Ag_2O enabled quantitative evaluation of H_2 consumption.

3.2.4. *In situ* X-ray Diffraction (XRD)

XRD experiments were done at the Center for Nanophase Materials Sciences, Oak Ridge National Laboratory, Oak Ridge, TN. The catalyst sample was loaded into an Anton Paar

XRK900 reaction chamber and exposed to 4% H_2/He flow. XRD patterns were recorded at selected temperatures by a PANalytical X'Pert Pro MPD diffractometer using Cu Kα radiation. The scan speed was 0.030384°/s, and the step size was 0.017°.

Phase identification was carried out by the Search & Match feature of X'Pert HighScore Plus (v. 3.0) using the library provided by the Crystallography Open Database.

3.2.5. *In situ* X-ray Absorption Near Edge Structure (XANES)

XANES measurements were collected on the Double Crystal Monochromator (DCM) beamline at the J. Bennett Johnston, Sr., Center for Advanced Microstructures and Devices (CAMD), Baton Rouge, LA. About 20 mg of sample was mixed with 20 mg of amorphous SiO_2 and loaded into a Lytle cell. As a 10% H_2/Ar mixture flowed over the catalyst, the temperature was increased at 2°C/min to 362°C.

XANES spectra were collected at the Cu K-edge of $CuCo/SiO_2$ and the Co K-edge of Co/SiO_2 and $CuCo/SiO_2$. During the temperature ramp, scans were collected using the following parameters: 1 eV steps in the range -50 to -15 eV relative to the edge, 0.5 eV steps in the range -15 to 50 eV, and 1 eV steps in the range 50-100 eV. The integration time at each data point was 1 s. A foil reference of the element being measured was placed in the beam path beyond the sample and scanned in transmission mode.

Transmission data were processed and analyzed in the Athena (v. 0.8.061) component of the Ifeffit software [22]. First, the edge energy of the foil reference (taken as the maximum in the first derivative of its spectrum) was shifted to its literature value (8979 eV for Cu, 7709 eV for Co) [23]. Each simultaneously measured sample spectrum was calibrated according to that shift. The spectra were processed by deglitching and determination of the pre-edge line and normalization range. Next, each spectrum was analyzed by linear combination fitting (LCF) of

its derivative to the derivative spectra of reference standards. The Cu standards included CuO, Cu_2O, and Cu^0 foil. The Co standards included Co_3O_4, CoO, and Co^0 foil. The model adopted for each fitting each spectrum was selected by a combinatorial approach, using all three standards and all possible combinations of two standards. Of the four possible fits, the one with the lowest χ_v^2 value was chosen. Each fit was confined to the region of the derivative spectrum that showed clear peaks.

3.3. Results

3.3.1. Composition and Texture

BET and ICP-OES results are listed in Table 3.1. The surface areas of all the catalysts, according to N_2 adsorption, are between 250 and 270 m^2/g. The surface area of calcined SiO_2 is 279 m^2/g.

Table 3.1. Catalyst surface areas, determined by flow BET, and compositions, determined by ICP-OES.

Catalyst	S_{BET} (m^2/g)	Composition (wt%)	
		Co	Cu
Cu/SiO_2	261 ± 14	--	3.30 ± 0.06
Co/SiO_2	268 ± 11	2.99 ± 0.15	--
$CuCo/SiO_2$	251 ± 4	2.97 ± 0.02	3.18 ± 0.09

3.3.2. TPR

TPR profiles of the three catalysts are shown in Figure 3.1. Cu/SiO_2 exhibits a main peak at 220°C, with a high temperature shoulder and another small feature at 300°C. The Co/SiO_2 profile contains a broad area of hydrogen consumption, spanning from 220°C to 600°C and apparently consisting of several overlapping reduction bands. Like that of Cu/SiO_2, the $CuCo/SiO_2$ TPR shows a prominent peak at 220°C, but its shoulder is on the low temperature side.

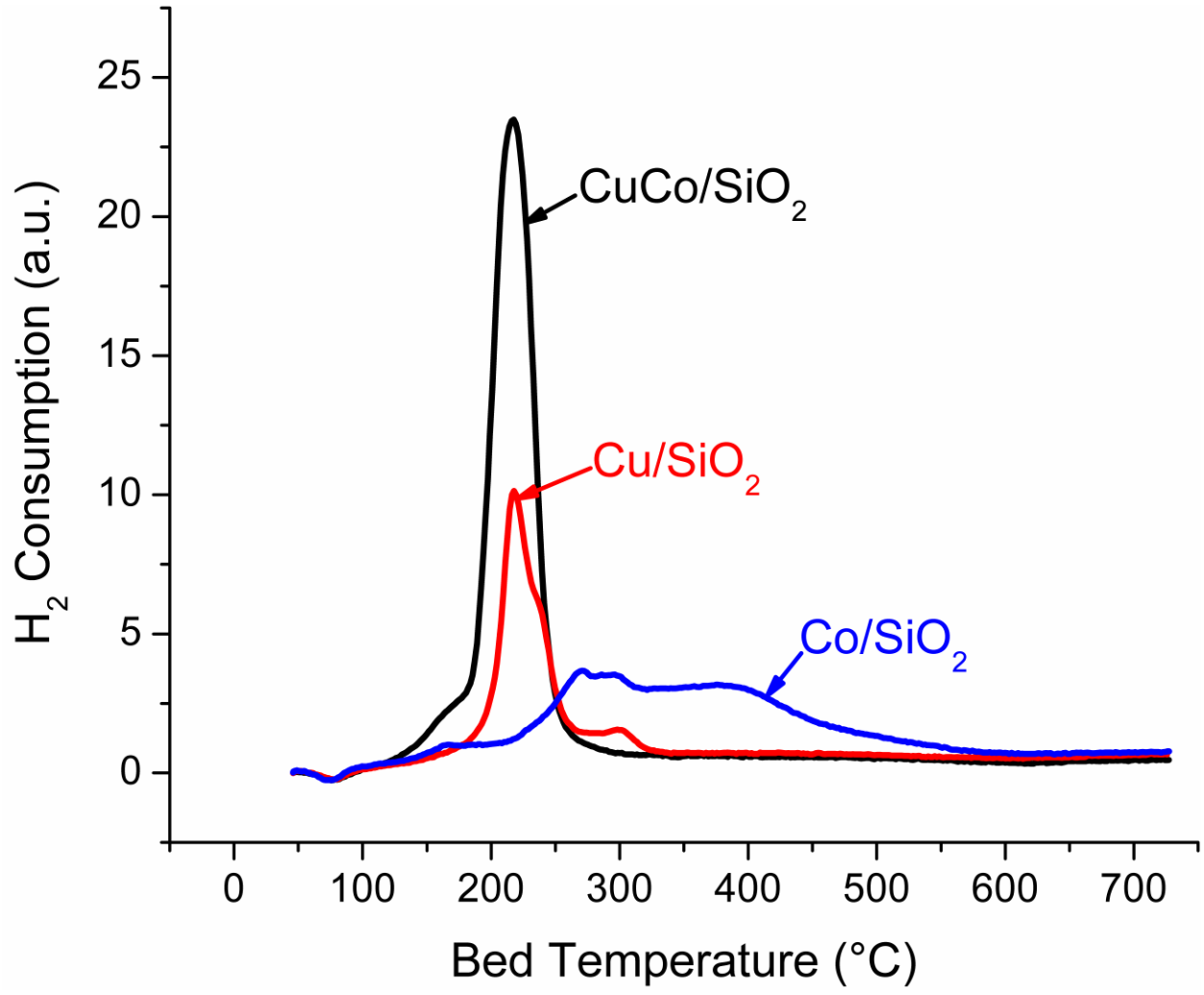

Figure 3.1. TPR profiles in 10% H_2/Ar, ramping at 10°C/min.

Quantities of hydrogen consumed by each catalyst are listed in Table 3.2. In each case, the catalyst consumes sufficient hydrogen to reduce CuO, when present, to Cu^0 and Co_3O_4, when present, to Co^0. In addition, the hydrogen consumption by $CuCo/SiO_2$ is near the sum of the total uptakes by Cu/SiO_2 and Co/SiO_2.

Table 3.2. Quantitative H_2 consumption during TPR.

Catalyst	H_2 consumption (mmol/g)	Expected H_2 consumption[a] (mmol/g)
Cu/SiO_2	0.65 ± 0.10	0.52
Co/SiO_2	0.76 ± 0.09	0.68
$CuCo/SiO_2$	1.50 ± 0.23	1.17

[a]Assuming complete conversion of CuO and Co_3O_4 to Cu^0 and Co^0, respectively.

3.3.3. *In situ* XRD

The XRD patterns of Cu/SiO_2 during isothermal hydrogen reduction at selected temperatures are shown in Figure 3.2. This catalyst initially contains CuO, as expected. With increasing temperature, the crystalline phases in Cu/SiO_2 transform as follows. At 200°C, a small amount of Cu^0 appears. At 250°C, CuO almost disappears, and Cu^0 is the dominant phase. A minor peak at $2\theta = 36.6°$ and $d = 2.45$ suggests also the presence of a small amount of Cu_2O [14,24,25]. By 300°C, Cu^0 is the only remaining phase detected by XRD.

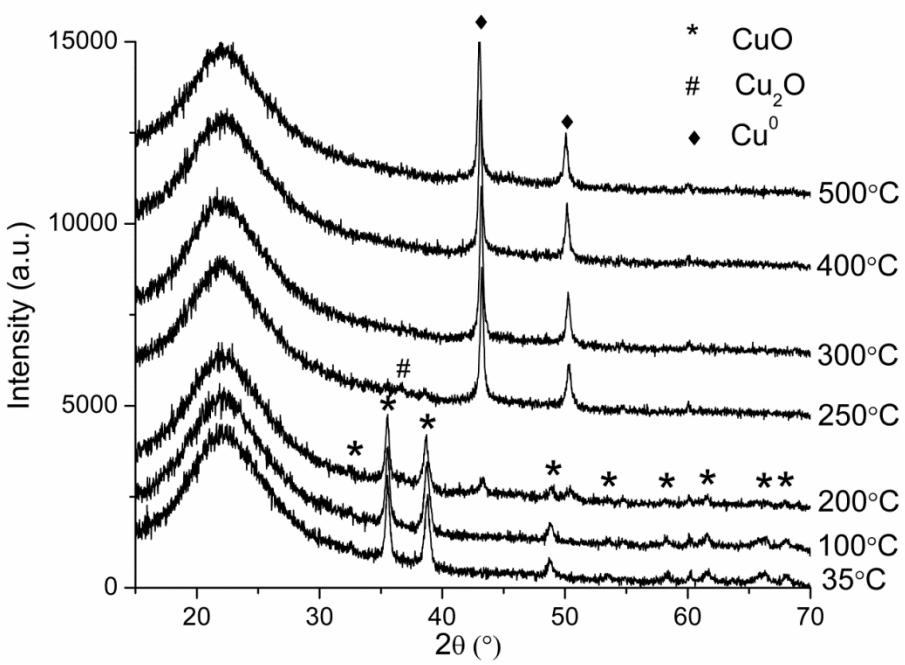

Figure 3.2. XRD patterns of Cu/SiO_2 during reduction in 4% H_2/He at the indicated temperatures.

The XRD patterns of Co/SiO_2 during reduction (Figure 3.3) show that Co_3O_4 is the starting crystalline phase, which transforms to CoO by 300°C. At 400°C, CoO has begun converting to a cubic Co^0 phase, but this process is complete only after an extended time at 600°C.

$CuCo/SiO_2$ initially contains crystalline CuO and Co_3O_4 (Figure 3.4). At 200°C, metallic phases have begun to appear. Intermediates such as Cu_2O and CoO may also be present at this stage, though interference from other peaks hinders this determination. By 300°C, only metallic crystalline phases remain.

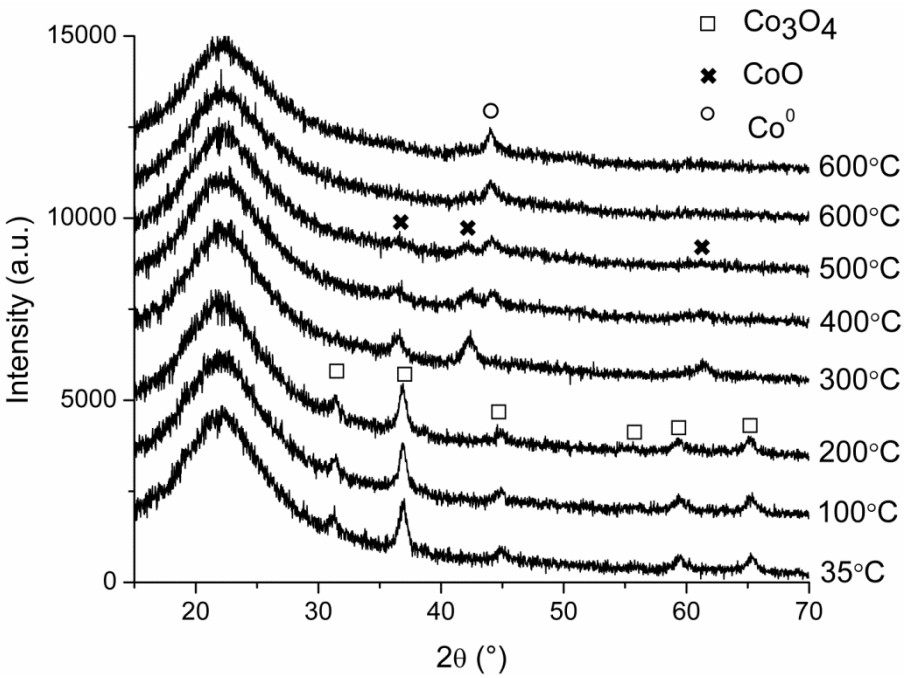

Figure 3.3. XRD patterns of Co/SiO_2 during reduction in 4% H_2/He at the indicated temperatures. A second scan was collected at 600°C immediately after the first.

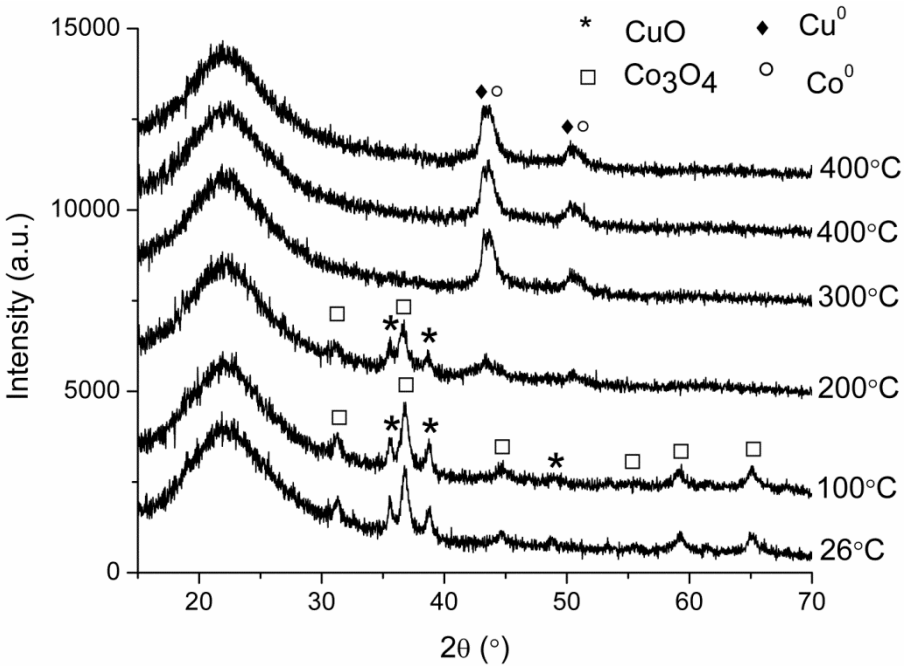

Figure 3.4. XRD patterns of $CuCo/SiO_2$ during reduction in 4% H_2/He at the indicated temperatures. A second scan was collected at 400°C immediately after the first.

The sizes of crystallites in the three catalysts were determined by the Scherrer method with correction for instrumental broadening. Table 3.3 shows the changing crystallite sizes with increasing temperature.

Table 3.3. Crystallite size (nm), determined by the Scherrer method with correction for instrumental broadening.

Temperature (°C)	Cu/SiO_2		Co/SiO_2			$CuCo/SiO_2$	
	CuO^a	Cu^{0a}	$Co_3O_4{}^a$	CoO^a	Co^{0a}	CuO^a	$Co_3O_4{}^a$
35°C (26°C) [b]	24.8	--	12.7	--	--	19.6	15.2
100°C	21.6	--	15.0	--	--	20.0	13.7
200°C	25.5	22.4	13.7	--	--	19.0	11.0
250°C	--	57.1	--	--	--	--	--
300°C	--	62.1	--	8.6	--	--	--
400°C	--	65.7	--	7.5	10.0	--	--
500°C	--	65.6	--	11.5	7.6	--	--
600°C	--	--	--	--	8.8, 10.3[c]	--	--

[a]The crystallite size calculations are based on the following peaks: CuO (111), Cu^0 (111), Co_3O_4 (311), CoO (200), and Co^0 (111).
[b]Room temperature measurements were collected at 35°C on Cu/SiO_2 and Co/SiO_2 and at 26°C on $CuCo/SiO_2$.
[c]From back-to-back measurements at 600°C.

CuO crystallites are slightly larger in Cu/SiO_2 (21-26 nm) than in $CuCo/SiO_2$ (19-20 nm). In addition, at room temperature, the area of the CuO (111) peak (not shown) is 50% less in

$CuCo/SiO_2$ than in Cu/SiO_2. The copper metal loading (from ICP) is only about 4% lower in $CuCo/SiO_2$ than in Cu/SiO_2. Thus, the bimetallic catalyst contains both crystalline and noncrystalline CuO.

When Cu^0 appears in Cu/SiO_2, crystallites initially have an average diameter of 22.4 nm (200°C), but enlarge to 57.1 nm at 250°C and 62-66 nm at higher temperatures. These sizes, from Table 3.3, were calculated based on the Cu^0 (111) peak. If instead the Scherrer formula is applied to the Cu^0 (200) peak, the Cu^0 crystallite diameter is 11.6 nm at 200°C, 32.6 nm at 250°C, and 44-47 nm at 300-500°C. If the (111) plane is assumed parallel to the support, the different dimensions obtained from different peaks suggest a flattened particle shape [26].

Co_3O_4 crystallite sizes fall into the same range (11-16 nm) in Co/SiO_2 and $CuCo/SiO_2$. However, at room temperature, the area of the Co_3O_4 (311) peak is 30% higher in $CuCo/SiO_2$ than in Co/SiO_2, whereas the cobalt metal loading is about the same in both catalysts. This suggests that more crystalline, and less amorphous, Co_3O_4 exists in $CuCo/SiO_2$ than in Co/SiO_2 at room temperature.

In Co/SiO_2, the intermediate CoO phase has a crystallite size of 7-12 nm. When Co^0 crystallites appear at 400-600°C, they are similar in size. The final Co^0 crystallite size is close to 75% of the starting Co_3O_4 crystallite size, which would be expected on the basis of the molar volumes of Co^0 and Co_3O_4 [17,27]. Co^0 crystallites on Co/SiO_2 do not exhibit the marked sintering that Cu^0 crystallites do on Cu/SiO_2.

The overlapping of the diffraction peaks of Cu^0 and Co^0 in $CuCo/SiO_2$ prevents accurate determination of their crystallite size. Overlapping or intermediate peaks can arise from intermediate lattice spacing between the spacings of pure Cu^0 and Co^0, due to alloying of the metals [28,29]. To address the question of possible alloying in $CuCo/SiO_2$, the diffraction patterns

of Cu/SiO_2, Co/SiO_2, and $CuCo/SiO_2$ at 400°C are compared in Figure 3.5. The formation of CuCo alloy cannot be ruled out from this figure, although in general Cu^0 has limited solubility in $Co^{0\ 6}$ and would be expected to segregate to the surface of such an alloy to lower the surface free energy [27].

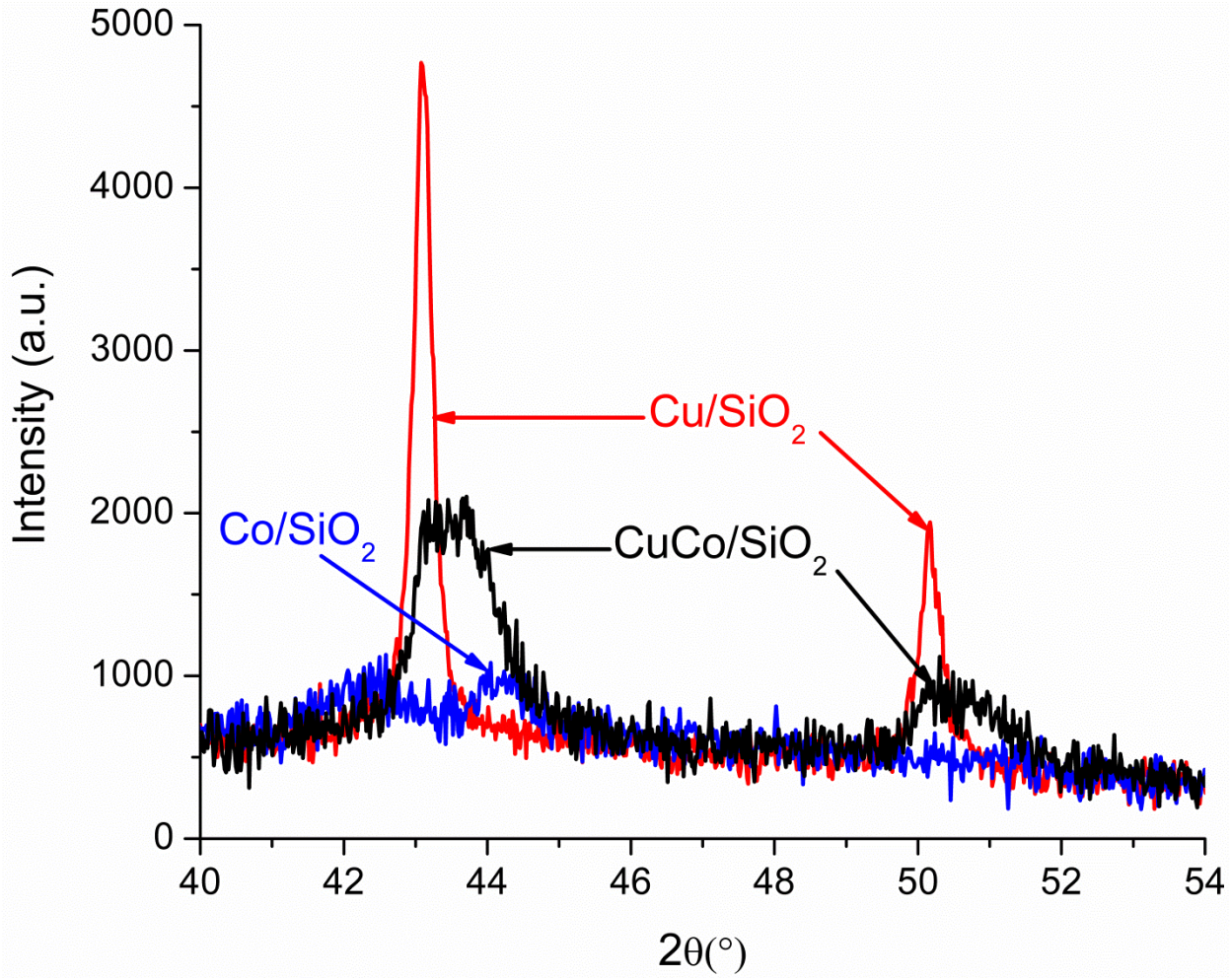

Figure 3.5. XRD patterns of Cu/SiO_2, Co/SiO_2, and $CuCo/SiO_2$ during reduction in 4% H_2/He at 400°C.

3.3.4. *In situ* XANES

The XANES spectra and LCF results at the Co K-edge of Co/SiO_2, the Co K-edge of $CuCo/SiO_2$, and the Cu K-edge of $CuCo/SiO_2$ during temperature programmed reduction are shown in Figures 3.6-3.8, respectively. The XANES spectra of cobalt and copper reference compounds are shown in Figure 3.9. Sample LCFs from each *in situ* experiment are shown in Figure 3.10.

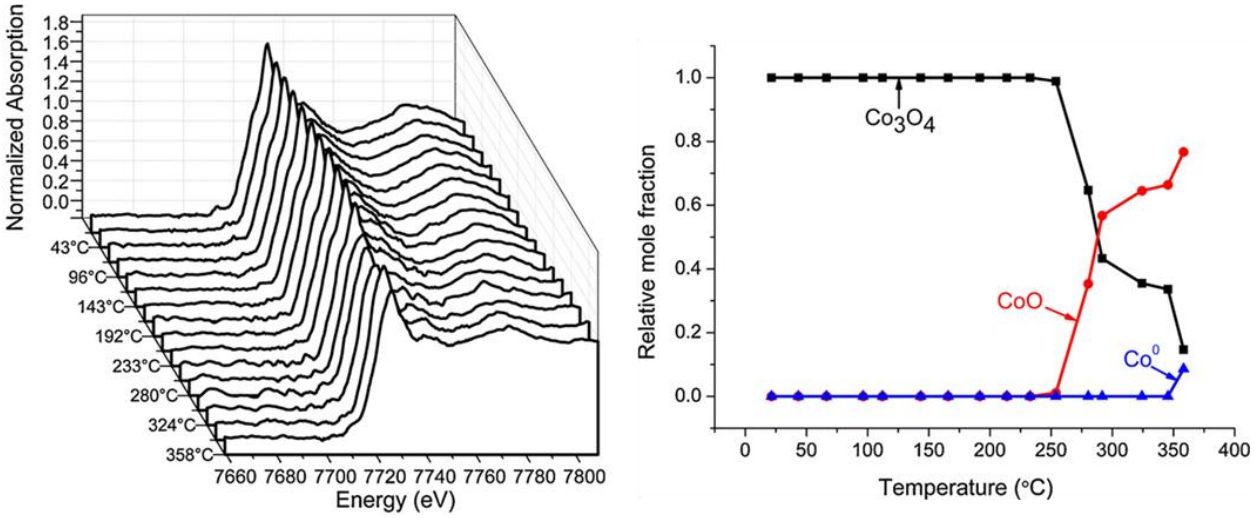

Figure 3.6. Left: XANES spectra at the Co K-edge of Co/SiO_2 during temperature ramping at 2°C/min in 10% H_2/Ar. Right: Composition of cobalt phases in Co/SiO_2, from LCF, as a function of temperature. Non-cobalt phases are excluded from the mole fractions.

Initially, Co_3O_4 is the only cobalt phase present in Co/SiO_2 (Figure 3.6). At about 280°C, the white line region of the spectrum begins to assume the more rounded shape of the CoO standard, which is confirmed by the appearance of CoO in the LCF profile. However, as Co_3O_4 reduces, the fit becomes imperfect in the white line region as shown in Figure 3.10. Probably, Co_3O_4 reduces via CoO species that have varying degrees of interaction with the support.

Electron deficiencies due to such interactions can result in enhanced white line intensities that cannot be perfectly modeled by reference spectra of bulk compounds [30]. Consequently, the full extent of Co_3O_4 conversion may not be completely captured by the LCF results in Figure 3.6. Nevertheless, the spectra clearly show that appreciable Co_3O_4 reduction occurs by 280°C. Furthermore, a small shoulder begins to develop at the absorption edge at 358°C, denoting the first appearance of Co^0.

Figure 3.7 shows the Co K-edge spectra and LCF results on $CuCo/SiO_2$. The low-temperature scans confirm that Co_3O_4 is the starting cobalt phase in this catalyst. Conversion to CoO begins at about 215°C, 65°C lower than for the monometallic Co/SiO_2 catalyst. This is also accompanied by a decrease in the white line intensity and growth of a shoulder at the edge, corresponding to the simultaneous appearance of Co^0 at the same temperature.

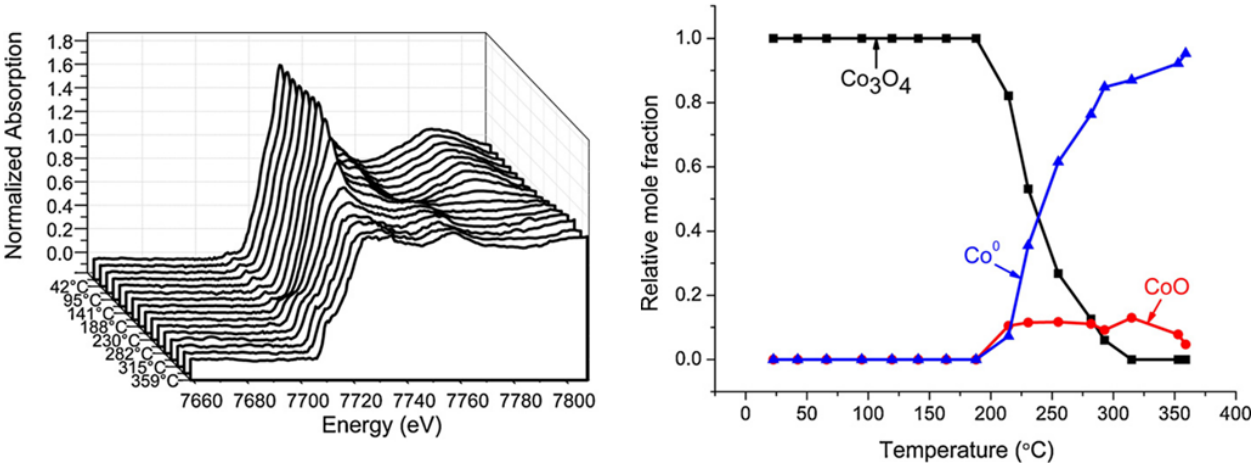

Figure 3.7. Left: XANES spectra at the Co K-edge of $CuCo/SiO_2$ during temperature ramping at 2°C/min in 10% H_2/Ar. Right: Composition of cobalt phases in $CuCo/SiO_2$, from LCF, as a function of temperature. Non-cobalt phases are excluded from the mole fractions.

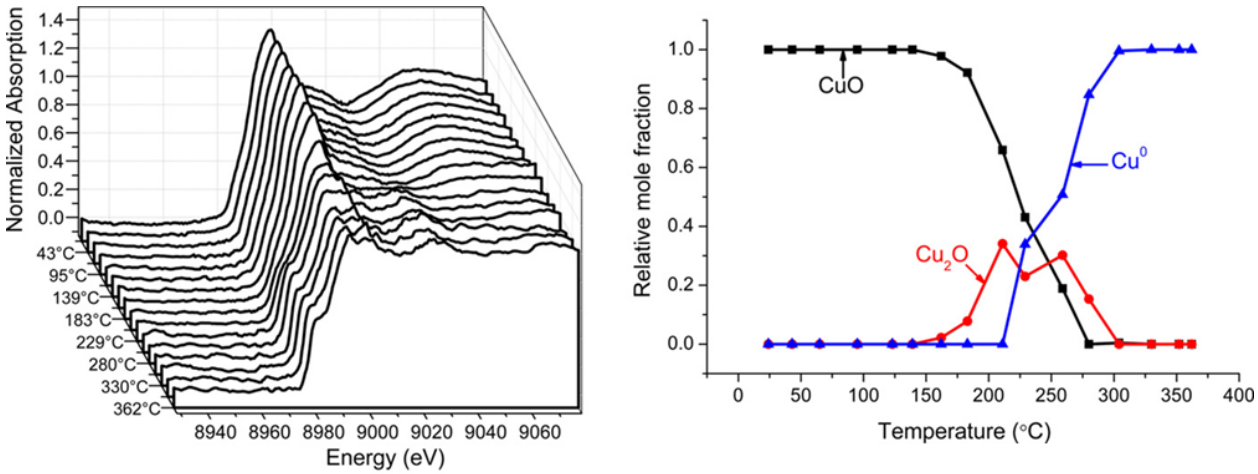

Figure 3.8. Left: XANES spectra at the Cu K-edge of $CuCo/SiO_2$ during temperature ramping at 2°C/min in 10% H_2/Ar. Right: Composition of copper phases in $CuCo/SiO_2$, from LCF, as a function of temperature. Non-copper phases are excluded from the mole fractions.

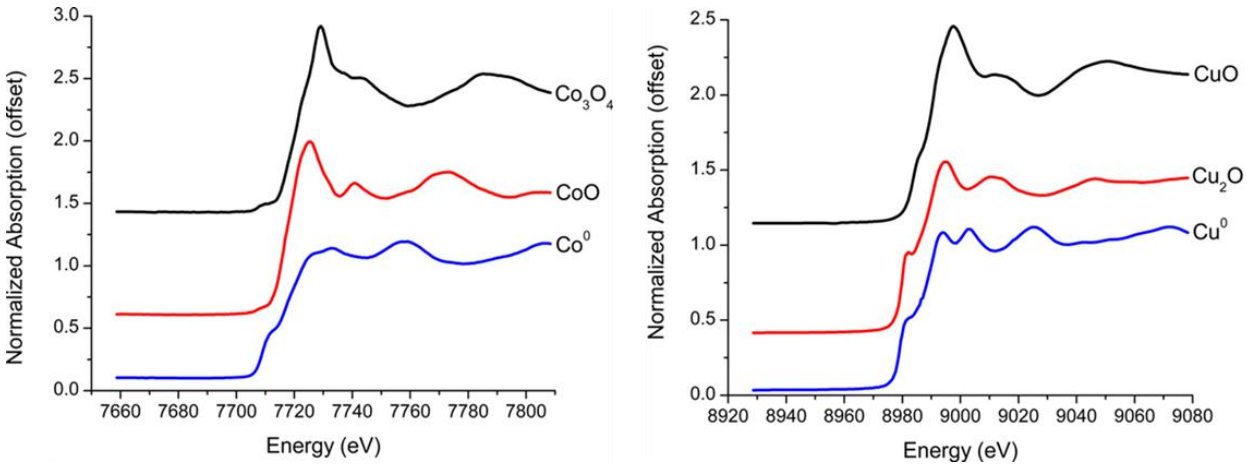

Figure 3.9. Left: Co K-edge XANES spectra of reference standards (Co_3O_4, CoO, and Co^0) used in LCF of cobalt phases. Right: Cu K-edge XANES spectra of reference standards (CuO, Cu_2O, and Cu^0) used in LCF of copper phases.

Figure 3.8 shows the Cu K-edge spectra and LCF results on $CuCo/SiO_2$. When compared to the Cu reference standards in Figure 3.9, the spectra up to 140°C match that of CuO. In the

early stages of reduction, CuO is converted first to Cu_2O. At about 230°C, Cu^0 appears as well. By 300°C, conversion to Cu^0 is complete.

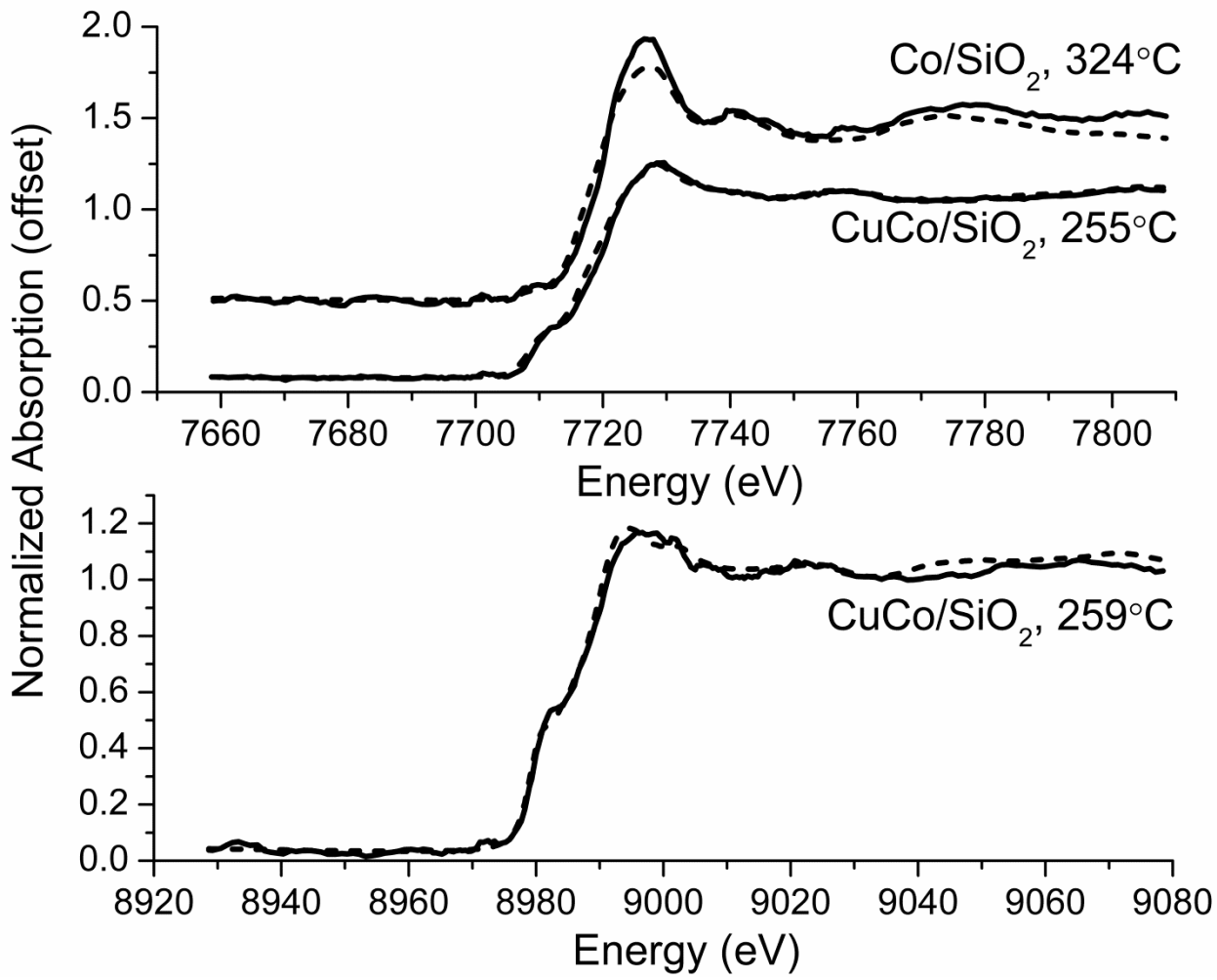

Figure 3.10. Sample LCFs of Co K-edge spectra (top), including Co/SiO_2 at 324°C and $CuCo/SiO_2$ at 255°C, and a Cu K-edge spectrum (bottom) of $CuCo/SiO_2$ at 259°C.

3.4. Discussion

After isothermal reduction at 400°C, Cu/SiO_2 would be expected to contain Cu^0, Co/SiO_2 to contain Co^0 and CoO, and $CuCo/SiO_2$ to contain a mixture of Cu^0 and Co^0. Thus, the

reduction temperature can be manipulated in order to produce catalysts containing the desired species, whether Co^0/Cu^0 or Co^0/Co^{2+}.

3.4.1. Effect of Co Addition to Cu/SiO_2

The low temperature shoulder in the TPR (Figure 3.1) of $CuCo/SiO_2$ can be identified with the help of XRD and XANES results. From peak fitting of the TPR profile, the shoulder arises from a band at about 170°C that accounts for 12.5% of the total hydrogen consumption by this catalyst. In the room temperature XRD patterns, comparison of the areas of the CuO (111) peak of Cu/SiO_2 and of $CuCo/SiO_2$ shows that this phase is more crystalline in Cu/SiO_2. Assuming that CuO in Cu/SiO_2 is fully crystalline, an estimated 50% of the CuO in $CuCo/SiO_2$ is noncrystalline. Thus, the main TPR peak at 220°C (observed for both catalysts) involves reduction of crystalline CuO, and the shoulder at 170°C (visible only in $CuCo/SiO_2$) corresponds to reduction of noncrystalline CuO. From XANES (Figure 3.8), it is clear that CuO in $CuCo/SiO_2$ begins reducing to Cu_2O before 200°C, before the appearance of metallic Cu, and before any reduction of Co_3O_4. Accordingly, the earlier conclusion can be extended to say the shoulder at 170°C relates to reduction of noncrystalline CuO to Cu_2O. This point can be further corroborated by calculating the percentage of total H_2 consumption needed to reduce noncrystalline CuO (that is, 50% of total CuO in $CuCo/SiO_2$) to Cu_2O. This value comes to 10.7%, compared to 12.5% obtained by peak fitting. The slight discrepancy between the two values might have been introduced during profile fitting of the TPR and XRD patterns.

An alternative explanation for the decrease in crystalline CuO and increase in crystalline Co_3O_4 observed by XRD in $CuCo/SiO_2$ relative to the monometallic catalysts could be formation of a mixed oxide. A spinel-type oxide, with incorporated Cu, would be difficult to

distinguish from Co_3O_4 by XRD [31,32]. However, the $Cu_xCo_{3-x}O_4$ phase shows low thermal stability, especially at Cu/Co ratios as high as the one used in this work, and would be expected to decompose during the calcination at 500°C [31]. Furthermore, XANES analysis does not support the formation of a copper-cobalt mixed metal oxide in the catalyst as-prepared or during reduction. For example, the XANES lineshapes from Cu^{2+} in CuO and in the octahedral sites of a spinel would be expected to differ markedly, by analogy to results obtained on CuO and $CuFe_2O_4$ (Figure 3 of [33]). These reasons support the idea that the decrease in CuO diffraction peaks is due to creation of an amorphous fraction of CuO, not incorporation of Cu into the spinel phase.

The Cu/SiO_2 TPR profile (Figure 3.1) has shoulders on the high, rather than low, temperature side. Peak fitting reveals that the main peak at 220°C, already assigned to reduction of crystalline CuO, has an area approximately equal to the sum of the areas of the high temperature shoulder (240°C) and small peak at 300°C. From the stoichiometry of H_2 consumption for a stepwise reduction, this suggests that the main peak corresponds to reduction of CuO to Cu_2O, and the secondary peaks represent reduction of Cu_2O to Cu^0. From XRD (Figure 3.2), residual crystalline Cu_2O is observed at 250°C and converts to Cu metal during isothermal treatment at 300°C. This confirms that Cu_2O is an intermediate during reduction of Cu/SiO_2.

The separation of Cu_2O reduction into two TPR peaks suggests that a fraction of the intermediate Cu_2O (about 26% of it) is especially difficult to reduce to Cu metal. It is not obvious why this should be so, but the type of Cu_2O that reduces with relative difficulty at 300°C is not observed in $CuCo/SiO_2$.

3.4.2. Effect of Cu Addition to Co/SiO_2

The reduction of Co/SiO_2 occurs over a wide temperature range, which implies the existence of many reducible species in varying degrees of interaction with the support [16]. The amplified white line of the Co K-edge spectra of reducing Co/SiO_2 suggests that the Co^{2+} species, in particular, are more electron deficient than in bulk CoO. In fact, the XANES spectra of CoO and Co_2SiO_4 are quite similar [17], the main difference being a more intense white line in the spectrum of the latter. Nevertheless, the formation of Co_2SiO_4, which reduces at temperatures greater than 800°C [16,17], does not seem to occur on Co/SiO_2, which is completely reduced at 600°C. According to the XRD results (Figure 3.3), CoO itself is difficult to reduce on Co/SiO_2 and is observed across a wide temperature span, 300-500°C. The strength of interaction of Co^{2+} with SiO_2 seems to lie somewhere between bulk unsupported CoO and Co_2SiO_4.

Co_3O_4 in $CuCo/SiO_2$ reduces simultaneously with crystalline CuO, at a temperature about 65°C lower than the corresponding transformation in Co/SiO_2. The reduction of Co^{2+} is very efficiently promoted by copper. According to TPR and XRD, this process is complete by 300°C on $CuCo/SiO_2$, whereas it continues up to 600°C on Co/SiO_2. XANES also shows that the CoO intermediate is reduced almost as fast as it can be produced on $CuCo/SiO_2$, in marked contrast to the situation on Co/SiO_2. This indicates that an interaction between copper and cobalt phases exists, and it has a stronger effect on Co^{2+} reducibility than the cobalt-silica interaction, which would tend to maintain cobalt in an oxidized state.

3.5. Conclusions

CuO and Co_3O_4 reduce via two step processes—CuO → Cu_2O → Cu^0 and Co_3O_4 → CoO → Co^0, respectively, on SiO_2-supported monometallic and bimetallic catalysts. The effects of cobalt addition to a Cu/SiO_2 catalyst are (1) an increase in the dispersion and amorphous content of CuO, (2) creation of a more easily reducible (to Cu_2O) fraction of CuO, due to its higher dispersion, and (3) elimination of a type of Cu_2O that is relatively difficult to reduce. The main effect of copper addition to a Co/SiO_2 catalyst is to increase the reducibility of cobalt oxides, especially of CoO.

3.6. References

1. Bailliard-Letournel, R. M.; Cobo, A. J. G.; Mirodatos, C.; Primet, M.; Dalmon, J. A. *Catal. Lett.* **1989**, *2*, 149.

2. Kiennemann, A.; Diagne, C.; Hindermann, J. P.; Chaumette, P.; Courty, P. *Appl. Catal.* **1989**, *53*, 197.

3. Mouaddib, N.; Perrichon, V.; Martin, G. A. *Appl. Catal., A* **1994**, *118*, 63.

4. Chaumette, P.; Courty, P.; Kiennemann, A.; Kieffer, R.; Boujana, S.; Martin, G. A.; Dalmon, J. A.; Meriaudeau, P.; Mirodatos, C.; Holhein, B.; Mausbeck, D.; Hubert, A. J.; Germain, A.; Noels, A. *Ind. Eng. Chem. Res.* **1994**, *33*, 1460.

5. Baker, J. E.; Burch, R.; Hibble, S. J.; Loader, P. K. *Appl. Catal.* **1990**, *65*, 281.

6. Dalmon, J. A.; Chaumette, P.; Mirodatos, C. *Catal. Today* **1992**, *15*, 101.

7. Rodriguez, J. A.; Kim, J. Y.; Hanson, J. C.; Perez, M.; Frenkel, A. I. *Catal. Lett.* **2003**, *85*, 247.

8. Kim, J. Y.; Rodriguez, J. A.; Hanson, J. C.; Frenkel, A. I.; Lee, P. L. *J. Am. Chem. Soc.* **2003**, *125*, 10684.

9. Robertson, S. D.; McNicol, B. D.; Debaas, J. H.; Kloet, S. C.; Jenkins, J. W. *J. Catal.* **1975**, *37*, 424.

10. Bond, G. C.; Namijo, S. N.; Wakeman, J. S. *J. Mol. Catal.* **1991**, *64*, 305.

11. van der Grift, C. J. G.; Mulder, A.; Geus, J. W. *Appl. Catal.* **1990**, *60*, 181.

12. Marchi, A. J.; Fierro, J. L. G.; Santamaria, J.; Monzon, A. *Appl. Catal., A* **1996**, *142*, 375.

13. Wang, Z. L.; Liu, Q. S.; Yu, J. F.; Wu, T. H.; Wang, G. J. *Appl. Catal., A* **2003**, *239*, 87.

14. Matsumura, Y.; Ishibe, H. *J. Catal.* **2009**, *268*, 282.

15. Khodakov, A. Y.; Lynch, J.; Bazin, D.; Rebours, B.; Zanier, N.; Moisson, B.; Chaumette, P. *J. Catal.* **1997**, *168*, 16.

16. van Steen, E.; Sewell, G. S.; Makhothe, R. A.; Micklethwaite, C.; Manstein, H.; deLange, M.; Oconnor, C. T. *J. Catal.* **1996**, *162*, 220.

17. Saib, A. M.; Borgna, A.; van de Loosdrecht, J.; van Berge, P. J.; Geus, J. W.; Niemantsverdriet, J. W. *J. Catal.* **2006**, *239*, 326.

18. Fierro, G.; Lo Jacono, M.; Inversi, M.; Dragone, R.; Porta, P. *Top. Catal.* **2000**, *10*, 39.

19. Brands, D. S.; Poels, E. K.; Bliek, A. *Appl. Catal., A* **1999**, *184*, 279.

20. Cesar, D. V.; Perez, C. A.; Salim, V. M. M.; Schmal, M. *Appl. Catal., A* **1999**, *176*, 205.

21. Deng, S. Y.; Chu, W.; Xu, H. Y.; Shi, L. M.; Huang, L. H. *J. Nat. Gas Chem.* **2008**, *17*, 369.

22. Ravel, B.; Newville, M. *J. Synchrotron Radiat.* **2005**, *12*, 537.

23. Williams, G. P. In *X-Ray Data Booklet*; second ed.; Thompson, A. C., Vaughan, D., Eds.; Lawrence Berkeley National Laboratory: Berkeley, 2001, p 1.

24. Subramanian, N. D.; Balaji, G.; Kumar, C. S. S. R.; Spivey, J. J. *Catal. Today* **2009**, *147*, 100.

25. Tien-Thao, N.; Alamdari, H.; Zahedi-Niaki, M. H.; Kaliaguine, S. *Appl. Catal., A* **2006**, *311*, 204.

26. Batyrev, E. B.; van den Heuvel, J. C.; Beckers, J.; Jansen, W. P. A.; Castricum, H. L. *J. Catal.* **2005**, *229*, 136.

27. Jacobs, G.; Ribeiro, M. C.; Ma, W. P.; Ji, Y. Y.; Khalid, S.; Sumodjo, P. T. A.; Davis, B. H. *Appl. Catal., A* **2009**, *361*, 137.

28. Nguyen, T. T.; Zahedi-Niaki, M. H.; Alamdari, H.; Kaliaguine, S. *Int. J. Chem. React. Eng.* **2007**, *5*.

29. Volkova, G. G.; Yurieva, T. M.; Plyasova, L. M.; Naumova, M. I.; Zaikovskii, V. I. *J. Mol. Catal. A: Chem.* **2000**, *158*, 389.

30. Jacobs, G.; Ji, Y. Y.; Davis, B. H.; Cronauer, D.; Kropf, A. J.; Marshall, C. L. *Appl. Catal., A* **2007**, *333*, 177.

31. Li, G. H.; Dai, L. Z.; Lu, D. S.; Peng, S. Y. *J. Solid State Chem.* **1990**, *89*, 167.

32. Di Cosimo, J. I.; Marchi, A. J.; Apesteguia, C. R. *J. Catal.* **1992**, *134*, 594.

33. Krishnan, V.; Selvan, R. K.; Augustin, C. O.; Gedanken, A.; Bertagnolli, H. *J. Phys. Chem. C* **2007**, *111*, 16724.

Chapter 4: CO Adsorption Behavior of Cu/SiO_2, Co/SiO_2, and $CuCo/SiO_2$ Catalysts Studied by *in situ* DRIFTS[†]

4.1. Introduction

The reaction of syngas to produce ethanol and higher alcohols is a possible route for converting a variety of feedstocks to useful transportation fuels and fuel additives. An active, selective catalyst is necessary. Since their inception in the early 1980s [1], catalysts based on copper and cobalt have received continuing attention for this reaction [2-10]. These modified Fischer-Tropsch catalysts are attractive because they mimic the mechanism of the highly ethanol-selective Rh-based catalysts [11] but have a lower cost.

The mechanism of higher alcohol synthesis on copper-cobalt catalysts requires one site capable of CO dissociation and chain growth, together with a site that adsorbs CO molecularly [12,13]. C—C bond formation between a surface hydrocarbon group and adsorbed CO forms the surface intermediate leading to higher alcohols. However, direct hydrogenation of the adsorbed C_xH_y or CO species, without coupling of the two, yields hydrocarbons or methanol, respectively.

Most literature dealing with the active sites of copper-cobalt catalysts assigns cobalt as the site for CO dissociation and copper as the main site for molecular adsorption and CO insertion [14-17]. A few studies [18,19] have also proposed that Co^0/Co^{n+} are appropriate site pairs.

Fourier transform infrared (FTIR) spectroscopy is particularly well suited to study the interaction of CO with a catalyst surface. This technique has been applied to CO adsorption on copper-cobalt catalysts [17,20-23]. These past studies usually aimed at identifying the types of surface sites on the catalyst. For example, a shift in the frequencies of CO adsorbed on copper

[†] Reprinted (adapted) with permission from (Smith, M. L.; Kumar, N.; Spivey, J. J. *J. Phys. Chem. C* **2012**, *116*, 7931). Copyright (2012) American Chemical Society.

and cobalt in opposite directions upon combining these elements has been taken as evidence for a CuCo surface alloy [17].

The usual approach in such experiments is to collect spectra of the irreversibly adsorbed species after carefully controlled CO dosing at ambient or subambient temperature, followed by evacuation or flushing with subsequent heating [17,20-23]. The advantages of this procedure are (1) reduction of the spectral contribution of the gas phase CO signal and (2) minimization of coverage effects on the vibrational frequency of adsorbed CO. However, these conditions are necessarily far removed from the working environment of the catalyst.

The application of FTIR spectroscopy to study the direct exposure of a catalyst to syngas is rarely reported [24-26], still less so for copper-cobalt systems [23]. Considering the important role of the CO adsorption mode in directing the selectivity of the reaction, it would be instructive to follow by FTIR the effects of adsorption and changing reaction conditions on the CO bond, instead of using the technique *exclusively* as a site probe.

The objectives of this work are to study the effect of combining copper and cobalt on CO adsorption under syngas flow at different temperatures and to relate this information to the activity/selectivity of the catalysts.

4.2. Experimental Methods

4.2.1. Catalyst Preparation

The catalysts (Cu/SiO_2, Co/SiO_2, and $CuCo/SiO_2$) were prepared by the incipient wetness technique. Nitrate precursors in aqueous solution were used. The catalysts were dried overnight at 100-105 °C and calcined in a tube furnace at 500 °C (after ramping at 4 °C/min from room temperature) for 2 h.

The compositions, from ICP-OES, of the three catalysts are: (1) Cu/SiO_2, 3.30 wt% Cu; (2) Co/SiO_2, 2.99 wt% Co; and (3) $CuCo/SiO_2$, 3.18 wt% Cu, 2.97 wt% Co.

4.2.2. DRIFTS

Diffuse reflectance infrared Fourier transform spectroscopy (DRIFTS) experiments were performed in a Thermo Scientific Nicolet 6700 spectrometer with a Harrick Praying Mantis reaction chamber. A mercury cadmium telluride (MCT-A) detector was used. All steps were carried out at atmospheric pressure. Approximately 25-28 mg of sample was used in each experiment.

4.2.2.1. Pretreatment

The catalyst sample was reduced in the reaction chamber using 40 sccm 10% H_2/He at 400 °C for 1 h. The catalyst was flushed with 40 sccm He at the reduction temperature for an additional 1 h. Background spectra were collected at 400 °C, 300 °C, 200 °C, 100 °C, and room temperature during cooling in He.

4.2.2.2. CO Adsorption and Desorption

At room temperature, 10 sccm of 5% CO/He were added to the 40 sccm of He already flowing. Spectra were collected (64 scans, with 4 cm^{-1} resolution) using the room temperature background. CO adsorption continued for about 9 min, with spectra being collected about once per minute. Next, the 5% CO/He flow was removed. Spectra were collected as He continued to flush the reaction chamber. After about 9 min, the temperature was increased to 100 °C and a spectrum collected using the corresponding background. Spectra were also collected at 200 °C, 300 °C, and 400 °C.

4.2.2.3. CO Hydrogenation

Following reduction and background collection, 10 sccm of 5% CO/He + 10 sccm of 10% H_2/He were added to the 40 sccm of He already flowing. Spectra were collected (64 scans, with 4 cm^{-1} resolution) using the room temperature background. Spectra were also collected at 100 °C, 200 °C, 300 °C, 400 °C, and again at 300 °C using the appropriate background in each case. Each temperature was maintained until no further changes were observed in the spectra before changing to the next condition. Products were monitored concurrently in a Hiden Analytical quadrupole mass spectrometer.

4.2.3. Catalytic Reaction

Reactions were carried out on 150 mg of sample in a ¼" glass lined stainless steel reactor tube in an Altamira 200R-HP unit. The catalyst was reduced in H_2/He at 400 °C for 1 h then cooled to room temperature in He. The system was pressurized to 10 bar and subsequently heated to 200 °C in He. At this point, the reactant mixture (space velocity = 24,000 scc/g_{cat}/h, H_2/CO = 2/1) replaced He. Products were analyzed by an online gas chromatograph with flame ionization and thermal conductivity detectors (FID and TCD). The temperature was changed to 250 °C and chromatograms recorded in the same way. Data were also collected at 275 °C, 300 °C, and again at 250 °C (275 °C for Cu/SiO_2) to check for deactivation during the run.

The reactor outlet lines were heated up to the Shimadzu GC-2014 gas chromatograph in order to prevent product condensation. CO_2 and CO were analyzed by TCD using a He carrier. Hydrocarbons and alcohols were analyzed by FID after being separated in a Restek Rt-Q-BOND column (25 m × 0.53 mm × 20 μm).

4.3. Results and Discussion

4.3.1. CO Adsorption and Desorption

4.3.1.1. Copper Sites of Cu/SiO_2 and $CuCo/SiO_2$

Selected spectra taken during CO adsorption and desorption are shown in Figure 4.1. In CO/He flow, both catalysts show an absorption at 2127 cm^{-1} on top of the doublet for gas-phase CO. During He flushing at room temperature, gas-phase CO is removed, while the peak due to adsorbed CO is retained. At 100 °C in He flow, the peak decreases in size. At 200 °C, it almost disappears, and at 300 °C, it is totally absent.

The frequency of infrared absorption on Cu/SiO_2 and $CuCo/SiO_2$ at 2127 cm^{-1} is the same within the resolution, shifting no more than 5 cm^{-1} during the experiments. A similar band near 2130 cm^{-1} has been previously observed in FTIR studies of copper-based catalysts and is often attributed to CO adsorbed on Cu^+ (Cu_2O) sites [27,28], particularly when it is stable to evacuation, flushing, or heating [29-32]. When easily removable by outgassing, it has also been assigned to CO adsorbed on small, two-dimensional, partially electropositive copper particles [33]. Maxima above 2120 cm^{-1} have alternatively been assigned to Cu crystallites with protruding Cu atoms, or atomically rough surfaces [34]. Greeley et al. [35], in a density functional theory (DFT) study of methanol synthesis catalysts, reported that a CO vibrational frequency of about 2130 cm^{-1} is consistent with three possible CO adsorption sites: Cu adatoms, compressed Cu surfaces, and Cu surfaces containing subsurface oxygen. Furthermore, the Cu surface containing subsurface oxygen showed the same CO stretching frequency even when the oxygen was removed and the surface atoms frozen in place. Greeley et al. therefore suggested that the band is situated at 2130 cm^{-1} due to CO adsorbed on a copper atom elevated above the surface, rather than an electronic effect. In their own DFT study of CO adsorption on Cu/SiO_2, Ferullo and Castellani [36] saw

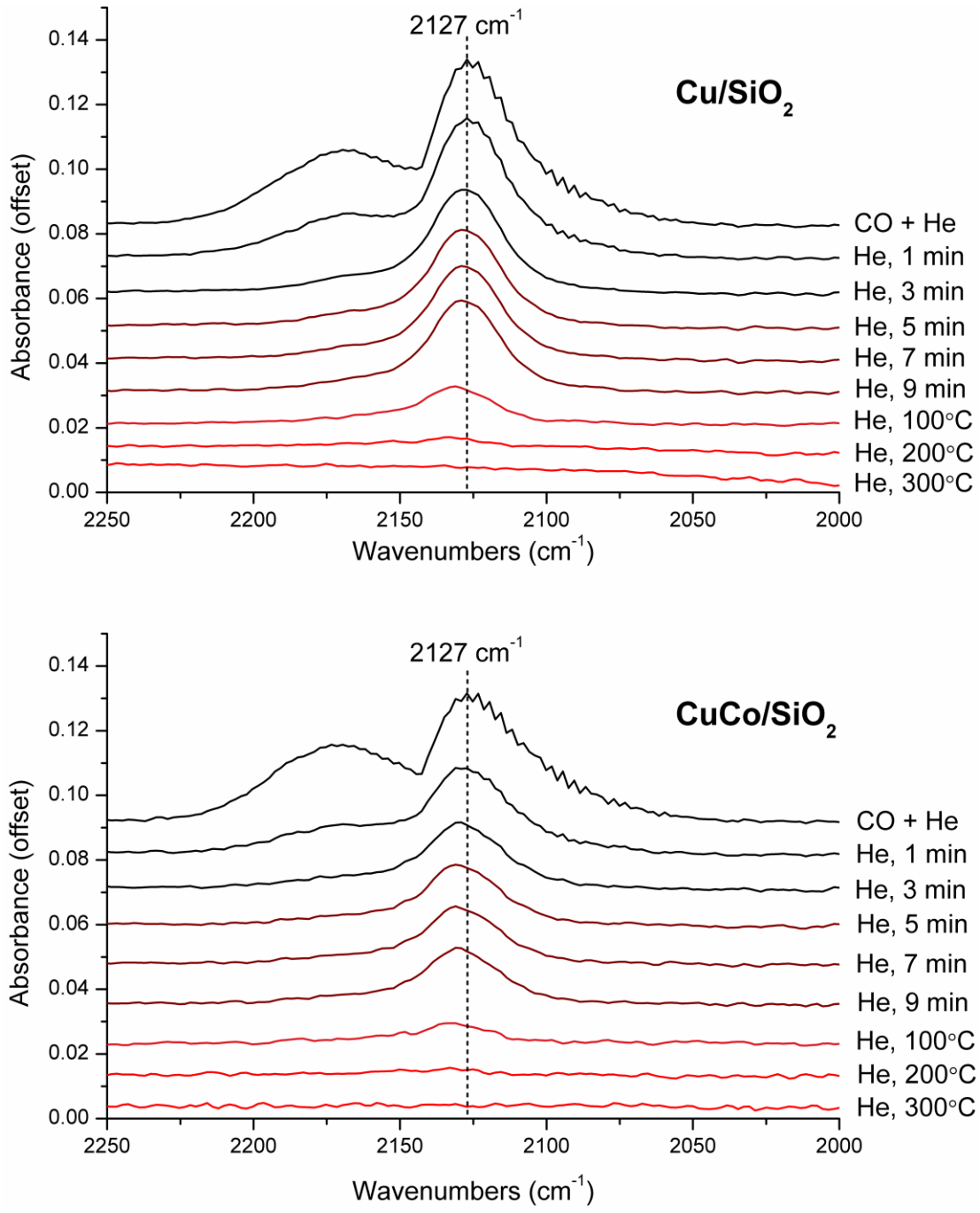

Figure 4.1. DRIFTS spectra during CO adsorption/desorption at 1 atm on Cu/SiO_2 (top) and $CuCo/SiO_2$ (bottom). In each plot, the first spectrum was collected in CO/He flow at room temperature. The next five spectra were collected after 1, 3, 5, 7, and 9 min in He at room temperature. The remaining spectra were collected at 100 °C, 200 °C, and 300 °C in He.

relatively lower red shifts when CO adsorbed on a quasi-isolated atom than on a Cu atom interacting with Cu neighbors. They assigned the signal at 2130 cm^{-1} to atomic Cu linked to a paramagnetic O atom of SiO_2.

The catalysts discussed in the present study have been previously characterized [37] by temperature programmed reduction (TPR), *in situ* X-ray diffraction (XRD), and *in situ* X-ray absorption near edge structure (XANES). On the basis of these results, copper species in both Cu/SiO_2 and $CuCo/SiO_2$ are expected to be totally reduced well below the reduction temperature used here, 400 °C. Therefore, the interpretation that CO is adsorbing on Cu_2O is unlikely. It could be that the adsorption sites are copper species made electropositive by interaction with oxygen atoms or hydroxyl groups of the support, or alternatively, they could be copper adatoms at the surface. Intensity transfer effects of the sort described by Hollins [38] could also be masking a $CO\text{-}Cu^0$ signal at lower frequency.

In our prior work [37], TPR and XRD agreed that CuO is fully crystalline in Cu/SiO_2, whereas $CuCo/SiO_2$ contains both crystalline and more dispersed CuO. Although TPR showed some interaction between copper and cobalt phases in $CuCo/SiO_2$, as evidenced by the greatly enhanced reducibility of the latter, XANES showed no evidence of mixed metal oxide formation. The present results show that the stretching frequency and thermal desorption behavior of CO are nearly identical on Cu/SiO_2 and $CuCo/SiO_2$. This suggests that the interaction between copper and cobalt (which promotes the reducibility of cobalt and the dispersion of copper) has little effect on CO chemisorption on copper.

The low stability of the CO-Cu peak at temperatures at and above 200 °C implies a limited ability for this species to participate in the CO hydrogenation reaction, which is usually carried out above 250 °C.

4.3.1.2. Cobalt Sites of Co/SiO_2 and $CuCo/SiO_2$

No peaks due to associatively adsorbed CO are observed after room temperature adsorption on Co/SiO_2, after He flushing at room temperature, or after desorption in He at elevated temperatures. The same is true of $CuCo/SiO_2$. It will be shown that this is due to an activation barrier for CO adsorption on cobalt, which can be overcome at higher temperatures.

4.3.2. CO Hydrogenation

4.3.2.1. Co/SiO_2

Representative DRIFTS spectra during $CO/H_2/He$ flow on Co/SiO_2 are shown in Figure 4.2. Below 200 °C, only peaks due to gas-phase CO and CO_2 are present. At 200 °C, a small peak appears on the low-frequency side of gas phase CO. This peak develops over time at 2070 cm^{-1} with little shift. At 300 °C, the peak shifts toward lower frequencies and intensifies over time to give a broad absorption centered around 2038 cm^{-1}. At 400 °C, peaks due to adsorbed CO disappear and do not return upon cooling to 300 °C.

The peak at 2070 cm^{-1} is too high in frequency to be attributed to CO linearly adsorbed on a clean, reduced, defect-free Co^0 surface. According to experiment and calculation, linear CO on Co^0, both fcc and hcp, normally shows an infrared absorption between 2000 and 2050 cm^{-1} depending on the coverage [25,39-49]. The commonly observed blue shift with increasing coverage of linear CO on Co^0 sites arises from the withdrawal of electrons from cobalt by the adsorbing CO. This results in lower 2π back-donation and a higher stretching frequency. In the case of Co/SiO_2, by contrast, the peak develops at ~2070 cm^{-1} and shifts very little upon increasing exposure time at 200 °C.

The peak at 2070 cm^{-1} falls into a region of the spectrum that has received a variety of interpretations. Peaks in the range 2050-2080 cm^{-1} have been assigned to (1) hydrocarbonyl

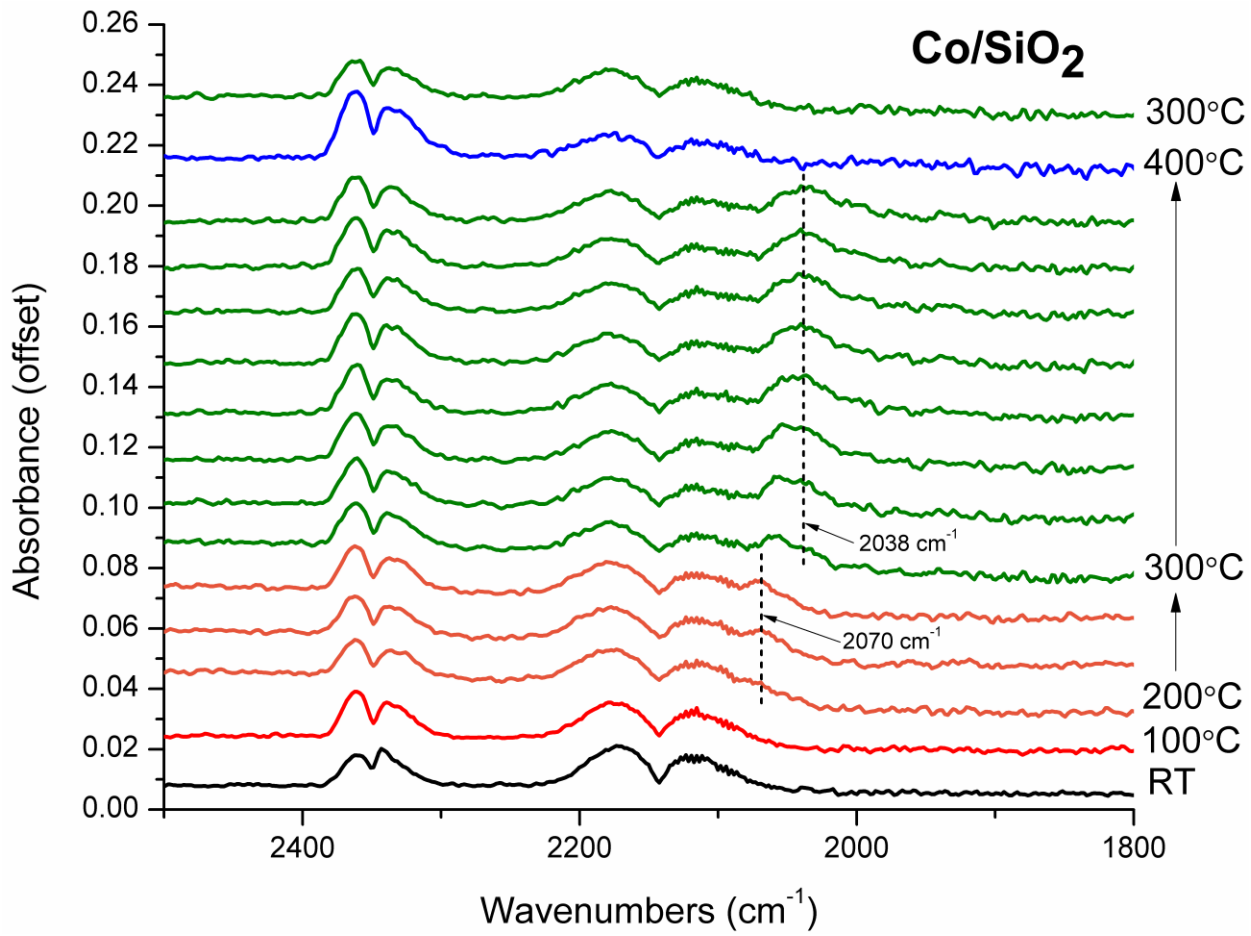

Figure 4.2. Selected DRIFTS spectra during $CO/H_2/He$ flow at 1 atm on Co/SiO_2 at the indicated temperatures. Spectra are in chronological order from bottom to top.

structures, (2) cobalt polycarbonyls [46], particularly when seen in conjunction with lower-frequency bands [50], (3) CO adsorbed on defect sites [44], (4) CO linearly adsorbed on $Co^{\delta+}$ sites [25,39,45,51-53], or on Co^0 in an oxygen-rich environment [54], and (5) some combination of the above [40,41,55]. The literature dealing with each of these species is discussed in turn.

Hydrocarbonyl structures. Adsorption of CO on cobalt in the presence of H_2 can lead to species such as HCo(CO), whose IR absorption at 2050-2060 cm^{-1} appears at the expense of an

ordinary CO-Co^0 band [40]. Such hydrocarbonyl species have been proposed as intermediates in the reaction between CO and H_2 [40] and have been correlated with the formation of CH_4 [24].

To test whether hydrocarbonyl species might be responsible for the peak at 2070 cm^{-1}, the catalyst was exposed to CO/He flow at room temperature, 100 °C, 200 °C, and 300 °C and spectra recorded (Figure 4.3). The peak at 2070 cm^{-1} again appeared, this time at 300 °C. Since the same peak appears in both the presence and the absence of hydrogen, it is unlikely to arise from a hydrocarbonyl species. Nevertheless, the absence of hydrogen retards the development of

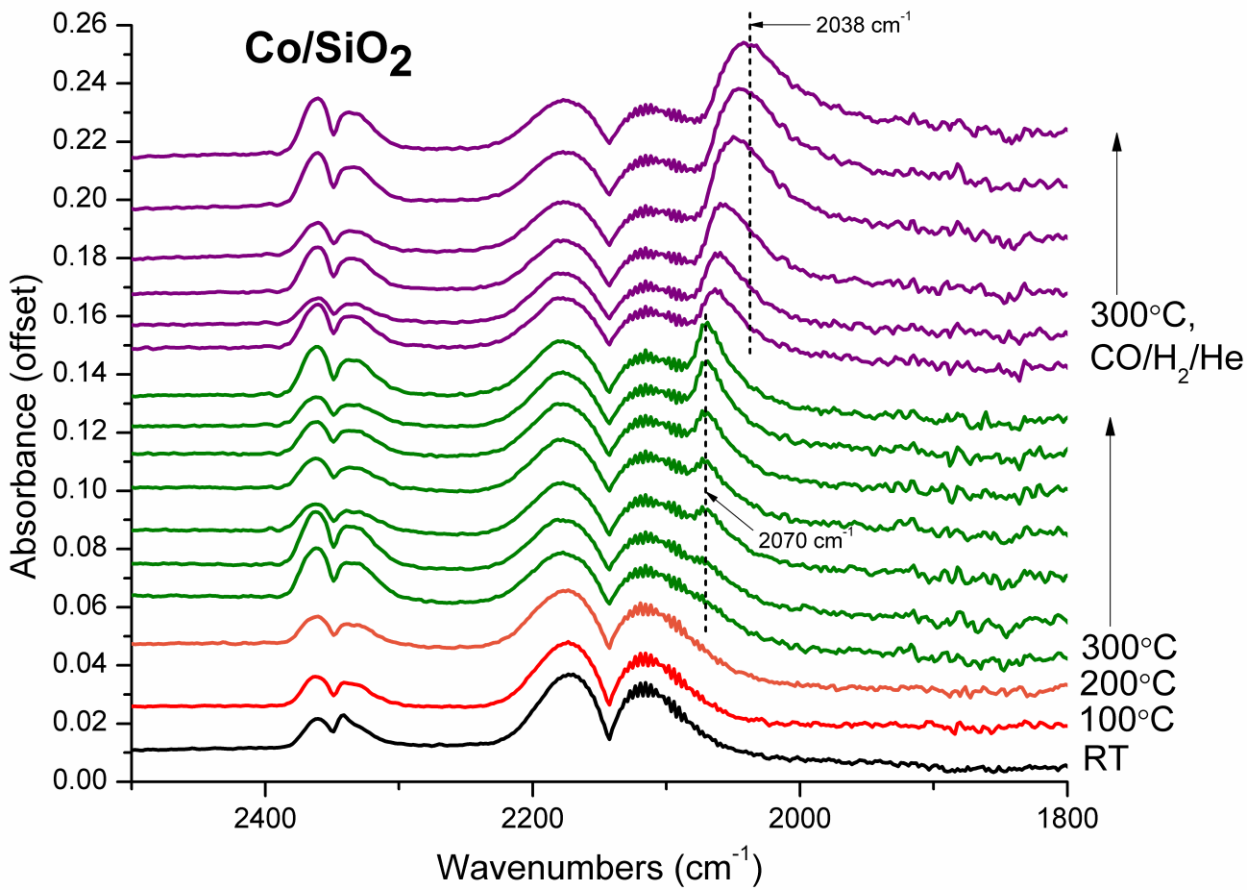

Figure 4.3. Selected DRIFTS spectra during CO/He flow (except where CO/H_2/He flow is explicitly noted) at 1 atm on Co/SiO_2 at the indicated temperatures. Spectra are in chronological order from bottom to top.

this peak, which appears at 200 °C under $CO/H_2/He$ flow. With the introduction of H_2 to the CO/He flow at 300 °C, the peak grows in intensity, broadens, and shifts over time to 2038 cm^{-1}, as in the original CO hydrogenation experiment.

Polycarbonyls; CO on defect sites. Polycarbonyls and CO adsorbed on defect sites are discussed together here since coordinatively unsaturated sites are required to form multinuclear carbonyl species [46,56]. Polycarbonyls are favored by excess CO or prolonged contact time [40,50]. As multiple ligands adsorb per metal site, the electron density back-donated to each decreases, and the stretching frequency increases [50]. In such cases, the higher-frequency symmetric stretching mode should dominate the spectrum, and the intensity of the antisymmetric vibration would be much less [55].

Several authors claim to have observed CO adsorbed on defect sites by infrared spectroscopy [25,26,44]. Beitel et al. [44] and Prieto et al. [25] both present evidence for surface restructuring in CO or syngas at elevated temperatures to yield low-coordination adsorption sites. However, Beitel et al. place the band in question at higher frequency [44] (and Prieto et al. at lower frequency [25]) than CO linearly adsorbed on reduced cobalt sites. Beitel et al. [44] state: "Since it is known that the cobalt—CO bonding contains a substantial degree of back-donation, the defect signal should be shifted to lower frequencies. . . . The reason for this apparent contradiction is not yet clear." The inconsistency could be reconciled if defect-adsorbed polycarbonyls were responsible for the peak seen by Beitel et al. on Co(0001) and defect-adsorbed monocarbonyls for the peak seen by Prieto et al. on zeolite-supported cobalt nanoparticles. Oosterbeek [57], in discussing the results of Beitel et al. [44], refers to the defect species as a geminal dicarbonyl.

CO on $Co^{\delta+}$ sites. An increased CO stretching frequency relative to linear CO on Co^0 would be expected if the cobalt sites themselves were electron deficient, with a reduced capacity

for back-donation to the CO 2π orbital. Such $Co^{\delta+}$ sites may be found at the support interface [25] or near unreduced cobalt ions [58]. The band due to CO-$Co^{\delta+}$ species is reported to be independent of coverage [51], or to exhibit a very weak shift [40]. This type of adsorbed CO may have a lower absorption coefficient than other species, so its amount can easily be underestimated [25].

Co/SiO_2 is expected to contain a mixture of Co^{2+} and Co^0 species after H_2 reduction at 400 °C [37]. It is plausible that the peak at 2070 cm^{-1} in CO/H_2 at 200 °C is due to CO adsorbed on Co^0 sites whose electron density is reduced by proximity to cobalt ions. The continuing shift toward lower frequencies as the temperature is increased and held at 300 °C could be due to an increasing degree of cobalt reduction in CO/H_2. This red shift is unlikely to be an effect of decreasing CO coverage since the peak intensity is increasing.

To verify whether the shift to lower frequency upon increasing temperature from 200 °C to 300 °C was caused by an increasing degree of cobalt reduction, a separate investigation has been conducted into the reversibility of this shift. The CO hydrogenation procedure was repeated up to and including the step at 300 °C. Next, the temperature was returned to 200 °C. After spectral collection in CO/H_2/He flow, the CO component was removed and H_2 allowed to react with the CO remaining on the surface. The sample was cooled to room temperature, and the CO/H_2/He flow was restored. Finally, the sample was heated to 200 °C, then 300 °C, and again cooled to 200 °C.

Selected spectra from this procedure are shown in Figure 4.4. The results are much the same as those for CO hydrogenation (Figure 4.2) up to the first step at 300 °C. The band shifts from about 2039 cm^{-1} at 300 °C to a constant position at 2047 cm^{-1} upon returning to 200 °C. Though a blue shift is observed, it does not return the peak to its original position before heating to 300 °C (which was 2070 cm^{-1}). In other words, the red shift observed upon increasing the

temperature from 200 °C to 300 °C during CO hydrogenation is not perfectly reversible. This confirms that a permanent change has occurred during the step at 300 °C, such as further reduction of the $Co^{\delta+}$ sites.

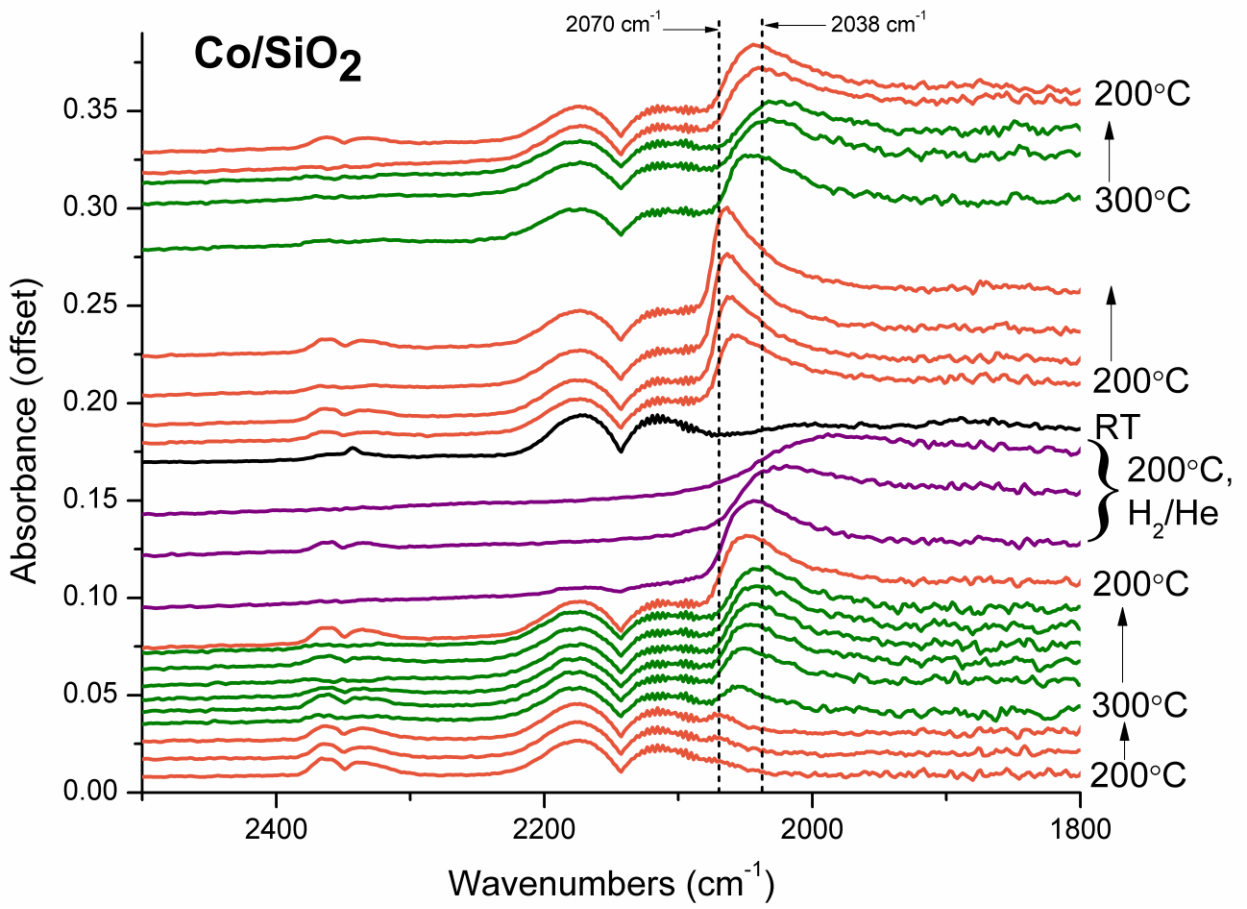

Figure 4.4. Selected DRIFTS spectra collected in flowing gas at 1 atm on Co/SiO_2 at the indicated temperatures. Spectra are in chronological order from bottom to top. Unless otherwise indicated, spectra were collected in $CO/H_2/He$ flow.

Stoppage of CO flow at 200 °C and continuation in H_2/He result in a decrease in the intensity of the adsorbed CO peak accompanied by a shift to lower frequency. Reintroduction of CO at room temperature produces no noticeable changes in the spectrum. This time, upon

heating to 200 °C, CO adsorption is accompanied by a shift from 2058 cm^{-1} to 2067 cm^{-1}. The final frequency is about the same as that observed the first time CO adsorbed at 200 °C (2070 cm^{-1}), but on this occasion, the frequency is approached from lower wavenumbers. This shifting during CO adsorption is more characteristic of reduced cobalt sites. Nevertheless, the frequency range, 2058-2067 cm^{-1}, is still high compared to the expected range of 2000-2050 cm^{-1}.

Heating to 300 °C at once shifts the peak from 2067 cm^{-1} to 2044 cm^{-1}, and continued time at 300 °C shifts it further to 2025 cm^{-1} while decreasing its intensity. This shift is likely produced by two cooperating phenomena: continuing slow reduction at 300 °C and decrease in the coverage of linearly adsorbed CO as reaction intermediates and carbon deposits spread on the surface. Returning to 200 °C shifts the peak to 2040 cm^{-1}.

The observed phenomena can be explained by partially oxidized cobalt becoming more reduced in the presence of CO and hydrogen. Evidently, CO and H_2 act cooperatively to produce this effect. Neither the initial activation in H_2 nor the treatment in CO alone (Figure 4.3) generates these sites but only does the simultaneous presence of H_2 and CO at 300 °C.

4.3.2.2. $CuCo/SiO_2$

Selected spectra during CO hydrogenation on $CuCo/SiO_2$ are shown in Figure 4.5. The room temperature spectrum, in addition to gas phase CO and CO_2, contains a peak at 2123 cm^{-1}. This peak, which is due to CO linearly adsorbed on copper, decreases in intensity at 100 °C and becomes indistinguishable from gas phase CO at 200 °C. This peak shows low thermal stability both in He after room temperature CO adsorption (Figure 4.1) and under CO hydrogenation conditions. Therefore, this species is unlikely to play a major role at reaction temperatures above 200°C and low pressures. The thermal behavior of the copper-adsorbed CO peak on Cu/SiO_2 is similar and is not reproduced here.

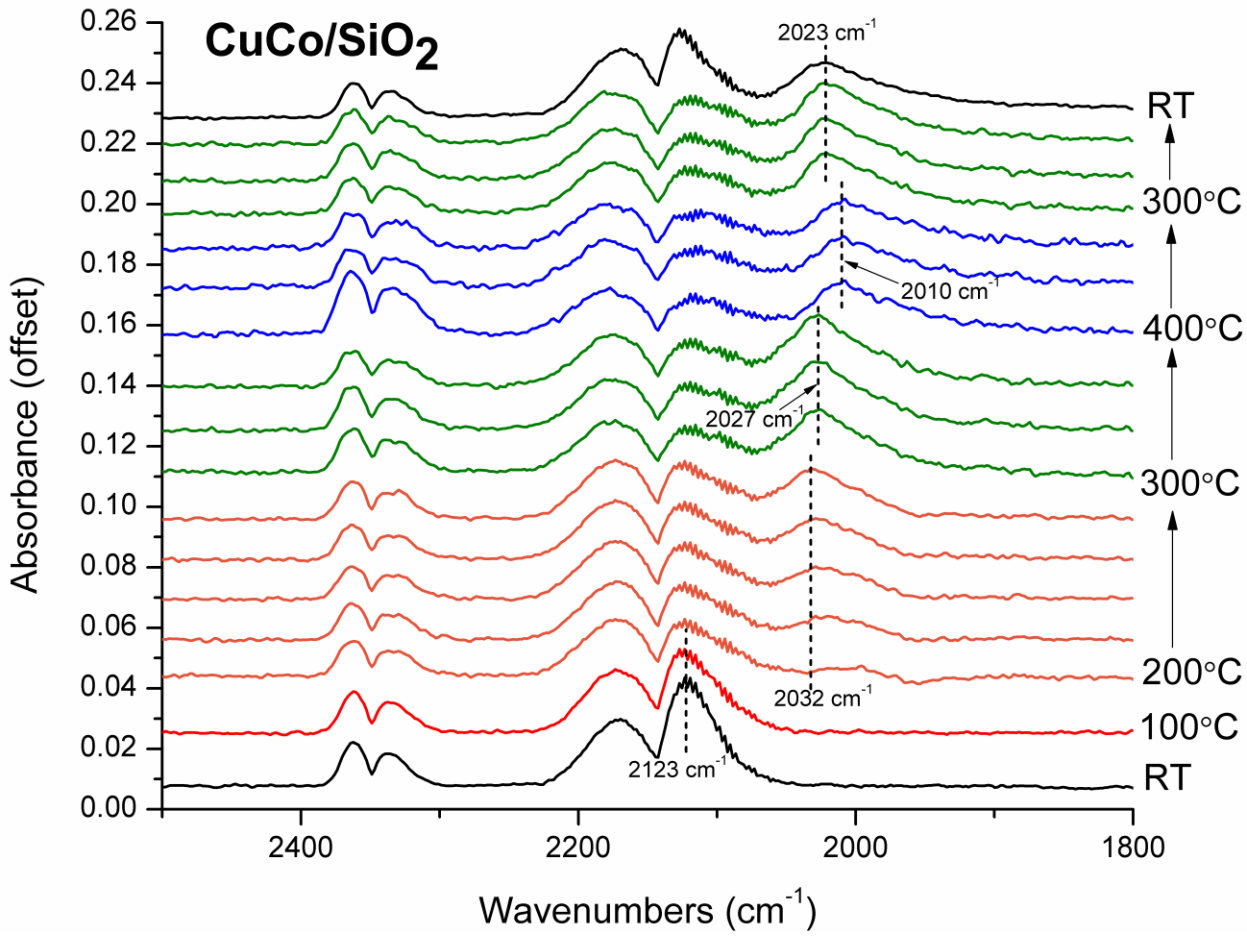

Figure 4.5. Selected DRIFTS spectra during $CO/H_2/He$ flow at 1 atm on $CuCo/SiO_2$ at the indicated temperatures. Spectra are in chronological order from bottom to top.

At 200 °C, a broad new peak appears at about 2000 cm^{-1} on $CuCo/SiO_2$. This peak is soon dominated by a second one at about 2018 cm^{-1}, which shifts over time to 2032 cm^{-1}. The spectral range and blue-shifting behavior of this peak are characteristic of CO linearly adsorbed on a Co^0 surface.

At 300 °C, this peak becomes more intense and, after initially shifting to 2027 cm^{-1}, remains at that position over time. The peak is broadened, with a shoulder on the low-frequency

side. The constant peak position at 300 °C contrasts with the continuous shifting observed for Co/SiO_2 at the same temperature (Figures 4.2 and 4.4). This implies that the site modification occurring on Co/SiO_2 is not a factor on $CuCo/SiO_2$, consistent with the previous finding [37] that copper acts as a reduction promoter for cobalt, which on $CuCo/SiO_2$ is expected to be completely reduced by the H_2/He pretreatment at 400 °C.

At 400 °C, the peak shifts to 2010 cm^{-1} and decreases in intensity. Upon returning to 300 °C, the peak position shifts back toward higher frequency (2023 cm^{-1}) and regains some of its intensity. This reversibility distinguishes $CuCo/SiO_2$ from Co/SiO_2, on which the DRIFTS peak is lost permanently after heating to 400 °C in CO/H_2/He.

The peak due to $CO\text{-}Co^0$ adsorbed at higher temperature remains at 2023 cm^{-1} after cooling to room temperature. In addition, CO adsorbs on copper again at 2127 cm^{-1}.

4.3.2.3. Methanation Observed by Mass Spectrometer (MS) During CO Hydrogenation

The most thermodynamically favorable product of CO hydrogenation (and the only one besides CO_2 observed by MS at the atmospheric pressure conditions of this DRIFTS study) is methane. Figure 4.6 compares the methane production by $CuCo/SiO_2$ and Co/SiO_2 during CO hydrogenation at different temperatures.

Upon heating to 300 °C in flowing CO/H_2/He, the methane production increases on Co/SiO_2 and subsequently falls off, whereas on $CuCo/SiO_2$, it increases to a lower, but steadier, level. This could be explained by enhanced CO dissociation on the sites of Co/SiO_2 relative to $CuCo/SiO_2$. The ease of CO dissociation on Co/SiO_2 might contribute to the nucleation and growth of carbon deposits on this catalyst, leading to the observed decrease in methanation activity with time.

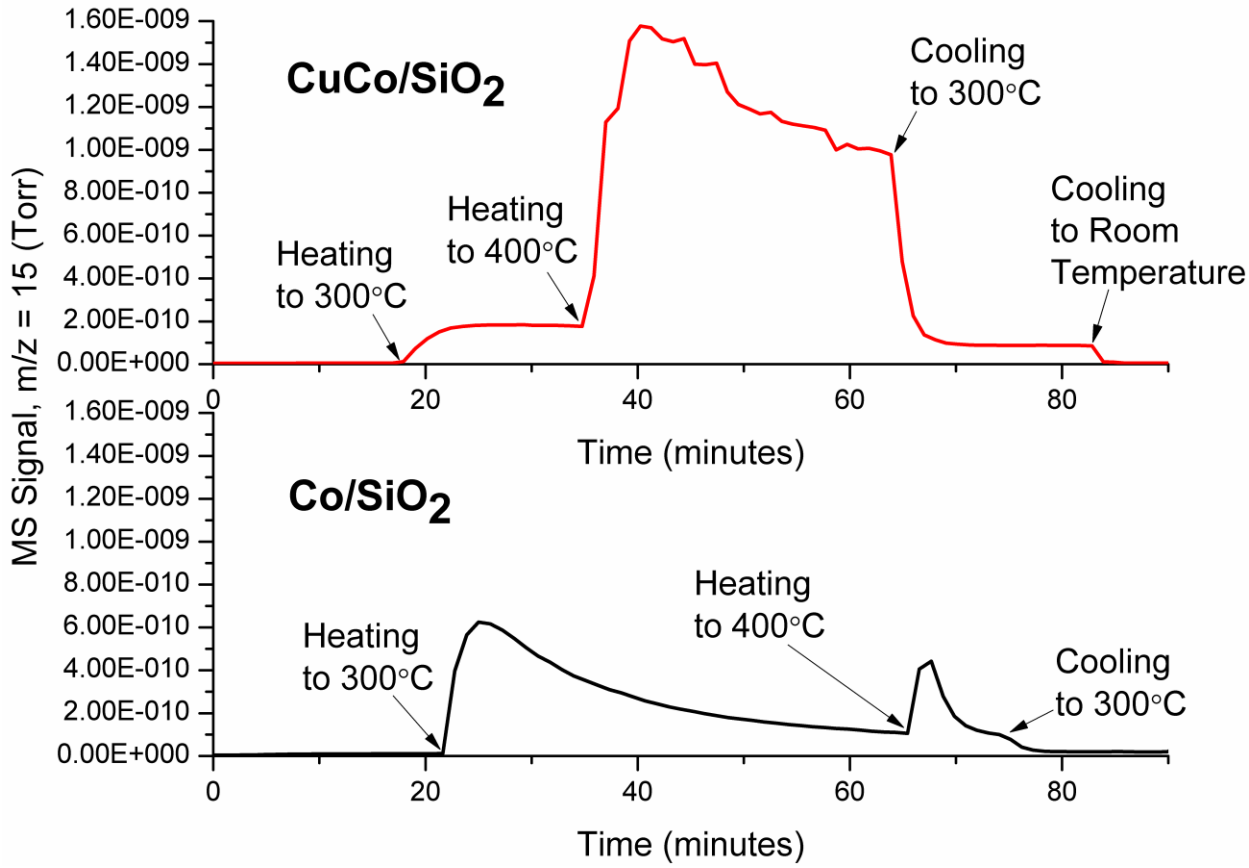

Figure 4.6. Methanation activity on $CuCo/SiO_2$ (top) and Co/SiO_2 (bottom), both reduced at 400 °C, measured by MS during the CO hydrogenation experiments represented in Figures 4.2 and 4.5.

Dissociated CO cannot be observed by DRIFTS, so the sites responsible for this mode of adsorption are not necessarily the same sites that linearly adsorb CO in Figures 4.2-4.4. Indeed, when the CO hydrogenation procedure (up to 400 °C in $CO/H_2/He$) was repeated on a sample of Co/SiO_2 prereduced in H_2/He at 300 °C instead of 400 °C, no peaks due to absorbed CO were seen by DRIFTS. Nevertheless, methane formation was observed by MS (Figure 4.7).

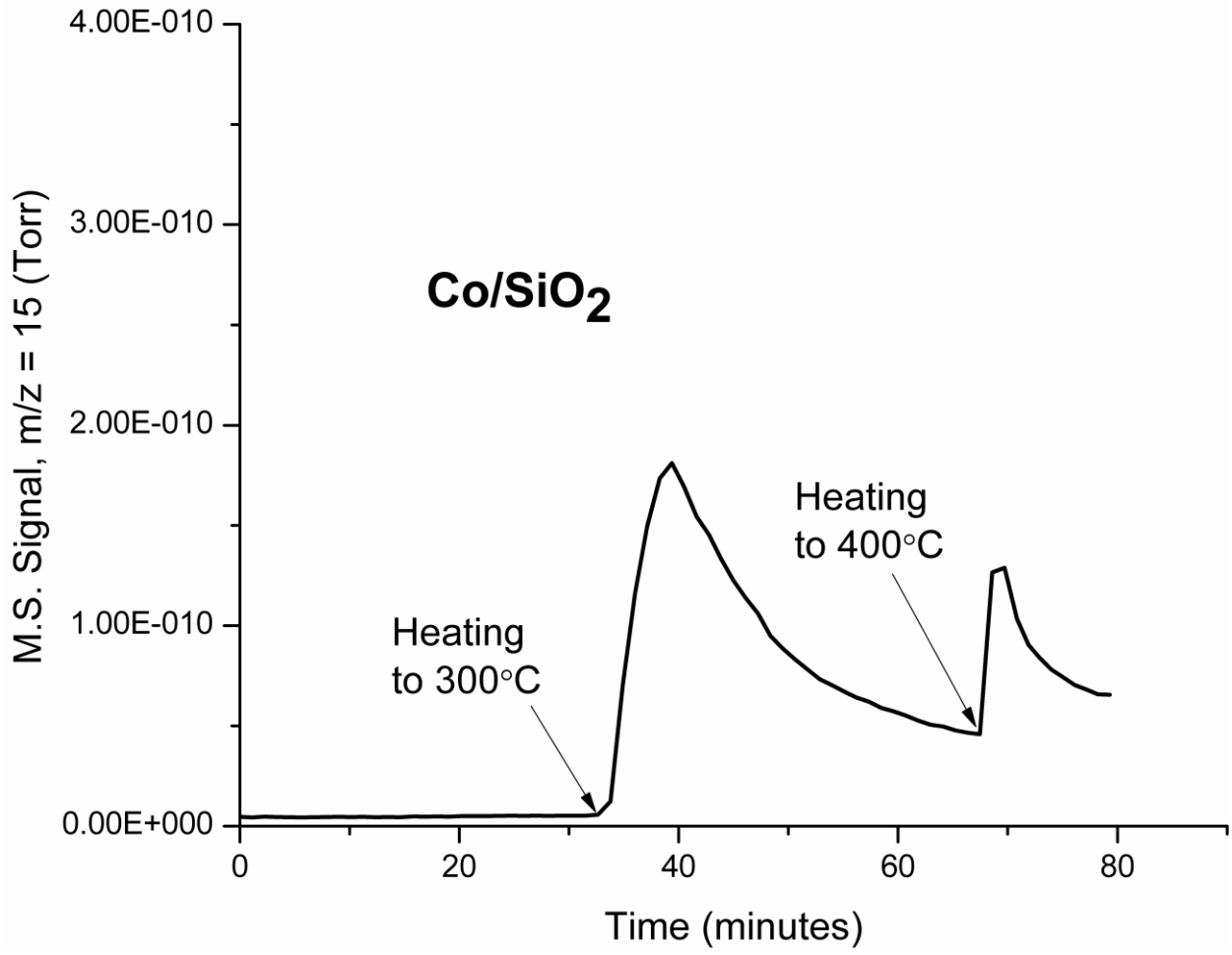

Figure 4.7. Methanation activity on Co/SiO_2 reduced at 300 °C, measured by MS during $CO/H_2/He$ flow at 1 atm.

On the basis of prior literature, we propose that the main sites at which CO dissociation occurs are coordinatively unsaturated sites. One DFT study [59] predicted that CO can dissociate directly on a stepped Co(0001) surface because the transition state associated with this process is of lower energy than CO in the gas phase. By contrast, there is a high activation barrier for dissociation on the flat surface. Beitel et al. [26,44] also observed that a defective Co(0001) surface can more easily dissociate CO than a defect-free surface. On the basis of these computational and experimental results, it seems reasonable that an increase in CO dissociation activity could

be due to an increased concentration of coordinatively unsaturated sites, such as steps, corners, and defects.

The reduced ability of cobalt sites to dissociate CO upon the addition of copper could be due to a reduced tendency toward defect formation during the fast reduction of cobalt oxides on $CuCo/SiO_2$. Alternatively, the defect sites could be blocked by copper atoms. Because of the barrier to CO dissociation on defect-free sites, the methane level is initially lower on $CuCo/SiO_2$ than on Co/SiO_2. Carbon deposition is also less likely on $CuCo/SiO_2$ because of the absence of the ready source of dissociated CO supplied by low-coordinated sites. As a result, the deactivation of $CuCo/SiO_2$ is not as pronounced as that of Co/SiO_2. Blockage of the cobalt surface by copper atoms might also interfere with the growth of graphitic deposits [60].

At 400 °C, the reduction in methanation activity of Co/SiO_2 compared with $CuCo/SiO_2$ is especially distinct. At the same temperature, the DRIFTS peak on Co/SiO_2 disappears irreversibly (Figure 4.2). The disappearance is due to deactivation, not simple desorption, since the peak cannot be recovered by returning to 300 °C. On $CuCo/SiO_2$, heating to 400 °C reduces but does not eliminate the intensity of the CO-Co^0 peak, which can be partially restored by returning to 300 °C. This observation is consistent with a lower tendency toward deactivation by coking of $CuCo/SiO_2$.

4.3.2.4. Comparison of Co/SiO_2 and $CuCo/SiO_2$

The band assignments of CO adsorbed on cobalt in each catalyst during CO hydrogenation are summarized in Table 4.1.

CO does not adsorb associatively in DRIFTS-detectable quantities on cobalt sites of either catalyst at room temperature. On both catalysts, adsorbed CO is seen starting at 200 °C,

increases in intensity at 300 °C, and decreases in intensity at 400 °C under CO hydrogenation conditions. These are signs of activated chemisorption on cobalt [58].

Table 4.1. Assignments of vibrational bands due to CO adsorbed on cobalt observed during CO hydrogenation at 1 atm on Co/SiO_2 and $CuCo/SiO_2$ catalysts.

	Co/SiO_2		$CuCo/SiO_2$	
200 °C	2070 cm^{-1}	CO on $Co^{\delta+}$ sites	2018 cm^{-1}, shifting to 2032 cm^{-1}	CO on Co^0 sites
300 °C	2057 cm^{-1}, shifting to 2038 cm^{-1}	CO on $Co^{\delta+}$ sites transforming to Co^0 sites	2027 cm^{-1}	CO on more strongly adsorbing Co^0 sites
400 °C	--	--	2010 cm^{-1}	Most stable CO species on Co^0

On both Co/SiO_2 and $CuCo/SiO_2$, the band shifts to lower frequencies whenever the temperature is raised. On average, that is, the strength of the CO bond is reduced as the temperature increases. The magnitude of the shift varies depending on the relative contributions of two competing effects, one kinetic and one thermodynamic. Increasing temperature enables the activation barrier for CO adsorption to be overcome, which increases CO coverage and tends to shift the peak toward high wavenumbers. At the same time, increasing temperature tends to desorb CO from more weakly binding sites, which shifts the peak toward low wavenumbers. On Co/SiO_2, the irreversible site transformations already noted also account for some of the shift.

The DRIFTS peak for linear CO on cobalt sites appears at lower frequency on $CuCo/SiO_2$ than on Co/SiO_2 at both 200 °C and 300 °C. Since the frequency on $CuCo/SiO_2$ is consistent with CO adsorbed on clean Co^0, it follows that the difference is due to some electron-withdrawing effect on Co/SiO_2, resulting in less effective weakening of the CO bond. This electron-withdrawing effect could arise from neighboring cobalt ions, interaction with O atoms of the support, or coadsorbed ligands such as CO, C, or O. Of these possibilities, cobalt ions and CO dissociation are more likely on Co/SiO_2 than on $CuCo/SiO_2$, consistent with the DRIFTS result.

4.3.3. Catalytic Reaction

CO conversions from each of the three catalysts at different temperatures (with P = 10 bar and GHSV = 24,000 scc/g_{cat}/h) are shown in Figure 4.8. Cu/SiO_2 gives the lowest conversions of all, which is expected on the basis of the very low amount of CO adsorbed on copper at temperatures above 200 °C. Co/SiO_2 gives higher conversion than $CuCo/SiO_2$ by an order of magnitude or more at 250 °C, 275 °C, and 300 °C. In particular, Co/SiO_2 gives 7 times higher methanol yield. However, DRIFTS shows CO adsorbed on the cobalt sites of $CuCo/SiO_2$ at 200-400 °C (Figure 4.5). Therefore, the lower conversion exhibited by $CuCo/SiO_2$ is not due to a deficiency of surface CO. It seems that the presence of copper interferes with the ability of cobalt to hydrogenate surface intermediates.

On all the catalysts, conversion increases with increasing temperature, as expected. Upon returning to 250 °C after CO hydrogenation at 275 °C and 300 °C, Co/SiO_2 shows a reduced CO conversion (0.7%) as compared to the earlier conversion observed at the same temperature (1.1%). The CO conversion on $CuCo/SiO_2$ is unchanged. This finding is consistent with the DRIFTS/MS observation that Co/SiO_2 is more prone to deactivation than $CuCo/SiO_2$.

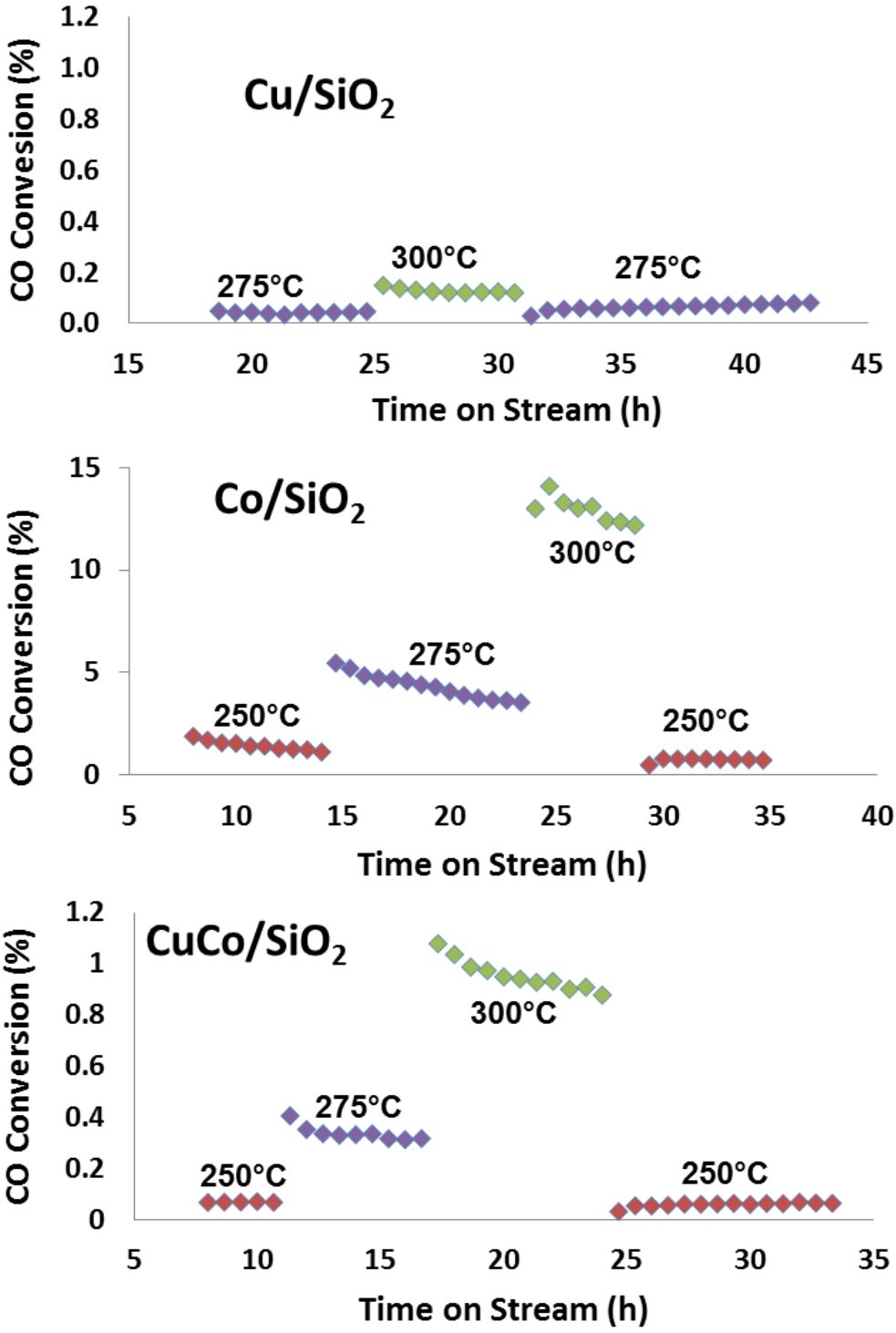

Figure 4.8. CO conversion on Cu/SiO_2, Co/SiO_2, and $CuCo/SiO_2$ at different temperatures. Conditions: P = 10 barg, H_2/CO = 2, GHSV = 24,000 $scc/g_{cat}/h$.

Co/SiO_2 gives higher selectivity to hydrocarbons, including methane, and lower selectivity to methanol, ethanol, and C_{2+} oxygenates than does $CuCo/SiO_2$ (Table 4.2).

Table 4.2. Product selectivities (expressed as carbon efficiencies) on Cu/SiO_2, Co/SiO_2, and $CuCo/SiO_2$ [a].

		CO_2	MeOH	EtOH	C_{2+} Oxygenates	CH_4	C_{2+} Hydrocarbons
Cu/SiO_2	275 °C	6.3	14.6	9.4	0	41.2	28.4
	300 °C	3.6	14.5	6.9	0.2	46.6	28.2
	275 °C (repeat)	5.1	19.9	8.1	0	40.7	26.2
Co/SiO_2	250 °C	1.4	5.0	1.7	1.7	52.2	38.0
	275 °C	1.3	3.3	1.3	1.0	56.5	36.6
	300 °C	1.9	2.6	1.2	0.8	59.1	34.4
	250 °C (repeat)	1.4	4.4	1.5	1.5	53.1	38.1
$CuCo/SiO_2$	250 °C	6.1	8.3	5.9	2.2	47.2	30.3
	275 °C	3.0	6.1	4.3	1.7	50.0	34.9
	300 °C	2.8	5.2	3.3	1.7	53.5	33.5
	250 °C (repeat)	4.8	10.9	6.3	3.1	46.4	28.5

[a]Conditions: P = 10 barg, $H_2/CO = 2$, GHSV = 24,000 $scc/g_{cat}/h$. C_{2+} oxygenates analyzed include acetaldehyde, acetone, isopropyl alcohol, *n*-propanol, isobutyl alcohol, and *n*-butanol. C_{2+} hydrocarbons include ethane, propane, propylene, isobutane, *n*-butane, and *n*-hexane.

Considering that the stretching frequency of adsorbed CO is consistently lower on $CuCo/SiO_2$ than on Co/SiO_2, the CO bond should weaken more when linearly adsorbed on $CuCo/SiO_2$. However, the selectivity to oxygenates is higher on $CuCo/SiO_2$, and the selectivity to

hydrocarbons (including methane) is consistently higher on Co/SiO_2. This is at odds with the expectation (from DRIFTS) that dissociation of *linearly adsorbed* CO is more likely on $CuCo/SiO_2$ than on Co/SiO_2 but could be explained if another type of site on Co/SiO_2 (different from the one seen by DRIFTS) is responsible for direct CO dissociation and hydrocarbon formation on this catalyst. This reinforces the conclusion already drawn from Figures 4.6 and 4.7, i.e., that CO is able to dissociate directly, without first adsorbing in linear form, on certain sites of Co/SiO_2, perhaps coordinatively unsaturated ones.

This is also consistent with the observation that $CuCo/SiO_2$ gives a higher ethanol-to-methanol ratio than does Co/SiO_2. On Co/SiO_2, that is, CO adsorbs associatively and dissociatively but not necessarily at the same site. In fact, the $Co^{\delta+}$ sites may well be active for oxygenate formation, the oxygenate *yield* being highest on Co/SiO_2. However, the catalyst is not very selective due to the existence of another site highly active for CO dissociation and hydrocarbon formation. On $CuCo/SiO_2$, CO is more likely to dissociate at the same sites where CO associatively adsorbs, increasing the probability of CO insertion and ethanol formation.

With increasing temperature on both catalysts, the methane selectivity increases, while selectivity to oxygenates decreases (Table 4.2). From Table 4.3, the chain growth probability of hydrocarbons on Co/SiO_2 decreases upon increasing the temperature from 275 °C to 300 °C. The chain growth probabilities of alcohols on both catalysts, and of hydrocarbons on $CuCo/SiO_2$, are less affected by the increase in temperature. Boz [61] found an alcohol chain growth probability factor that was constant with respect to conversion and a decreasing hydrocarbon α that converged to the alcohol value at high conversions. Boz concluded that there is one active site for alcohol formation and two sites, or one site being modified at high conversion, for hydrocarbon synthesis.

Table 4.3. Chain growth probability factors, assuming Anderson-Schulz-Flory distributions of linear alcohols C_1-C_4 and of normal paraffins C_2-C_4 and C_6.

	Co/SiO_2		CuCo/SiO2	
	Hydrocarbons	Alcohols	Hydrocarbons	Alcohols
275 °C	0.77	0.29	0.48	0.20
300 °C	0.54	0.26	0.45	0.21

4.4. Conclusions

Cu/SiO_2, Co/SiO_2, and $CuCo/SiO_2$ catalysts have been studied by DRIFTS. CO adsorption at room temperature followed by heating in He resulted in a single band at the same position on both Cu/SiO_2 and $CuCo/SiO_2$; this species largely desorbed below CO hydrogenation temperatures on both catalysts. The presence of cobalt did not markedly affect the CO adsorption behavior of the copper sites.

Exposure to CO at room temperature did not produce any bands attributable to CO on cobalt sites on either Co/SiO_2 or $CuCo/SiO_2$. Heating in CO/H_2/He yielded bands due to CO on cobalt sites, starting at 200 °C in both cases, with some differences between the two catalysts. Linearly adsorbed CO bound more weakly to cobalt on Co/SiO_2 than on $CuCo/SiO_2$, probably due to the lower degree of reduction of the former catalyst. Continuous red shifting at 300 °C was attributed to continuing slow reduction of Co/SiO_2. Heating to 400 °C caused partial desorption of CO from $CuCo/SiO_2$ but total deactivation of Co/SiO_2.

CO conversions increased in the order $Cu/SiO_2 < CuCo/SiO_2 < Co/SiO_2$. Because CO adsorption was similar on copper sites with and without cobalt and CO seemed to be thermally unstable on these sites, selectivity differences between $CuCo/SiO_2$ and Co/SiO_2 were explained

by differences in CO binding to cobalt sites. $Co^{\delta+}$ sites of Co/SiO_2 favored high oxygenate yields, but another type of site leading to direct CO dissociation contributed to high hydrocarbon selectivity on this catalyst. The well-reduced Co^0 sites of $CuCo/SiO_2$ bound CO more strongly, leading to increased probability of CO adsorbed associatively and dissociatively at the same type of site. Consequently, ethanol selectivity was higher on this catalyst.

4.5. References

1. Courty, P.; Durand, D.; Freund, E.; Sugier, A. *J. Mol. Catal.* **1982**, *17*, 241.

2. Sheffer, G. R.; King, T. S. *Appl. Catal.* **1988**, *44*, 153.

3. Chu, W.; Kieffer, R.; Kiennemann, A.; Hindermann, J. P. *Appl. Catal., A* **1995**, *121*, 95.

4. Tien-Thao, N.; Alamdari, H.; Zahedi-Niaki, M. H.; Kaliaguine, S. *Appl. Catal., A* **2006**, *311*, 204.

5. Tien-Thao, N.; Zahedi-Niaki, M. H.; Alamdari, H.; Kaliaguine, S. *Appl. Catal., A* **2007**, *326*, 152.

6. Shi, L. M.; Chu, W.; Deng, S. Y.; Xu, H. Y. *J. Nat. Gas Chem.* **2008**, *17*, 397.

7. Deng, S. Y.; Chu, W.; Xu, H. Y.; Shi, L. M.; Huang, L. H. *J. Nat. Gas Chem.* **2008**, *17*, 369.

8. Dong, X.; Liang, X. L.; Li, H. Y.; Lin, G. D.; Zhang, P.; Zhang, H. B. *Catal. Today* **2009**, *147*, 158.

9. Subramanian, N. D.; Balaji, G.; Kumar, C. S. S. R.; Spivey, J. J. *Catal. Today* **2009**, *147*, 100.

10. Fang, Y. Z.; Liu, Y.; Zhang, L. H. *Appl. Catal., A* **2011**, *397*, 183.

11. Spivey, J. J.; Egbebi, A. *Chem. Soc. Rev.* **2007**, *36*, 1514.

12. Kiennemann, A.; Diagne, C.; Hindermann, J. P.; Chaumette, P.; Courty, P. *Appl. Catal.* **1989**, *53*, 197.

13. Xiaoding, X.; Doesburg, E. B. M.; Scholten, J. J. F. *Catal. Today* **1987**, *2*, 125.

14. Dalmon, J. A.; Chaumette, P.; Mirodatos, C. *Catal. Today* **1992**, *15*, 101.

15. Chaumette, P.; Courty, P.; Kiennemann, A.; Kieffer, R.; Boujana, S.; Martin, G. A.; Dalmon, J. A.; Meriaudeau, P.; Mirodatos, C.; Holhein, B.; Mausbeck, D.; Hubert, A. J.; Germain, A.; Noels, A. *Ind. Eng. Chem. Res.* **1994**, *33*, 1460.

16. Mouaddib, N.; Perrichon, V.; Martin, G. A. *Appl. Catal., A* **1994**, *118*, 63.

17. Bailliard-Letournel, R. M.; Cobo, A. J. G.; Mirodatos, C.; Primet, M.; Dalmon, J. A. *Catal. Lett.* **1989**, *2*, 149.

18. Blanchard, M.; Derule, H.; Canesson, P. *Catal. Lett.* **1989**, *2*, 319.

19. Baker, J. E.; Burch, R.; Hibble, S. J.; Loader, P. K. *Appl. Catal.* **1990**, *65*, 281.

20. Mouaddib, N.; Perrichon, V.; Primet, M. *J. Chem. Soc. Faraday T. 1* **1989**, *85*, 3413.

21. Cao, R.; Pan, W. X.; Griffin, G. L. *Langmuir* **1988**, *4*, 1108.

22. Llorca, J.; Homs, N.; Rossell, O.; Seco, M.; Fierro, J. L. G.; de la Piscina, P. R. *J. Mol. Catal. A: Chem.* **1999**, *149*, 225.

23. Figueiredo, R. T.; Granados, M. L.; Fierro, J. L. G.; Vigas, L.; de la Piscina, P. R.; Homs, N. *Appl. Catal., A* **1998**, *170*, 145.

24. Song, D.; Li, J.; Cai, Q. *J. Phys. Chem. C* **2007**, *111*, 18970.

25. Prieto, G.; Martínez, A.; Concepción, P.; Moreno-Tost, R. *J. Catal.* **2009**, *266*, 129.

26. Beitel, G. A.; de Groot, C. P. M.; Oosterbeek, H.; Wilson, J. H. *J. Phys. Chem. B* **1997**, *101*, 4035.

27. Topsøe, N. Y.; Topsøe, H. *J. Mol. Catal. A: Chem.* **1999**, *141*, 95.

28. Scarano, D.; Bordiga, S.; Lamberti, C.; Spoto, G.; Ricchiardi, G.; Zecchina, A.; Arean, C. O. *Surf. Sci.* **1998**, *411*, 272.

29. Padley, M. B.; Rochester, C. H.; Hutchings, G. J.; King, F. *J. Catal.* **1994**, *148*, 438.

30. Dandekar, A.; Vannice, M. A. *J. Catal.* **1998**, *178*, 621.

31. Hadjiivanov, K.; Tsoncheva, T.; Dimitrov, M.; Minchev, C.; Knozinger, H. *Appl. Catal., A* **2003**, *241*, 331.

32. Tsoncheva, T.; Venkov, T.; Dimitrov, M.; Minchev, C.; Hadjiivanov, K. *J. Mol. Catal. A: Chem.* **2004**, *209*, 125.

33. Boccuzzi, F.; Coluccia, S.; Martra, G.; Ravasio, N. *J. Catal.* **1999**, *184*, 316.

34. de Jong, K. P.; Geus, J. W.; Joziasse, J. *Appl. Surf. Sci.* **1980**, *6*, 273.

35. Greeley, J.; Gokhale, A. A.; Kreuser, J.; Dumesic, J. A.; Topsøe, H.; Topsøe, N. Y.; Mavrikakis, M. *J. Catal.* **2003**, *213*, 63.

36. Ferullo, R. M.; Castellani, N. J. *J. Mol. Catal. A: Chem.* **2005**, *234*, 121.

37. Smith, M. L.; Campos, A.; Spivey, J. J. *Catal. Today* **2012**, *182*, 60.

38. Hollins, P. *Surf. Sci. Rep.* **1992**, *16*, 51.

39. Jiang, M.; Koizumi, N.; Ozaki, T.; Yamada, M. *Appl. Catal., A* **2001**, *209*, 59.

40. Kadinov, G.; Bonev, C.; Todorova, S.; Palazov, A. *J. Chem. Soc. Faraday T.* **1998**, *94*, 3027.

41. Rodrigues, E. L.; Bueno, J. M. C. *Appl. Catal., A* **2002**, *232*, 147.

42. Bian, G.; Nanba, T.; Koizumi, N.; Yamada, M. *J. Mol. Catal. A: Chem.* **2002**, *178*, 219.

43. Khodakov, A. Y.; Lynch, J.; Bazin, D.; Rebours, B.; Zanier, N.; Moisson, B.; Chaumette, P. *J. Catal.* **1997**, *168*, 16.

44. Beitel, G. A.; Laskov, A.; Oosterbeek, H.; Kuipers, E. W. *J. Phys. Chem.* **1996**, *100*, 12494.

45. Zhang, J.; Chen, J.; Ren, J.; Sun, Y. *Appl. Catal., A* **2003**, *243*, 121.

46. Sun, S. L.; Tsubaki, N.; Fujimoto, K. *Appl. Catal., A* **2000**, *202*, 121.

47. Morales, F.; de Smit, E.; de Groot, F. M. F.; Visser, T.; Weckhuysen, B. M. *J. Catal.* **2007**, *246*, 91.

48. Sato, K.; Inoue, Y.; Kojima, I.; Miyazaki, E.; Yasumori, I. *J. Chem. Soc. Faraday T. 1* **1984**, *80*, 841.

49. Pick, S. *Surf. Sci.* **2007**, *601*, 5571.

50. Heal, M. J.; Leisegang, E. C.; Torrington, R. G. *J. Catal.* **1978**, *51*, 314.

51. Lapidus, A.; Krylova, A.; Kazanskii, V.; Borovkov, V.; Zaitsev, A.; Rathousky, J.; Zukal, A.; Jancalkova, M. *Appl. Catal.* **1991**, *73*, 65.

52. Mendes, F. M. T.; Perez, C. A. C.; Noronha, F. B.; Souza, C. D. D.; Cesar, D. V.; Freund, H. J.; Schmal, M. *J. Phys. Chem. B* **2006**, *110*, 9155.

53. Xiong, H.; Zhang, Y.; Liew, K.; Li, J. *J. Mol. Catal. A: Chem.* **2008**, *295*, 68.

54. Ansorge, J.; Forster, H. *J. Catal.* **1981**, *68*, 182.

55. Rygh, L. E. S.; Ellestad, O. H.; Klaeboe, P.; Nielsen, C. J. *Phys. Chem. Chem. Phys.* **2000**, *2*, 1835.

56. Risse, T.; Carlsson, A.; Baumer, M.; Kluner, T.; Freund, H. J. *Surf. Sci.* **2003**, *546*, L829.

57. Oosterbeek, H. *Phys. Chem. Chem. Phys.* **2007**, *9*, 3570.

58. Kumar, N.; Jothimurugesan, K.; Stanley, G. G.; Schwartz, V.; Spivey, J. J. *J. Phys. Chem. C* **2010**, *115*, 990.

59. Gong, X.-Q.; Raval, R.; Hu, P. *Surf. Sci.* **2004**, *562*, 247.

60. Swart, J. C. W.; Ciobîcă, I. M.; van Santen, R. A.; van Steen, E. *J. Phys. Chem. C* **2008**, *112*, 12899.

61. Boz, I. *Catal. Lett.* **2003**, *87*, 187.

Chapter 5: Effect of Sn Addition on Cu/SiO_2, Co/SiO_2, and $CuCo/SiO_2$ Catalysts for CO Hydrogenation to Ethanol and Higher Alcohols

5.1. Introduction

Sn has been incorporated into various metal catalysts as a promoter for the selective hydrogenation or hydrogenolysis of unsaturated aldehydes and esters [1-6]. Sn addition increases selectivity for C=O bond hydrogenation to yield unsaturated alcohols, over the thermodynamically favored C=C hydrogenation to yield saturated compounds. This effect has two possible origins: interaction of the O atom of the C=O bond with ionic (Lewis acid) sites of the promoter [2-4], or enhanced C=O adsorption due to increased electron density on the transition metal from interaction with Sn [1,6,7].

CO hydrogenation can also yield alcohols selectively. Over the widely studied copper-cobalt bimetallic catalysts [8-17], ethanol production depends on the atomic-level proximity of CH_x species, formed from dissociated CO, and associatively adsorbed CO. Insertion of adsorbed CO into surface CH_x species leads to ethanol [18,19].

The effect of Sn addition on CO adsorption by copper-cobalt catalysts is not, to our knowledge, reported in the literature. However, application of diffuse reflectance infrared Fourier transform spectroscopy (DRIFTS) to CO adsorbed on Ru-Sn catalysts showed that the Sn/(Ru + Sn) ratio influenced the position and stability of infrared bands [20]. The addition of Sn created a new type of $Ru^{\delta+}$ adsorption center and increased the stability of linearly adsorbed CO-Ru^0 species. In another study, density functional theory (DFT) calculations [21] on copper and copper-tin alloy surfaces predicted stronger CO binding on Cu-terminated CuSn(0001) than on Cu(111). This was largely attributed to the expansive strain on Cu from alloying with Sn. CO

adsorption studies more directly applicable to Sn promotion of copper-cobalt catalysts are currently unavailable.

The objectives of the present work are (i) to study whether the promoting effect of Sn on C=O bond activation in aldehydes and esters also applies to CO adsorption on copper and cobalt, and (ii) to determine whether Sn increases the selectivity of Cu- and Co- based catalysts to ethanol and higher alcohols during CO hydrogenation.

5.2. Materials and Methods

5.2.1. Catalyst Preparation

The preparation of Cu/SiO_2, Co/SiO_2, and $CuCo/SiO_2$ has been described elsewhere [22]. Briefly, these catalysts were prepared by impregnation or coimpregnation of nitrate salts, followed by drying at about 100°C and calcination at 500°C. To prepare the corresponding Sn-promoted catalysts, the active metal nitrate precursors were deposited on the support by impregnation ($CuSn/SiO_2$, $CoSn/SiO_2$) or coimpregnation ($CuCoSn/SiO_2$) with an aqueous nitrate solution. After drying at 100-105°C, a second impregnation was done with $Sn(OOCCH_3)_2$ in an aqueous solution containing a small amount of acetic acid. The catalysts were again dried overnight at 100-105°C, then calcined at 500°C for two hours in stagnant air.

5.2.2. Catalyst Characterization

The bulk compositions were obtained by ICP-OES, which was performed using a Perkin Elmer 2000 DV ICP-optical emission spectrometer.

Catalyst surface areas were determined by flow BET in an Altamira AMI-200 unit. The catalyst (about 40 mg) was first dried in 30 sccm He at 150°C for 30 min. N_2 concentrations of 10%, 20%, and 30% in a He carrier were used for adsorption at liquid nitrogen temperature.

Temperature programmed reduction (TPR) was carried out on 45 mg of sample in an Altamira AMI-200 unit. After drying at 120°C in 30 sccm He for 100 min, the bed was cooled to room temperature. The atmosphere was changed to 30 sccm 10% H_2/Ar and the temperature ramped to 750°C at 10°C/min. A thermal conductivity detector (TCD), calibrated for quantitative analysis by TPR of Ag_2O, was used to evaluate H_2 consumption.

X-ray absorption near edge structure (XANES) spectra were collected at the Co K-edge of $CoSn/SiO_2$ and $CuCoSn/SiO_2$. Measurements were conducted at the Double Crystal Monochromator (DCM) beamline at the LSU J. Bennett Johnston, Sr., Center for Advanced Microstructures and Devices (CAMD) in Baton Rouge, LA. The scan parameters were as follows: 1 eV steps from -50 to -15 eV relative to the edge, 0.5 eV steps from -15 to 50 eV, and 1 eV steps from 50 eV to 100 eV. An integration time of 1 s was allowed at each step. The K-edge spectrum of a cobalt foil was measured simultaneously with the sample. The maximum in the first derivative of this spectrum was shifted to the literature value of the Co K-edge energy (7709 eV) [23], and the corresponding sample spectrum was calibrated accordingly. The spectra were then normalized and analyzed by linear combination fitting (LCF) of their derivatives in Athena (v. 0.8.056) [24]. Co_3O_4 and CoO were used as standards for LCF.

In situ X-ray diffraction, used to characterize reduction of the catalysts, was carried out at the Center for Nanophase Materials Sciences, Oak Ridge National Laboratory, Oak Ridge, TN. The diffractometer was a PANalytical X'Pert Pro MPD equipped with an Anton Paar XRK900 reaction chamber. The sample was exposed to 4% H_2/He flow at temperatures selected on the basis of TPR. Using Cu Kα radiation, XRD patterns were collected at a scan speed of 0.030384°/s with a step size of 0.017°.

5.2.3. *In situ* DRIFTS

Diffuse reflectance infrared Fourier transform spectroscopy (DRIFTS) characterization was done in a Thermo Scientific Nicolet 6700 spectrometer equipped with a Harrick Praying Mantis reaction chamber and a mercury cadmium telluride (MCT-A) detector. The catalyst (25-30 mg) was first reduced *in situ* in 40 sccm 10% H_2/He at 400°C (unless otherwise specified) for 1 h. The system was then purged with 40 sccm He at 400°C for 1 h. Background spectra were collected at 400°C, 300°C, 200°C, 100°C, and room temperature in 40 sccm He. From this point, one of two experiments was conducted:

(1) CO adsorption/desorption. To the 40 sccm of He already flowing, 10 sccm 5% CO/He were added. Spectra were collected in the presence of CO and also after stopping the 5% CO/He, with continuing He flow, at room temperature. Spectra were also taken in He at 100°C, 200°C, 300°C, and 400°C.

(2) CO hydrogenation. To the 40 sccm of He already flowing, 10 sccm 5% CO/He and 10 sccm 10% H_2/He were added. Spectra were collected in this gas composition at room temperature and at elevated temperatures.

All the DRIFTS experiments were carried out at atmospheric pressure. Each spectrum was taken as an average of 64 scans, at a resolution of 4 cm^{-1}. Each of the gases was fitted with an in-line trap (Alltech) for the removal of water, oxygen, and hydrocarbons.

5.2.4. Catalytic Reaction

Catalytic tests were conducted in an Altamira AMI-200R-HP system. The catalyst sample, weighing 150 mg, was loaded into a 1/4" glass-lined reactor tube and reduced at 400°C for one hour in H_2/He. The data reported here were collected at a pressure of 10 bar, reaction temperature of 300°C, gas hourly space velocity of 24,000 scc/h/g_{cat}, and H_2/CO = 2.

Product samples were analyzed online by a Shimadzu GC-2014 gas chromatograph. Hydrocarbons and oxygenates were separated on a Restek Rt-Q-BOND column (25 m × 0.53 mm × 20 μm) and analyzed by a flame ionization detector (FID). CO and CO_2 were analyzed by TCD using He as a carrier.

5.3. Results and Discussion

5.3.1. Composition and Surface Area

The actual bulk compositions of the Sn-promoted catalysts, determined by ICP-OES, are shown in Table 5.1, along with the BET surface areas. The surface areas are in the range 250-270 m^2/g, consistent with those of the unpromoted catalysts [22].

Table 5.1. BET surface areas and ICP-OES compositions of the Sn-promoted catalysts.

Catalyst	S_{BET} (m^2/g)	Composition (wt%)		
		Co	Cu	Sn
$CuSn/SiO_2$	252 ± 9	--	3.29 ± 0.01	2.89 ± 0.25
$CoSn/SiO_2$	262 ± 14	2.99 ± 0.05	--	2.83 ± 0.04
$CuCoSn/SiO_2$	250 ± 3	3.04 ± 0.14	3.36 ± 0.10	2.80 ± 0.03

5.3.2. Temperature Programmed Reduction (TPR)

Figure 5.1 shows TPR results for the Sn-promoted and unpromoted catalysts. The reduction behavior of the unpromoted catalysts has been explained previously [22]. In Co/SiO_2 and $CuCo/SiO_2$, Co_3O_4 reduces to Co^0 via a CoO intermediate. Both reduction steps are catalyzed by copper, particularly the CoO → Co^0 step, such that reduction of all copper and cobalt oxides is essentially simultaneous on $CuCo/SiO_2$. Reduction of bulk crystalline CuO occurs at about the

same temperature (220°C) on both Cu/SiO_2 and $CuCo/SiO_2$. However, the small shoulder on the low temperature side of the profile for $CuCo/SiO_2$ is due to the reduction of a fraction of CuO that is noncrystalline [22]. This is supported by XRD, in which CuO becomes less crystalline upon cobalt addition, and by *in situ* XANES, in which CuO begins reducing to Cu_2O below 200°C in $CuCo/SiO_2$ [22].

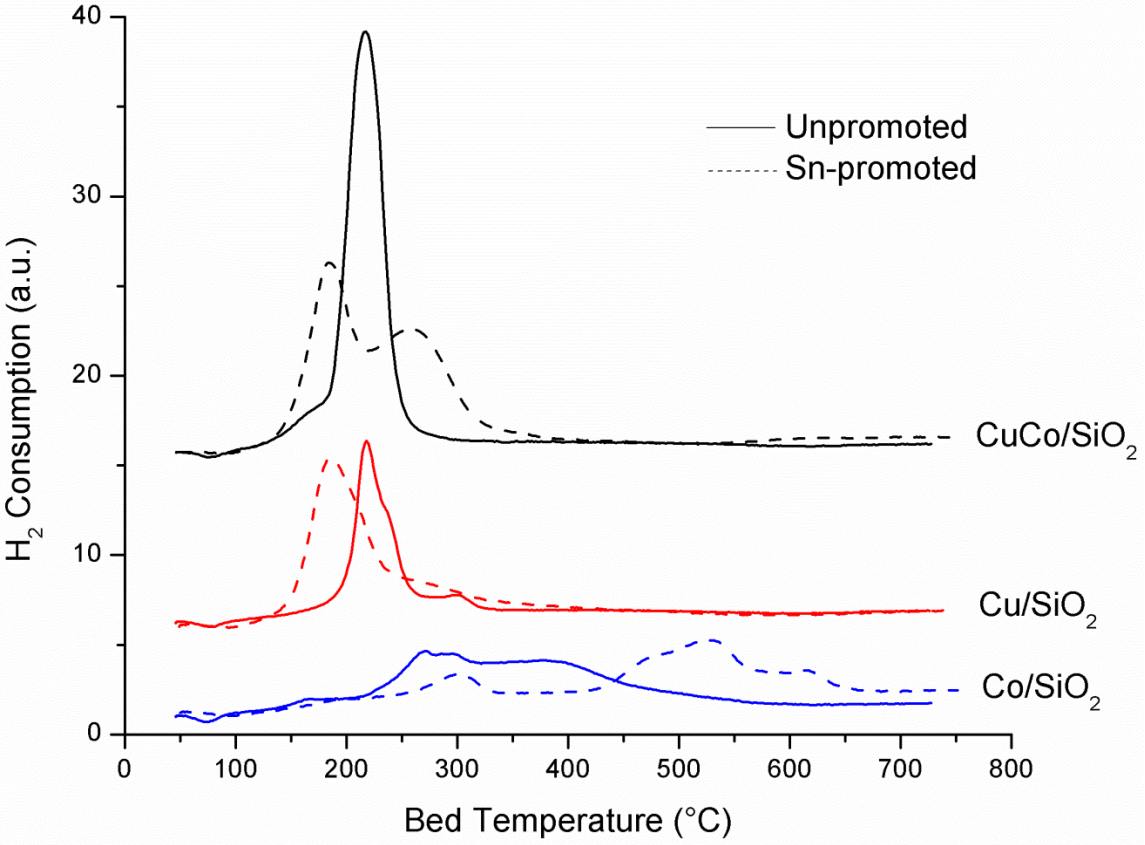

Figure 5.1. TPR profiles of Sn-promoted and unpromoted $CuCo/SiO_2$, Cu/SiO_2, and Co/SiO_2.

The addition of Sn increases the reducibility of copper phases. $CuCoSn/SiO_2$ and $CuSn/SiO_2$ each show a major reduction peak at about 190°C, below the reduction temperature of crystalline CuO and aligning with the shoulder previously attributed to noncrystalline CuO

reduction in $CuCo/SiO_2$. This suggests that CuO in $CuSn/SiO_2$ and $CuCoSn/SiO_2$ is noncrystalline or weakly crystalline.

On the other hand, Sn addition decreases the reducibility of cobalt species in Co/SiO_2. Notably, the feature at around 300°C, corresponding to reduction of Co_3O_4 to CoO, is less intense in the Sn-promoted sample. Since the cobalt loading is the same in both catalysts (2.99 wt%), this implies that the remaining cobalt is in a separate, less reducible phase, such as the cobalt-tin mixed metal oxide, Co_2SnO_4. The three overlapping peaks between 400°C and 700°C can then be assigned to reduction of CoO originating from Co_3O_4, reduction of CoO originating from Co_2SnO_4, and reduction to SnO of SnO_2 originating from Co_2SnO_4, in that order.

On $CuCoSn/SiO_2$, reduction of cobalt species takes place at a higher temperature (about 260°C) than reduction of CuO, which means the contact between copper and cobalt phases is less intimate than in $CuCo/SiO_2$. However, the copper-cobalt interaction is still sufficiently close to increase the reducibility of Co^{2+} species with respect to both Co/SiO_2 and $CoSn/SiO_2$.

The quantitative hydrogen consumption of each Sn-containing catalyst is listed in Table 5.2. The actual H_2 consumption by $CuSn/SiO_2$ is nearly twice that required for reduction of CuO alone. If reduction of SnO_2 to Sn^0 is also considered, the expected H_2 consumption for $CuSn/SiO_2$ becomes 0.90 mmol/g, in better agreement with the observed value. This suggests the high temperature tail on the $CuSn/SiO_2$ profile is due to reduction of Sn species. Without copper promotion, SnO_2 supported on SiO_2 reduces between 600 and 700°C [25]. The H_2 consumption by $CuCoSn/SiO_2$ is also higher than necessary for complete reduction of CuO and Co_3O_4, and reduction of Sn species on this catalyst is also probable. $CoSn/SiO_2$ consumes the amount of H_2 expected to reduce Co_3O_4 to Co^0, but assuming the presence of Co_2SnO_4 also leads to a calculated H_2 consumption (0.74 mmol/g) within the experimental error. It is unlikely that

Sn species reduce fully to Sn^0 on this catalyst, suggesting that the presence of Cu^0 is necessary to promote reduction of tin oxides.

Table 5.2. Quantitative H_2 consumption by the Sn-promoted catalysts during TPR.

Catalyst	H_2 Consumption (mmol/g)	Expected H_2 consumption[a] (mmol/g)
$CuSn/SiO_2$	0.97 ± 0.10	0.52
$CoSn/SiO_2$	0.68 ± 0.20	0.68
$CuCoSn/SiO_2$	1.50 ± 0.25	1.22

[a]H_2 consumption required for complete reduction of Co_3O_4 and CuO to the respective metals.

5.3.3. X-ray Absorption Near Edge Structure (XANES)

Confirmation that Co_3O_4 is not the unique cobalt phase in calcined $CoSn/SiO_2$ comes from the Co K-edge XANES measurement on this catalyst, shown in Figure 5.2. The spectrum of $CoSn/SiO_2$ resembles that of Co_3O_4, except for a prominent shoulder on the low-energy side of the white line. This shoulder is at the position of the CoO white line (about 7725 eV) and might originate from Co^{2+} species. However, a linear combination fit using Co_3O_4 and CoO as standards does not yield a satisfactory fit to the spectrum of $CoSn/SiO_2$. Therefore, the most likely explanation seems to be the incorporation of some cobalt into a mixed metal oxide with tin (the spinel Co_2SnO_4, in which cobalt is divalent and tin is tetravalent). The same is true for $CuCoSn/SiO_2$, whose XANES spectrum (not shown) is similar to that of $CoSn/SiO_2$.

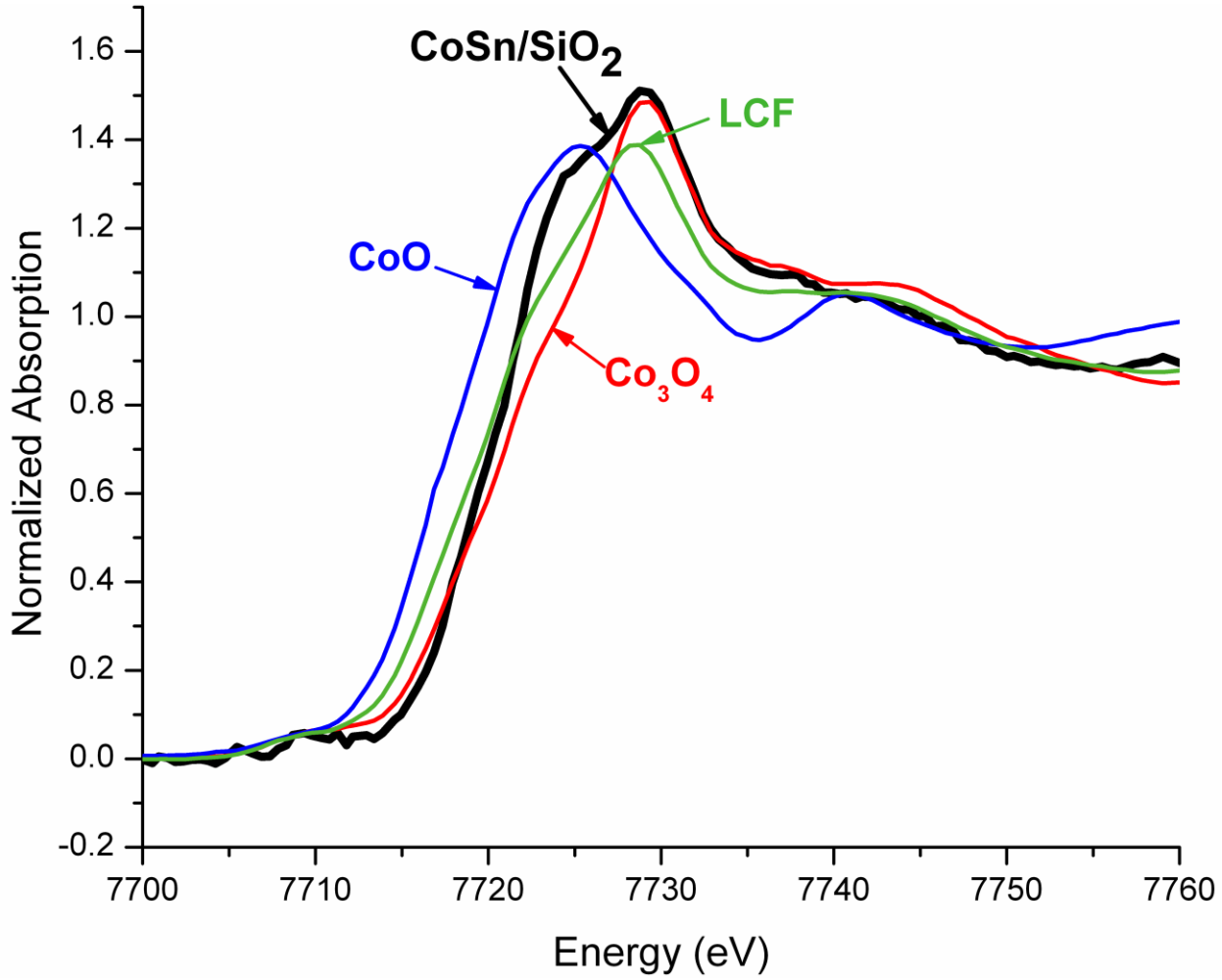

Figure 5.2. Co K-edge spectrum of $CoSn/SiO_2$, together with spectra of Co_3O_4 and CoO standards. A linear combination fit of the $CoSn/SiO_2$ spectrum to the standards is also shown for reference.

5.3.4. *In situ* X-ray Diffraction (XRD)

The XRD patterns of the Sn-promoted catalysts are shown in Figures 5.3-5.5. The XRD peaks representing copper and cobalt phases in all the Sn-promoted catalysts are quite broad, similar to the feature at $2\theta = 20°\text{-}30°$ corresponding to weakly ordered SiO_2. Concerning the copper phases, this is consistent with TPR results showing that Sn addition decreases the crystallinity and increases the dispersion. The CuO, and eventually Cu^0, "crystallites" in

$CuSn/SiO_2$ have diameters <4 nm based on the Scherrer equation. In the Sn-free catalysts, the CuO crystallite diameters range from about 20 nm ($CuCo/SiO_2$) to 25 nm (Cu/SiO_2) [22]. Sn addition also increases the dispersion of the cobalt phases. In $CoSn/SiO_2$, Co_3O_4 crystallites are 5-7 nm, and Co^0 crystallites, when they form, are 3-5 nm in size. On the other hand, Co_3O_4 crystallites are 11-16 nm in diameter in Co/SiO_2 and $CuCo/SiO_2$. In $CuCoSn/SiO_2$, the peaks broaden to such an extent that there is overlap even between copper and cobalt oxides. Clearly, Sn addition promotes the dispersion of the active metals.

The Sn itself is also highly dispersed, as peaks corresponding to Sn phases cannot be uniquely and unambiguously identified from the XRD patterns. However, SnO_2 has intense lines near 26.7° and 34.1° [25-28] and might contribute to the broad oxide peaks below $2\theta = 40°$ in $CuSn/SiO_2$. Similarly, Co_2SnO_4 has a reflection near 34.6° [29] and may contribute to the oxide peaks in the $CoSn/SiO_2$ and $CuCoSn/SiO_2$ patterns. However, when these phases reduce, no peak appears at 32.0°, corresponding to Sn^0 [25].

Figure 5.3 shows that the CuO initially present in $CuSn/SiO_2$ reduces to Cu^0 at 200°C. In agreement with TPR, the signal at low 2θ value (probably corresponding to a tin oxide phase) is the last to disappear. Reduction is mostly complete by 250°C. Above this temperature metallic copper slowly crystallizes.

Figure 5.4 shows an initial Co_3O_4 phase in $CoSn/SiO_2$ transforming to CoO at 275°C. At about 450°C, CoO begins reducing to Co^0, coinciding with the onset of the second TPR peak. From XRD, CoO reduction continues through 500°C. This suggests that the CoO originating from Co_2SnO_4 is highly dispersed and barely detectable by XRD, since reduction of this species continues beyond 550°C in TPR. Slow crystallization of Co^0 occurs up to 700°C.

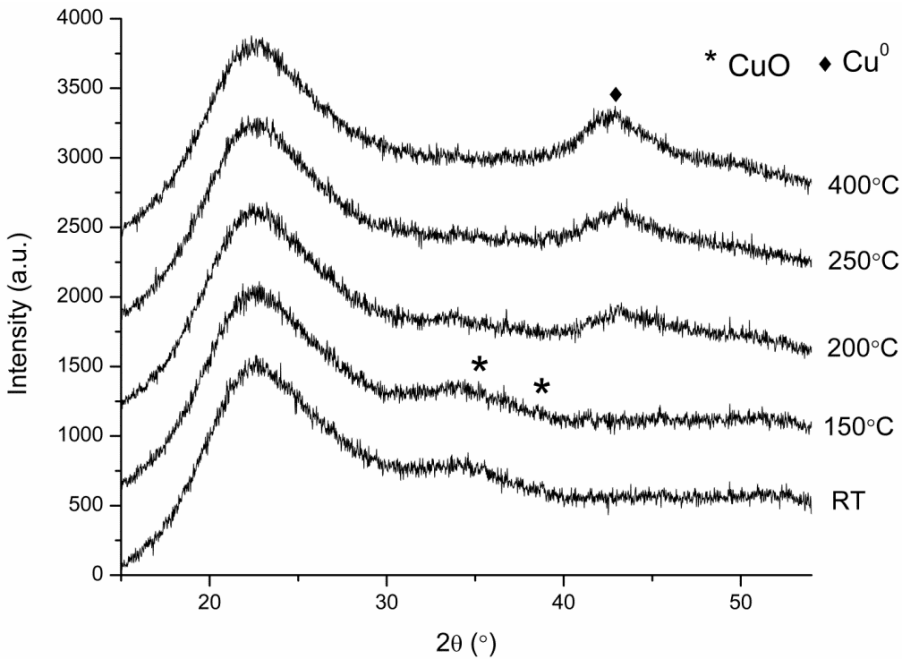

Figure 5.3. Selected XRD patterns during reduction of $CuSn/SiO_2$ in 4% H_2/He at different temperatures.

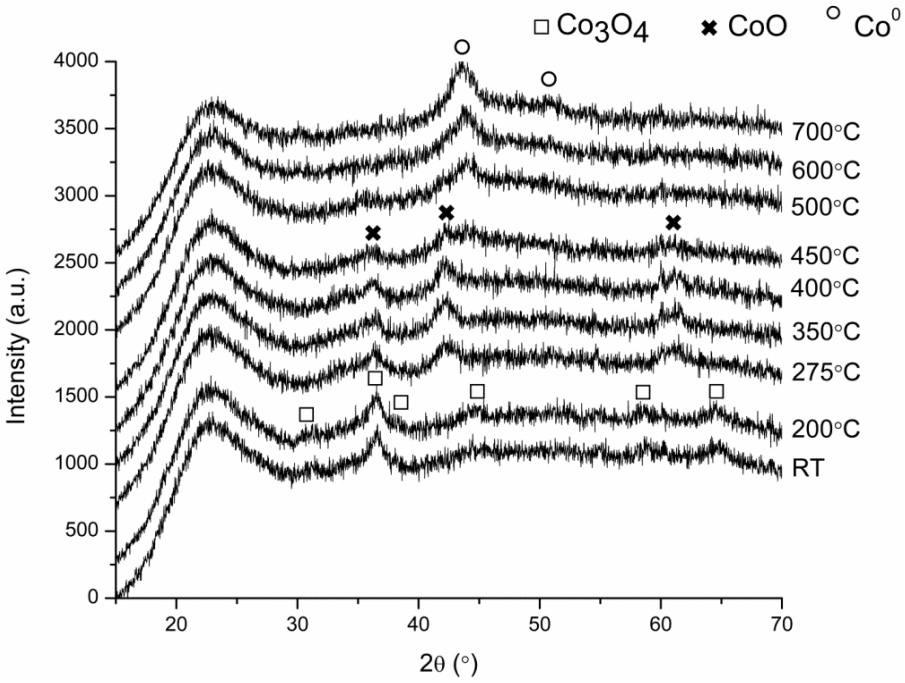

Figure 5.4. Selected XRD patterns during reduction of $CoSn/SiO_2$ in 4% H_2/He at different temperatures.

Figure 5.5 shows that CuO and Co_3O_4 are initially present in $CuCoSn/SiO_2$. As the temperature increases, Cu^0 appears at 200°C, while some Co_3O_4 and Sn-containing phase(s) remain. These are largely reduced by 250°C, beyond which only Cu^0 and Co^0 are visible by XRD.

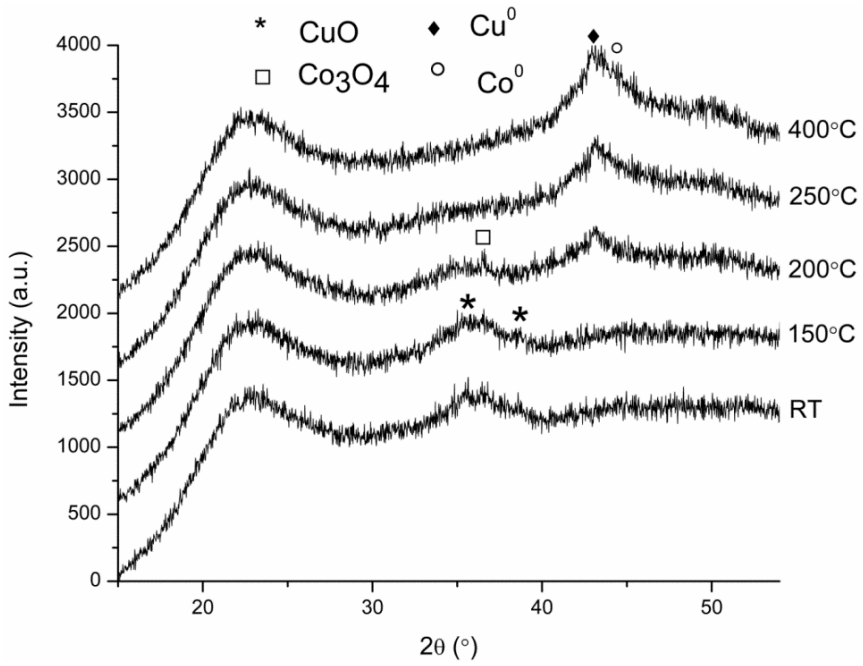

Figure 5.5. Selected XRD patterns during reduction of $CuCoSn/SiO_2$ in 4% H_2/He at different temperatures.

5.3.5. *In situ* DRIFTS

5.3.5.1. $CuSn/SiO_2$

Figure 5.6 presents DRIFTS results during CO hydrogenation at 1 atm on $CuSn/SiO_2$. In general, three distinct peaks can be recognized near 2140 cm^{-1}, 2130 cm^{-1}, and 2110 cm^{-1}. They will be referenced as peaks A, B, and C, respectively.

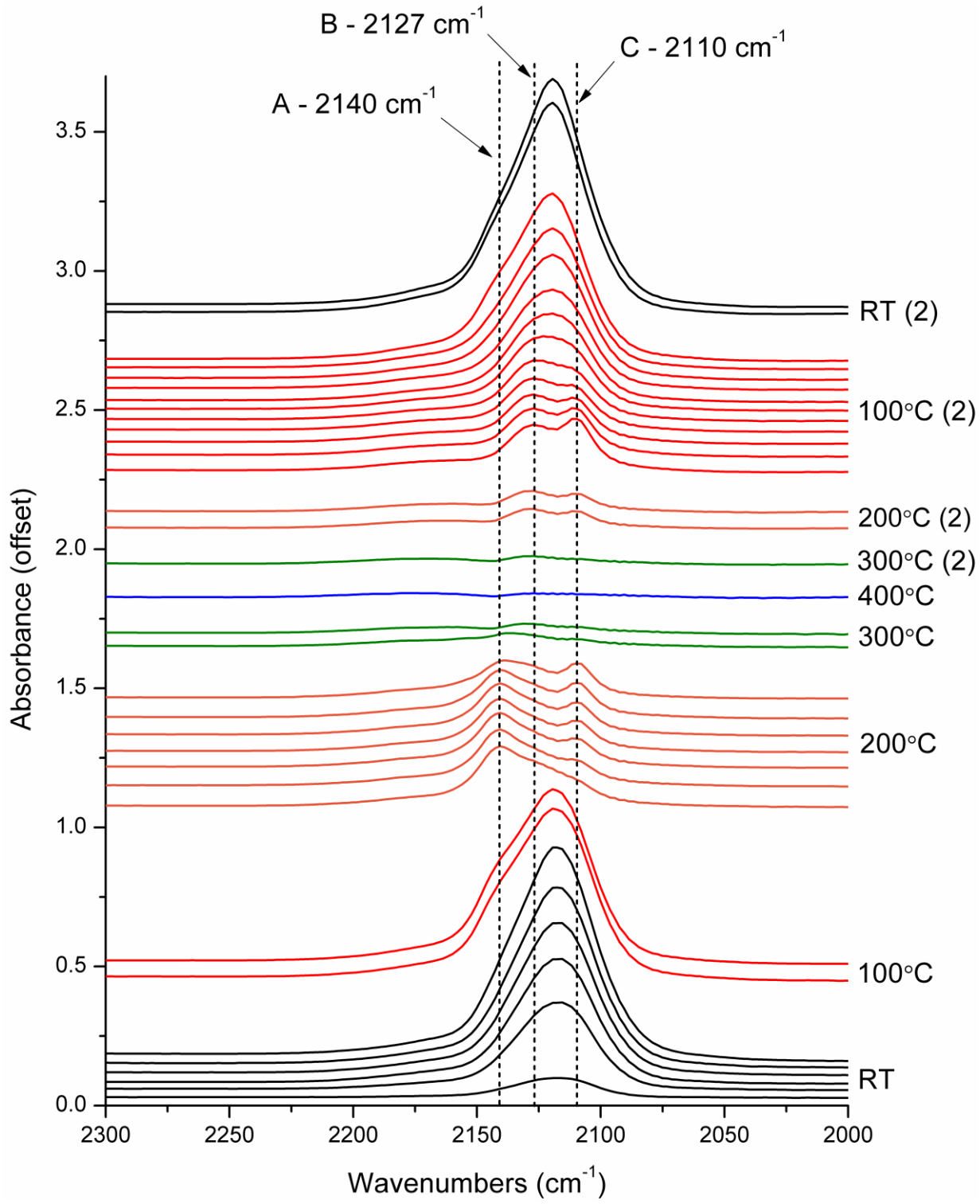

Figure 5.6. Selected DRIFTS spectra of $CuSn/SiO_2$ under $H_2/CO/He$ flow at 1 atm and the temperatures indicated at the right. The order of collection was from bottom to top. Spectra labeled as (2) were collected during cooling to room temperature.

As CO and H_2 are introduced at room temperature, a broad band develops at around 2120 cm^{-1} and encompasses the entire region occupied by peaks A, B, and C. At 100°C, a shoulder develops at the position of peak A. At 200°C, the intensity of all the peaks decreases, but peak A is the most prominent. With time, the initial peak at position A decreases in intensity, while the low-frequency tail strengthens at position C, and between them a hump develops at position B. Figure 5.7 shows the phenomena occurring at 200°C in greater detail. At 300°C, the main component remaining is peak B, though its intensity is low; the shoulder at position C is very weak. At 400°C, all peaks are removed.

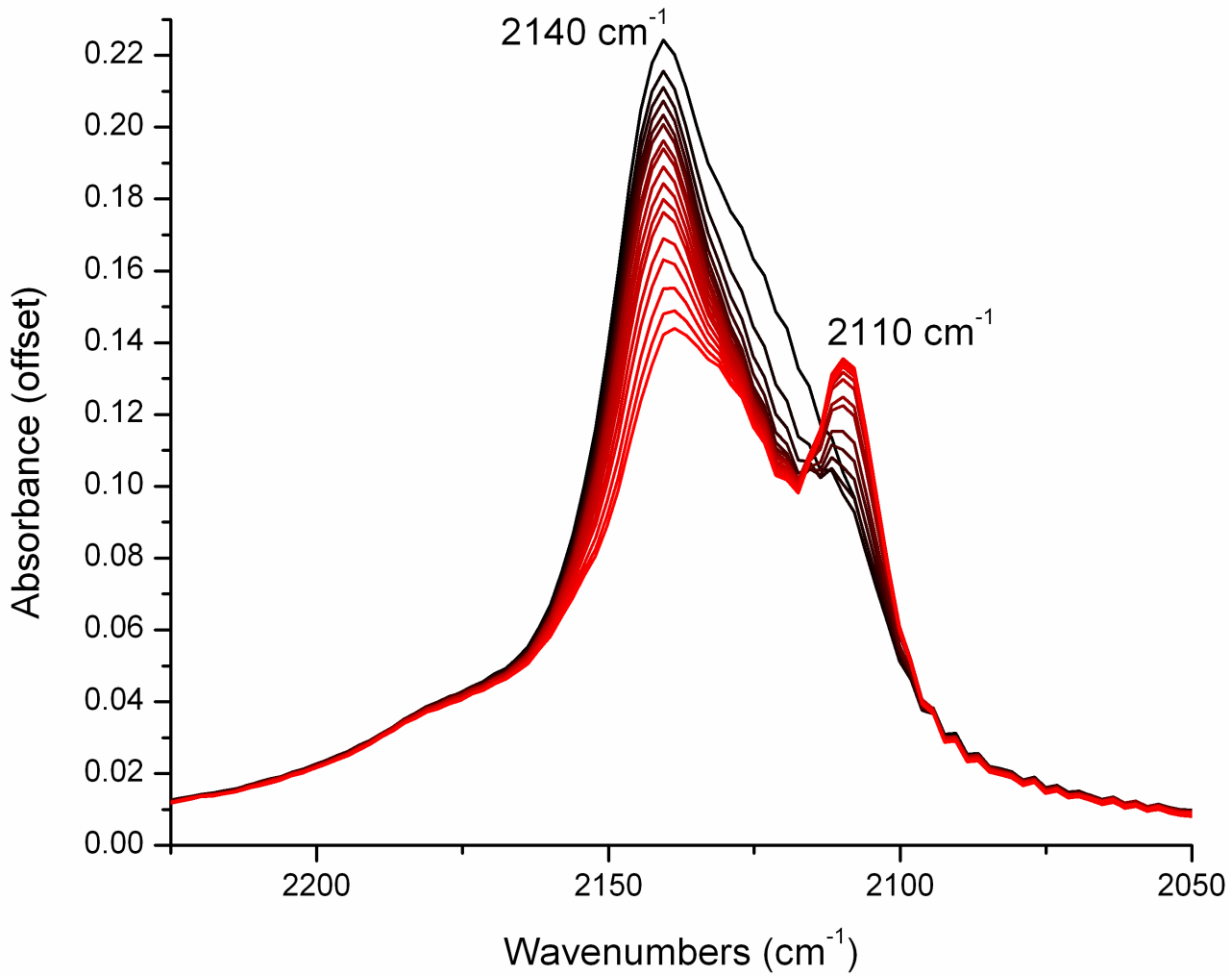

Figure 5.7. DRIFTS spectra of $CuSn/SiO_2$ during CO hydrogenation at 1 atm and 200°C. Spectra are shown in chronological order as black transforming to red.

On the same sample, the above temperatures were repeated in decreasing order to investigate the reversibility of the observed phenomena. At 300°C, peak B reappears, but at even lower intensity. At 200°C, only peaks B and C are observed. At 100°C, peak C decreases in intensity while that of peak B increases. With time, peaks B and C merge and grow; ultimately, a shoulder also appears at position A. At room temperature, a broad, intense band at 2120 cm^{-1}, similar to the one seen previously at room temperature, is observed.

Spectra during CO adsorption/desorption are shown in Figure 5.8. CO adsorption at room temperature produces a peak at position B, which shifts to 2122 cm^{-1} with increasing

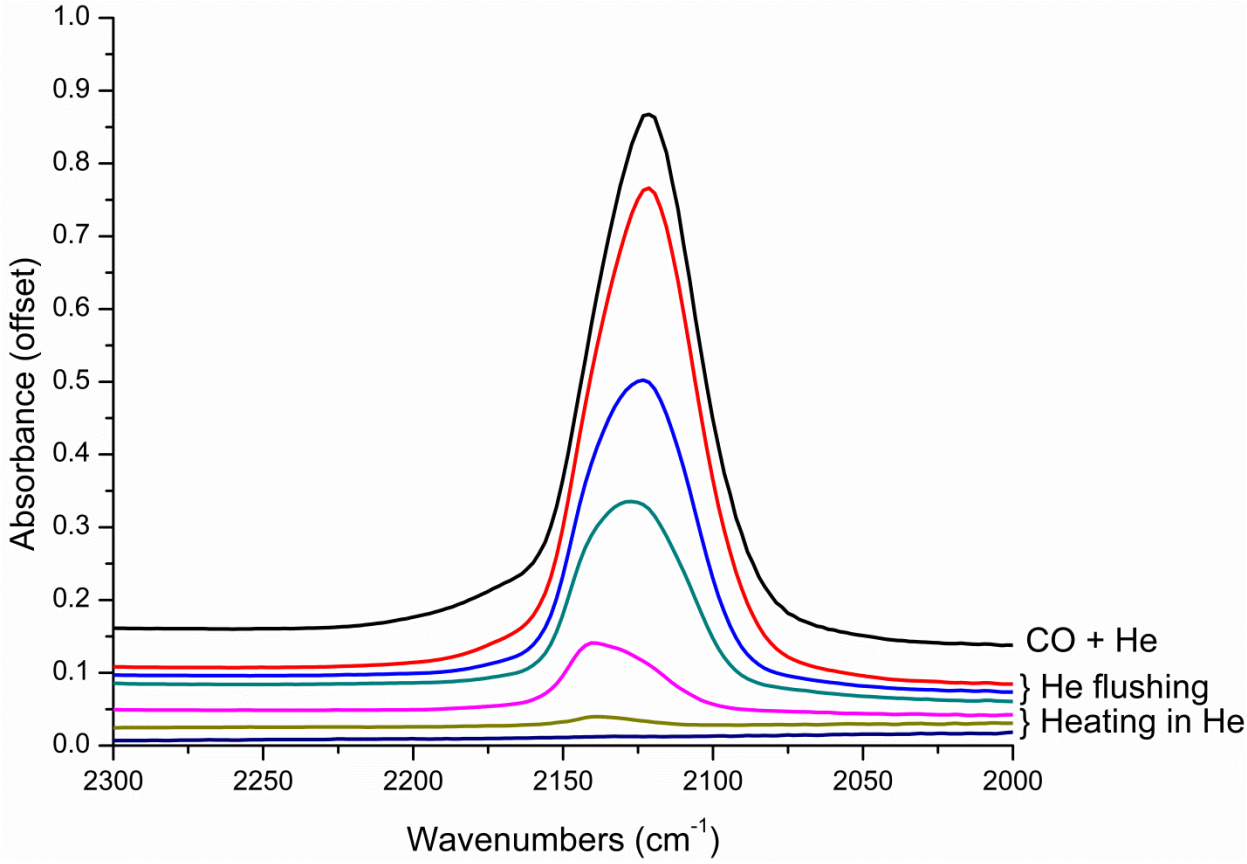

Figure 5.8. DRIFTS spectra during CO adsorption at room temperature on $CuSn/SiO_2$, followed by room temperature He flushing and heating in He to 100°C, 200°C, and 300°C (three bottom spectra). Spectra are in chronological order from top to bottom.

exposure time. He flushing decreases the intensity of this peak and returns its center to position B. Upon heating to 100°C and 200°C, the peak intensity progressively reduces, but the main component in both cases is at A, with a shoulder or tail through B. At 300°C, barely any adsorbed CO remains on the surface, except for a very small amount at position B.

Comparing the different sets of spectra in Figures 5.6-5.8 shows that:

(1) The species responsible for peak A, if already adsorbed at lower temperature, survives up to 200°C both in H_2/CO/He atmosphere and under He desorbing conditions. However, species A does not adsorb at 200°C during the cooling segment of the CO hydrogenation experiment (Figure 5.6).

(2) The decreasing intensity of peak A at 200°C in Figure 5.7, accompanied by an increase in the intensity of peak C, might suggest that "A" species are transforming to "C" species. For example, peak A could arise from multiply populated sites and peak C from the same type of site with only one CO adsorbed. In this view, the opposing trends in intensity result from desorption of some of the "extra" CO ligands (species A), leaving behind single CO molecules (species C). However, in the CO adsorption/desorption experiment, only "A" and "B" species remain at 200°C, and show uniformly decreasing intensity with no peak appearing at C.

(3) Species C is the most easily desorbed in the absence of CO flow; there is no infrared absorption at this position at temperatures > 100°C. In the presence of H_2/CO, however, a small amount of species C is present up to 300°C, and peak A is the first to disappear. On CuSn/SiO_2, species C is stabilized by the presence of CO.

Next, we consider possible assignments for each peak according to the literature.

Peak A (2140 cm^{-1}):

Peaks in the vicinity of 2140 cm^{-1} are sometimes attributed to CO adsorbed on Cu^{2+} ions [30], but usually this species absorbs at wavenumbers higher than about 2150 cm^{-1} [31-34]. CO is also reported to be weakly bound on Cu^{2+} and to desorb into flowing inert at 27°C [35]. Because peak A is the main component during desorption in He at 100°C in the present work, CO on Cu^{2+} can be ruled out as the origin of this peak. Furthermore, reduction at 400°C should suffice to reduce Cu^{2+} entirely to Cu^0 (this is confirmed by TPR, which shows a maximum at about 190°C, and by *in-situ* XRD).

On the other hand, de Jong et al. [36] proposed that a peak at 2139 cm^{-1} might be due to CO adsorbed on small metallic particles of high curvature that expose a large number of protruding atoms or small clusters. This assignment for peak A would be consistent with *in-situ* XRD, which shows very broad, weakly crystalline peaks for Cu^0 in $CuSn/SiO_2$ after reduction at 400°C. Furthermore, peak A is absent from DRIFTS spectra after CO adsorption on a highly crystalline, Sn-free Cu/SiO_2 catalyst.

The latter point also suggests a possible alternative explanation for the peak at position A—that it could be due to CO adsorption on a copper species interacting with tin. For example, the DFT study of Gokhale et al.[21] showed that a copper terminated CuSn alloy adsorbed CO with a higher binding energy than did Cu(111). They ascribed the strengthening of the CO adsorption bond to increased electron donation from CO to the copper surface due to surface strain from tin alloying. An increase in electron donation to the surface would be expected to shift the absorption toward higher frequencies, consistent with the position of peak A. Thus, peak A could plausibly be due to CO adsorbed on copper sites at the surface of a copper-tin alloy.

Peak B (2130 cm^{-1}):

Peaks near 2130 cm^{-1} are usually assigned to CO linearly adsorbed on Cu^{+} ions when the species is stable to evacuation, flushing, or heating [32,34,35,37,38]. Again, all copper is expected to be metallic after reduction at 400°C, so CO adsorbed on bulk Cu_2O is unlikely to be responsible for this peak. It is plausible, however, that peak B results from CO adsorption on copper having a slight positive charge due to interaction with oxygen atoms or hydroxyl groups at the support interface [39,40].

On Sn-free Cu/SiO_2 and $CuCo/SiO_2$, peak B is the only absorption resulting from CO adsorption on copper; peaks A and C are not observed [41]. On these catalysts, the peak vanishes near 200°C under both adsorption/desorption and CO hydrogenation conditions.

On all these catalysts, a band at about 1630 cm^{-1}, corresponding to the bending vibration of molecular water [42,43], is consistently detected upon CO admission at room temperature. The disruption of surface OH groups by adsorbing CO, forming some molecular water and locally oxidized surface sites, could account for the position of peak B. This process would be roughly analogous to the "CO-induced oxidative disruption" observed on ruthenium catalysts [44]. Therefore, we assign peak B to CO adsorbed on copper interacting with hydroxyl groups or at the support interface.

Peak C (2110 cm^{-1}):

Bands in the range 2100-2110 cm^{-1} are typical of CO adsorption on well-reduced copper catalysts [30,45], particularly ones with extended stepped surfaces [36,39]. It is therefore conceivable that peak C might arise from CO adsorbed on high-index Cu^{0} planes. On the other hand, peak C might be due to an alternate type of Cu-Sn interaction—for example, copper particles decorated (but not covered) by Sn species.

Assuming peaks A and C are due to the two above-mentioned types of copper-tin interactions, the results of Figures 5.6-5.8 may be interpreted as follows. At room temperature, in CO/He or H_2/CO/He, all three types of sites (depicted schematically in Figure 5.9) are present and occupied. Under H_2/CO/He during heating at 200°C, tin begins to segregate to the surface of a copper-tin alloy, resulting in a transfer of intensity from peak A (due to the alloy) to peak C (due to Sn-decorated copper). The reason no such transfer is observed in the case of He desorption at 200°C (Figure 5.8) could be that CO has already desorbed from the copper sites in question and no gas phase CO is available to repopulate them. The initial decrease in peak C during cooling at 100°C (Figure 5.6) could be due to the loss of some of these sites as Sn atoms migrate back to their original, subsurface locations. Consistent with this view, peak A is the last to appear during this step. The driving force for the reconstruction would be the stabilization of CO on the surface. Though we have no direct evidence for the postulated reconstruction, it would provide a consistent, unified explanation for the data in this study.

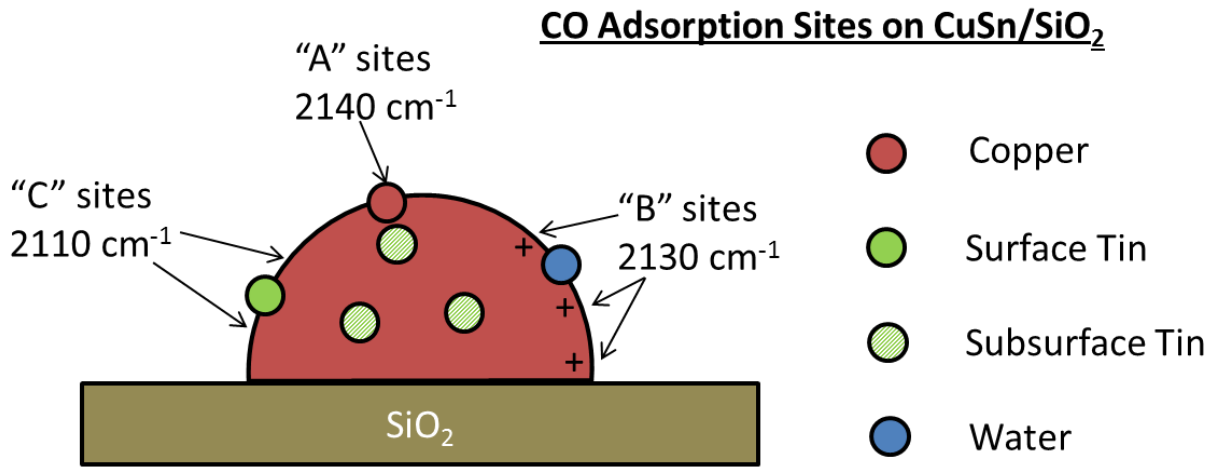

Figure 5.9. Postulated sites to account for peaks at 2140 cm^{-1}, 2130 cm^{-1}, and 2110 cm^{-1} during CO adsorption/desorption and CO/H_2/He flow on CuSn/SiO_2.

5.3.5.2. $CuCoSn/SiO_2$

Figure 5.10 shows selected DRIFTS spectra during CO hydrogenation on $CuCoSn/SiO_2$ at atmospheric pressure. The spectra at room temperature and 100°C are similar to the ones on $CuSn/SiO_2$ at the same temperatures. There is no maximum from CO adsorbed on cobalt at the first two temperatures. At 200°C, CO mainly occupies "A" sites on copper, in keeping with the nomenclature used for the peaks on $CuSn/SiO_2$. At 300°C, the copper peak shifts from position A to position B. At 400°C, the CO-copper peak disappears, returning upon cooling again to 300°C. This peak at B is difficult to remove by hydrogenation when CO flow is stopped.

Figure 5.11 shows results of CO adsorption/desorption on $CuCoSn/SiO_2$. In CO flow and during He flushing at room temperature, a broad peak spans regions A, B, and C. In flowing He at 100°C, peak A dominates, with a tail through B and a shoulder at C. Peak A again dominates at 200°C. At 300°C, there is a very slight peak at B.

The main difference in the DRIFTS spectra between $CuSn/SiO_2$ and $CuCoSn/SiO_2$, so far as CO adsorption on copper is concerned, is that the growth of peak C at the expense of peak A (Figure 5.7, CO hydrogenation) does not occur on $CuCoSn/SiO_2$. The stabilization of species C under H_2/CO/He flow is not favored when cobalt is present. It could be that Sn^0 helps to stabilize this species, but the close interaction between Co^0 and Sn^0 interferes with this effect on $CuCoSn/SiO_2$.

Only peaks corresponding to CO adsorbed on copper, but none in the region of CO on cobalt, are observed after the initial CO exposure at room temperature in either Figure 5.10 (hydrogenation) or Figure 5.11 (adsorption/desorption). Upon continuation of CO hydrogenation

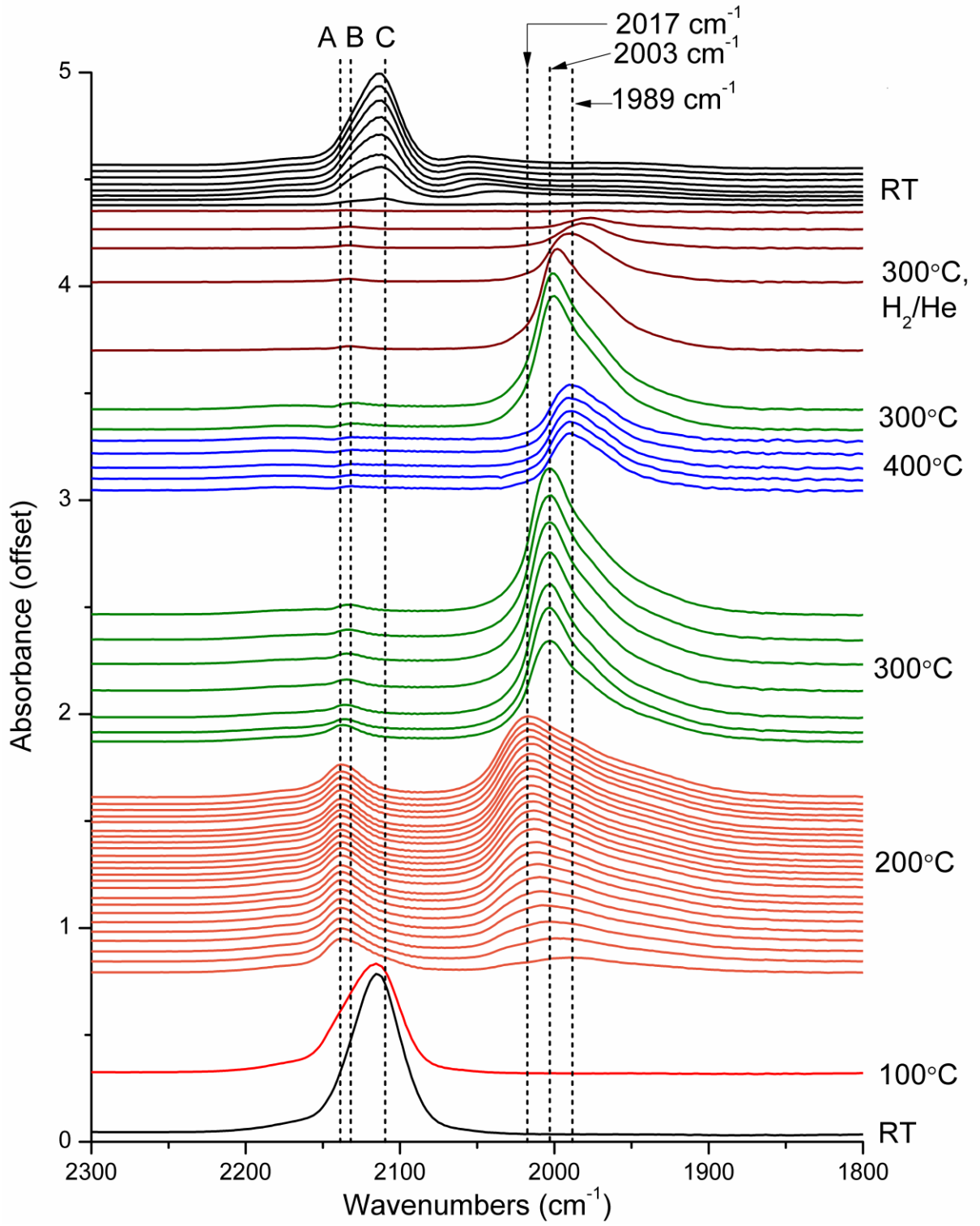

Figure 5.10. Selected DRIFTS spectra of $CuCoSn/SiO_2$ under $H_2/CO/He$ flow (except where H_2/He flow is noted) at 1 atm and the temperatures indicated at the right. The order of collection was from bottom to top.

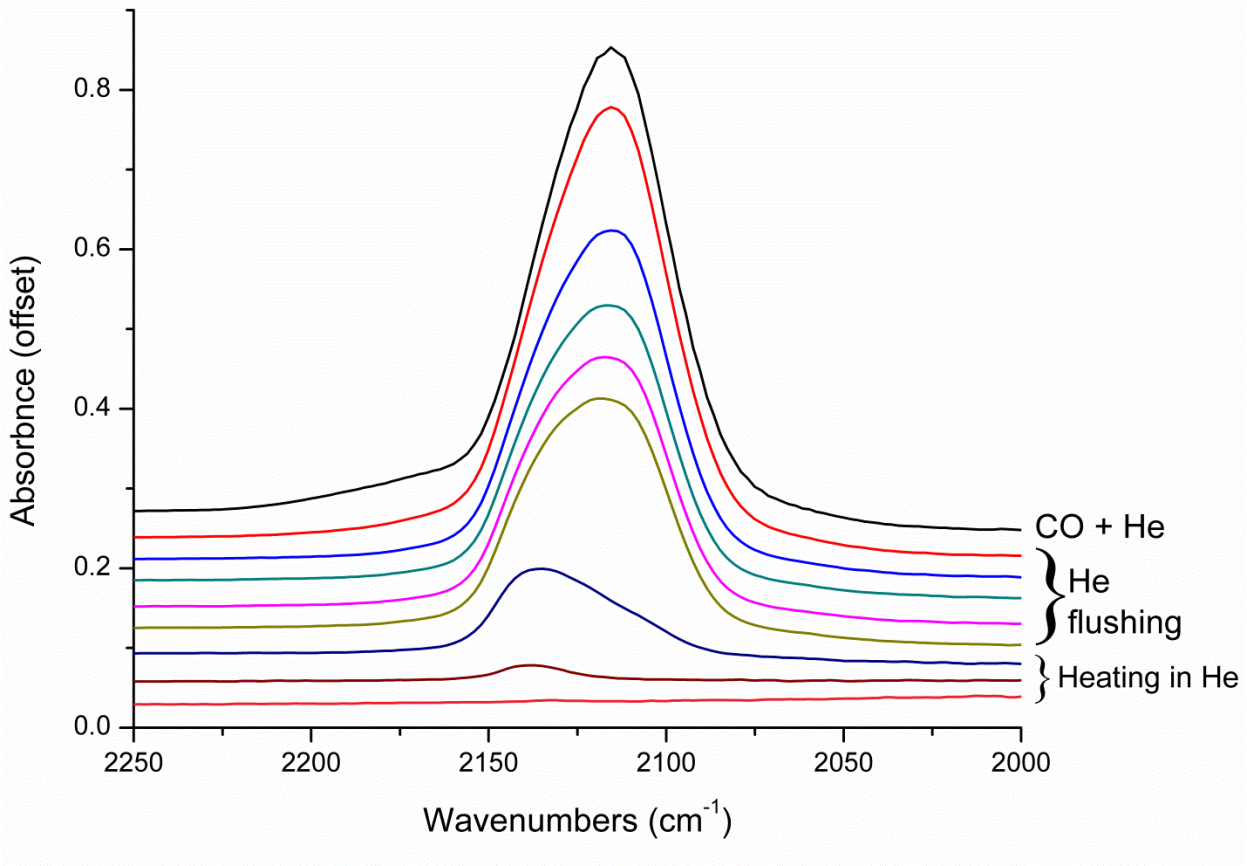

Figure 5.11. DRIFTS spectra during CO adsorption at room temperature on $CuCoSn/SiO_2$, followed by room temperature He flushing and heating in He to 100°C, 200°C, and 300°C. Spectra are in chronological order from top to bottom.

(Figure 5.10), peaks for CO adsorbed on cobalt emerge at 200°C. Initially, a peak at 1985 cm^{-1} is flanked by a shoulder at 2015-2020 cm^{-1}. With increasing coverage, the main peak shifts from 1985 cm^{-1} to 2017 cm^{-1}, obscuring the shoulder, and a tail develops on the low frequency side. At 300°C, the most intense absorption shifts to 2003 cm^{-1}, and a shoulder becomes visible at about 1985 cm^{-1}. At 400°C, the CO-cobalt band is reduced to a single component at 1989 cm^{-1}. Upon returning to 300°C, the peak near 2000 cm^{-1} and shoulder at 1985 cm^{-1} are restored. CO flow is then removed and the experiment continued at 300°C under H_2/He. Within a few

minutes, the peak near 2000 cm^{-1} disappears, but the low frequency component resists hydrogenation; traces of this peak are still observed after more than three hours.

When the sample is returned to room temperature, and CO is again introduced, the first adsorption occurs on copper at position C, with a shoulder at B. With time, a broad adsorption band develops, spanning regions A, B, and C. This time, a CO-cobalt peak is also observed, shifting from about 2030 cm^{-1} to 2055 cm^{-1} with time.

The main CO-cobalt peak appears in a frequency range (about 2000 cm^{-1} to 2055 cm^{-1}, depending on the coverage and temperature) characteristic of CO linearly adsorbed on Co^0 sites [46-52]. The shift to higher frequency with increasing peak intensity at 200°C is also expected of this species, due to electron-withdrawing effects from the increasing adsorbate population. This suggests that the Co^0 particles, though well dispersed, are not so small as to prohibit adsorption of CO molecules on adjacent metallic cobalt sites.

CO hydrogenation on $CuCo/SiO_2$ also gives a peak in the frequency window for linearly adsorbed CO on Co^0 [41], but at consistently higher frequency than the peak from $CuCoSn/SiO_2$. This suggests that CO binding to Co^0 is stronger on the Sn-containing catalyst.

With increasing temperature, the amount of CO adsorbed (judged by the peak area), first increases from zero at room temperature and 100°C, to a pronounced peak at 200°C and a maximum at 300°C before decreasing at 400°C. The temperature dependence of the quantity of CO adsorbed suggests that chemisorption is activated on the Co^0 surface.

Increasing the temperature from 200°C to 300°C shifts the peak to lower frequency, despite the increasing intensity, which would tend to shift the maximum in the opposite direction. This can be explained on the basis of two competing phenomena, one kinetic and one

thermodynamic. Increasing temperature activates CO chemisorption but also destabilizes CO on sites where binding is weaker.

A peak due to linearly adsorbed CO appears during the final exposure to H_2/CO/He at room temperature, whereas none exists during the initial exposure at room temperature. This suggests that the intervening treatments lower the activation barrier for CO adsorption on Co^0, or create new adsorption sites.

The secondary peak or shoulder at 1985-1990 cm^{-1} is especially stable. It remains after increasing the temperature to 400°C and resists hydrogenation when CO is removed from the gas phase at 300°C. By analogy to results on RuSn and PdSn catalysts [6,20], this low-frequency peak could arise from linear CO on Co^0 electronically enriched by interaction with tin.

5.3.5.3. $CoSn/SiO_2$

After reduction of $CoSn/SiO_2$ at 400°C, the DRIFTS spectra during CO hydrogenation contain no clear peaks at any temperature. To test whether the absence of Co^0 is responsible for the lack of adsorption, CO hydrogenation was performed again after reduction at 500°C (spectra shown in Figure 5.12). The only peak observed has weak intensity and is seen after the sample has been exposed to syngas at high temperature and cooled again to room temperature. Flushing away the gas phase CO reveals the peak at 2080 cm^{-1}, a position characteristic of linear CO on $Co^{\delta+}$ sites. This species usually absorbs at frequencies at or above 2050 cm^{-1} [46,53-57].

5.3.5.4. Comparison of CO Adsorption on Sn-promoted and Unpromoted Catalysts

The infrared absorption intensity is much higher on Sn-promoted Cu/SiO_2 and $CuCo/SiO_2$ than on the Sn-free catalysts submitted to similar experiments. This is true of the CO

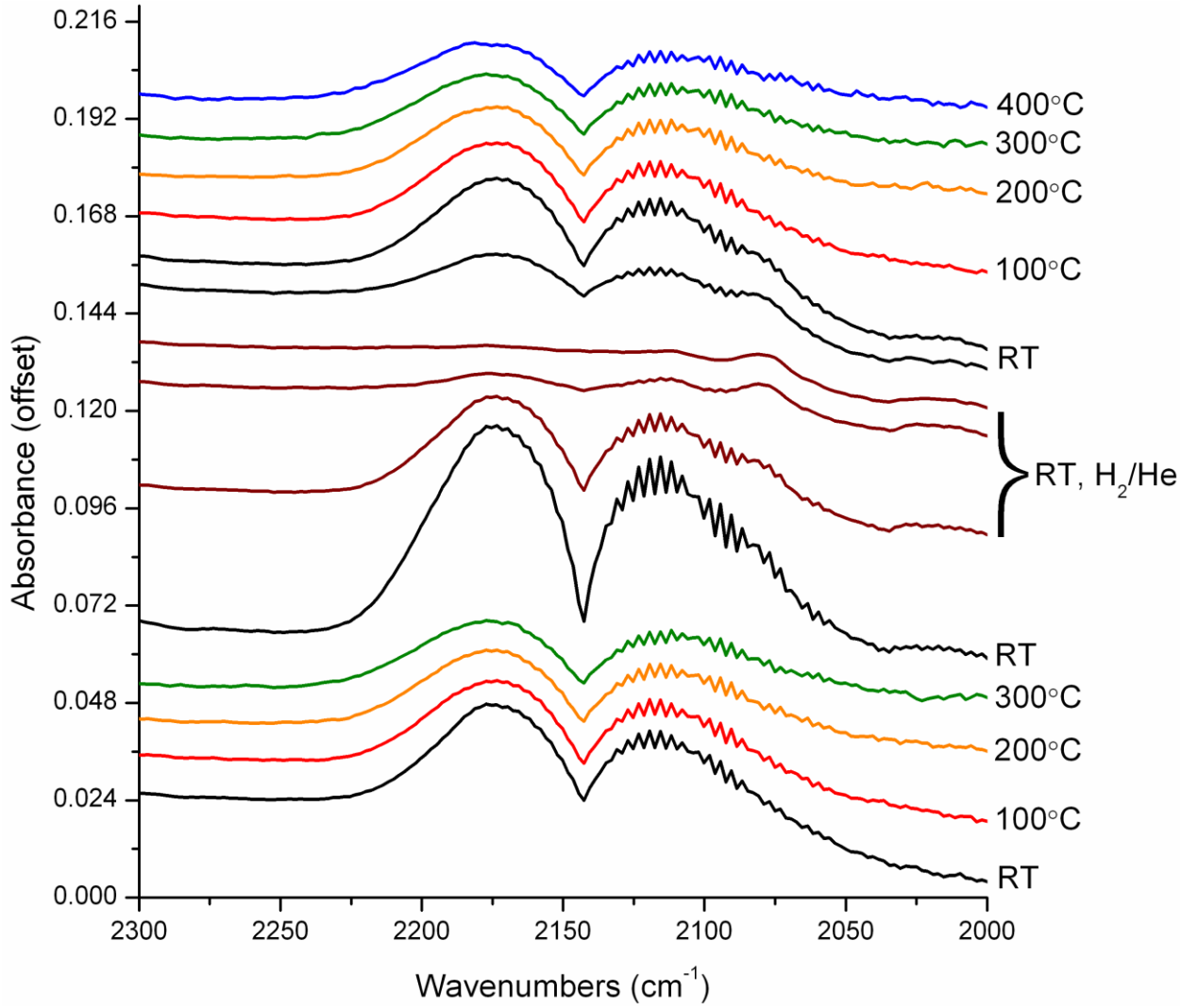

Figure 5.12. Selected DRIFTS spectra of $CoSn/SiO_2$ under H_2/CO flow at 1 atm and the temperatures indicated at the right. The order of collection was from bottom to top. The catalyst was reduced at 500°C prior to the experiment.

adsorbed on both copper and cobalt sites (as shown in Figure 5.13, which compares CO hydrogenation on $CuCo/SiO_2$ and $CuCoSn/SiO_2$ at room temperature and 300°C). The increase in CO adsorption capacity would be expected based on the increase in dispersion induced by Sn. By contrast, Sn addition does not increase the intensity of the CO peak on $CoSn/SiO_2$, because of the difficulty of cobalt reduction.

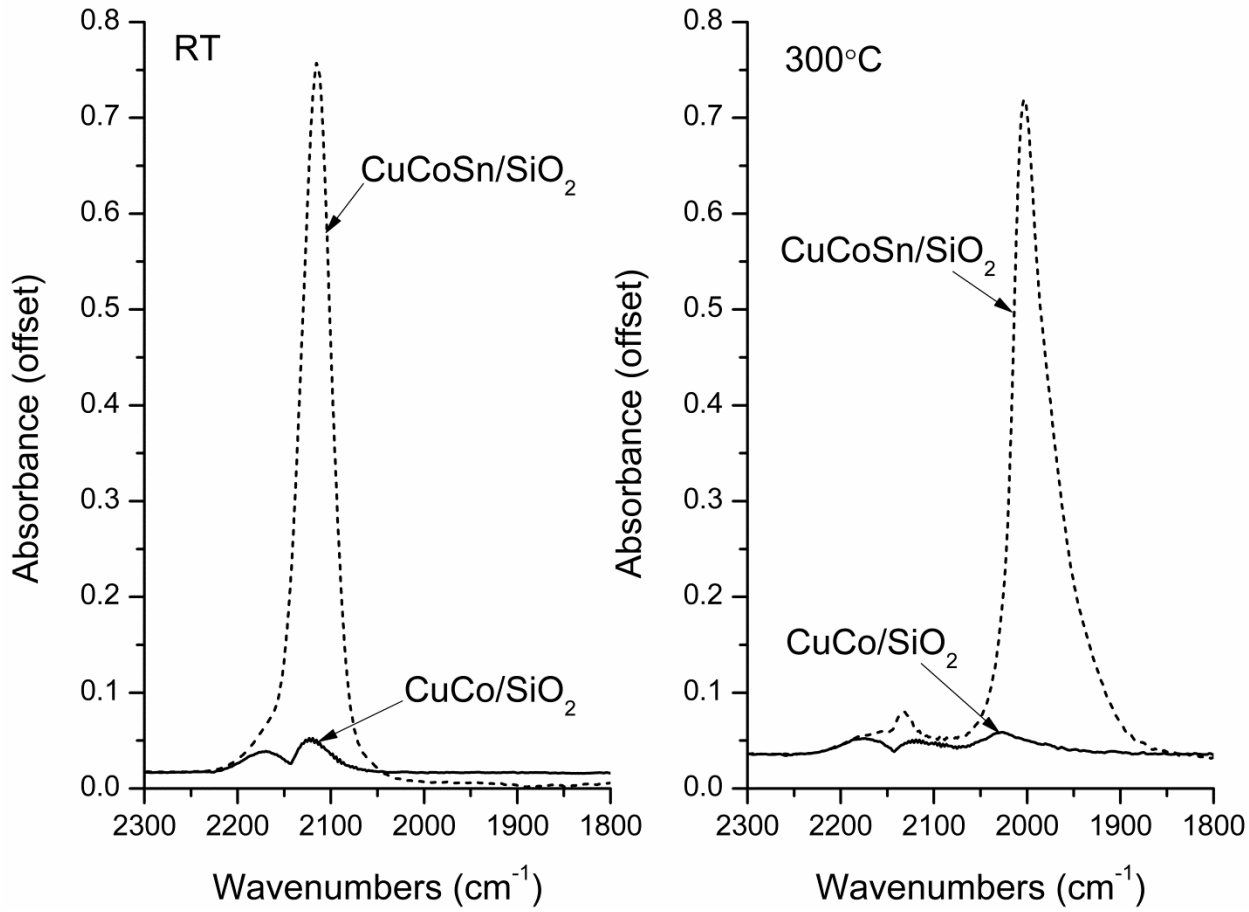

Figure 5.13. DRIFTS spectra on $CuCo/SiO_2$ and $CuCoSn/SiO_2$ under H_2/CO/He flow at room temperature and 300°C.

5.3.6. Catalytic Reaction

The results of CO hydrogenation on tin-promoted and unpromoted catalysts are shown in Table 5.3. $CoSn/SiO_2$ (not shown) is almost completely inactive. This is unsurprising, since reduction at 400°C fails to produce any metallic cobalt. $CuSn/SiO_2$ also gives a very low conversion. It has much higher CO_2 selectivity than any of the other catalysts, consistent with reports that Sn can increase water-gas shift activity when added to Group IB metal catalysts [21,58]. This may be related to species C, located at 2110 cm^{-1} in the DRIFTS spectrum. The thermal

stabilization of this species is a phenomenon peculiar to this catalyst. Other than CO_2, $CuSn/SiO_2$ produces only methanol, methane, and trace amounts of ethane. The chain growth selectivity of this catalyst is not significant.

Table 5.3. Carbon selectivities (%) and CO conversions (%) from GC-FID analysis of reaction products[a].

	CO_2	MeOH	EtOH	C_{2+} Oxygenates	CH_4	C_{2+} Hydrocarbons	CO Conversion
Cu/SiO_2	3.6	14.5	6.9	0.2	46.6	28.2	0.12
Co/SiO_2	1.9	2.6	1.2	0.8	59.1	34.4	12.2
$CuCo/SiO_2$	2.8	5.2	3.3	1.7	53.5	33.5	0.88
$CuSn/SiO_2$	43.7	17.2	0	0	32.4	6.7	0.02
$CuCoSn/SiO_2$	2.9	11.6	6.5	0	58.6	20.4	0.10

[a]Reaction conditions: P = 10 bar, T = 300°C, $H_2/CO = 2$, GHSV = 24,000 $scc/g_{cat}/h$. C_{2+} oxygenates analyzed include acetaldehyde, acetone, i-propanol, n-propanol, i-butanol, and n-butanol. C_{2+} hydrocarbons include ethane, propane, propylene, i-butane, n-butane, and n-hexane.

Compared to its Sn-free counterpart at 300°C, $CuCoSn/SiO_2$ gives higher ethanol selectivity but considerably lower conversion. The performance of $CuCoSn/SiO_2$ closely resembles that of Cu/SiO_2, albeit with higher methane selectivity and lower C_{2+} hydrocarbon selectivity. Nevertheless, the cobalt sites of $CuCoSn/SiO_2$ are needed for ethanol formation, since $CuSn/SiO_2$ fails to produce any ethanol even though well reduced. The methane selectivity of $CuCoSn/SiO_2$ is closest to that of Co/SiO_2. $CuCoSn/SiO_2$ does not favor the formation of C_{2+} oxygenates other than ethanol. The selectivity results (increased methane, methanol, and ethanol; decreased C_{2+} hydrocarbons and zero C_{2+} oxygenates) suggest that the addition of Sn strongly inhibits chain growth on cobalt sites. On this catalyst, the large amount of associatively

adsorbed CO might dilute surface dissociated CO, thereby preventing coupling of CH_x species. CO insertion into such CH_x species, on the other hand, is more probable on the Sn-promoted catalyst.

Highly dispersed, metallic cobalt has previously been found to favor oxygenate selectivity while decreasing catalyst activity [59]. In $CuCoSn/SiO_2$, cobalt is present in such a state and also adsorbs more CO in associative form than does Sn-free $CuCo/SiO_2$. Because CO is adsorbed in large quantities, the low activity of $CuCoSn/SiO_2$ must be related to a reduced capability for H_2 adsorption, dissociation, or reaction with surface intermediates.

5.4. Conclusions

When added to silica-supported copper, cobalt, and copper-cobalt catalysts, tin acted mainly as a dispersing agent. Tin increased the reducibility of copper oxides and decreased that of cobalt oxides. In $CuCoSn/SiO_2$, copper acted as a reduction promoter of cobalt. Due to the combined effects of tin and copper, highly dispersed, well-reduced metallic particles were produced on $CuCoSn/SiO_2$ upon activation.

As a corollary to the increase in dispersion, tin addition greatly increased the amount of CO adsorbed on the copper sites of $CuSn/SiO_2$ and on both copper and cobalt sites of $CuCoSn/SiO_2$. The addition of tin also resulted in new types of adsorbed CO, not observed on the tin-free catalysts. Furthermore, the stability of CO on the surface increased.

For CO hydrogenation, the addition of tin depressed the overall catalytic activity. Sn also inhibited the Fischer-Tropsch chain growth ability of the reduced cobalt sites of $CuCoSn/SiO_2$ by diluting CH_x species with associatively adsorbed CO. This resulted in reduced selectivity to higher hydrocarbons compared to $CuCo/SiO_2$. However, CO insertion became more likely, which favored ethanol selectivity.

5.5. References

1. Riguetto, B. A.; Rodrigues, C. E. C.; Morales, M. A.; Baggio-Saitovitch, E.; Gengembre, L.; Payen, E.; Marques, C. M. P.; Bueno, J. M. C. *Appl. Catal., A* **2007**, *318*, 70.

2. Margitfalvi, J. L.; Tompos, A.; Kolosova, I.; Valyon, J. *J. Catal.* **1998**, *174*, 246.

3. Margitfalvi, J. L.; Vankó, G.; Borbáth, I.; Tompos, A.; Vértes, A. *J. Catal.* **2000**, *190*, 474.

4. Pouilloux, Y.; Autin, F.; Guimon, C.; Barrault, J. *J. Catal.* **1998**, *176*, 215.

5. Ferretti, O. A.; Bournonville, J. P.; Mabilon, G.; Martino, G.; Candy, J. P.; Basset, J. M. *J. Mol. Catal.* **1991**, *67*, 283.

6. Vicente, A.; Lafaye, G.; Especel, C.; Marecot, P.; Williams, C. T. *J. Catal.* **2011**, *283*, 133.

7. Liberkova, K.; Touroude, R. *J. Mol. Catal. A: Chem.* **2002**, *180*, 221.

8. Courty, P.; Durand, D.; Freund, E.; Sugier, A. *J. Mol. Catal.* **1982**, *17*, 241.

9. Sheffer, G. R.; King, T. S. *Appl. Catal.* **1988**, *44*, 153.

10. Chu, W.; Kieffer, R.; Kiennemann, A.; Hindermann, J. P. *Appl. Catal., A* **1995**, *121*, 95.

11. Tien-Thao, N.; Alamdari, H.; Zahedi-Niaki, M. H.; Kaliaguine, S. *Appl. Catal., A* **2006**, *311*, 204.

12. Tien-Thao, N.; Zahedi-Niaki, M. H.; Alamdari, H.; Kaliaguine, S. *Appl. Catal., A* **2007**, *326*, 152.

13. Shi, L. M.; Chu, W.; Deng, S. Y.; Xu, H. Y. *J. Nat. Gas Chem.* **2008**, *17*, 397.

14. Deng, S. Y.; Chu, W.; Xu, H. Y.; Shi, L. M.; Huang, L. H. *J. Nat. Gas Chem.* **2008**, *17*, 369.

15. Dong, X.; Liang, X. L.; Li, H. Y.; Lin, G. D.; Zhang, P.; Zhang, H. B. *Catal. Today* **2009**, *147*, 158.

16. Subramanian, N. D.; Balaji, G.; Kumar, C. S. S. R.; Spivey, J. J. *Catal. Today* **2009**, *147*, 100.

17. Fang, Y. Z.; Liu, Y.; Zhang, L. H. *Appl. Catal., A* **2011**, *397*, 183.

18. Kiennemann, A.; Diagne, C.; Hindermann, J. P.; Chaumette, P.; Courty, P. *Appl. Catal.* **1989**, *53*, 197.

19. Xiaoding, X.; Doesburg, E. B. M.; Scholten, J. J. F. *Catal. Today* **1987**, *2*, 125.

20. Riguetto, B. A.; Bueno, J. M. C.; Petrov, L.; Marques, C. M. P. *Spectrochim. Acta A* **2003**, *59*, 2141.

21. Gokhale, A. A.; Huber, G. W.; Dumesic, J. A.; Mavrikakis, M. *J. Phys. Chem. B* **2004**, *108*, 14062.

22. Smith, M. L.; Campos, A.; Spivey, J. J. *Catal. Today* **2012**, *182*, 60.

23. Williams, G. P. In *X-Ray Data Booklet*; second ed.; Thompson, A. C., Vaughan, D., Eds.; Lawrence Berkeley National Laboratory: Berkeley, 2001, p 1.

24. Ravel, B.; Newville, M. *J. Synchrotron Radiat.* **2005**, *12*, 537.

25. Nava, N.; Viveros, T. *J. Radioanal. Nucl. Chem.* **2000**, *243*, 689.

26. Bennici, S.; Auroux, A.; Guimon, C.; Gervasini, A. *Chem. Mater.* **2006**, *18*, 3641.

27. Depero, L. E.; Levrangi, P.; Sberveglieri, G. *J. Solid State Chem.* **1995**, *116*, 256.

28. Ramaswamy, V.; Shah, P.; Lazar, K.; Ramaswamy, A. V. *Catal. Surv. Asia* **2008**, *12*, 283.

29. Huo, G. Y.; Lu, J.; Ren, L. X. *J. Alloys Compd.* **2004**, *368*, 126.

30. Hollins, P. *Surf. Sci. Rep.* **1992**, *16*, 51.

31. Rodrigues, E. L.; Marchi, A.; Apesteguia, C. R.; Bueno, J. M. C. *Appl. Catal., A* **2005**, *294*, 197.

32. Hadjiivanov, K.; Knozinger, H. *Phys. Chem. Chem. Phys.* **2001**, *3*, 1132.

33. Busca, G. *J. Mol. Catal.* **1987**, *43*, 225.

34. Padley, M. B.; Rochester, C. H.; Hutchings, G. J.; King, F. *J. Catal.* **1994**, *148*, 438.

35. Dandekar, A.; Vannice, M. A. *J. Catal.* **1998**, *178*, 621.

36. de Jong, K. P.; Geus, J. W.; Joziasse, J. *Appl. Surf. Sci.* **1980**, *6*, 273.

37. Hadjiivanov, K.; Tsoncheva, T.; Dimitrov, M.; Minchev, C.; Knozinger, H. *Appl. Catal., A* **2003**, *241*, 331.

38. Tsoncheva, T.; Venkov, T.; Dimitrov, M.; Minchev, C.; Hadjiivanov, K. *J. Mol. Catal. A: Chem.* **2004**, *209*, 125.

39. Boccuzzi, F.; Coluccia, S.; Martra, G.; Ravasio, N. *J. Catal.* **1999**, *184*, 316.

40. Ferullo, R. M.; Castellani, N. J. *J. Mol. Catal. A: Chem.* **2005**, *234*, 121.

41. Smith, M. L.; Kumar, N.; Spivey, J. J. *J. Phys. Chem. C* **2012**, *116*, 7931.

42. Hadjiivanov, K.; Klissurski, D.; Ramis, G.; Busca, G. *Appl. Catal., B* **1996**, *7*, 251.

43. Wang, Z. L.; Liu, Q. S.; Yu, J. F.; Wu, T. H.; Wang, G. J. *Appl. Catal., A* **2003**, *239*, 87.

44. Kantcheva, M.; Sayan, S. *Catal. Lett.* **1999**, *60*, 27.

45. Scarano, D.; Bordiga, S.; Lamberti, C.; Spoto, G.; Ricchiardi, G.; Zecchina, A.; Arean, C. O. *Surf. Sci.* **1998**, *411*, 272.

46. Jiang, M.; Koizumi, N.; Ozaki, T.; Yamada, M. *Appl. Catal., A* **2001**, *209*, 59.

47. Kadinov, G.; Bonev, C.; Todorova, S.; Palazov, A. *J. Chem. Soc. Faraday T.* **1998**, *94*, 3027.

48. Rodrigues, E. L.; Bueno, J. M. C. *Appl. Catal., A* **2002**, *232*, 147.

49. Song, D.; Li, J.; Cai, Q. *J. Phys. Chem. C* **2007**, *111*, 18970.

50. Bian, G.; Nanba, T.; Koizumi, N.; Yamada, M. *J. Mol. Catal. A: Chem.* **2002**, *178*, 219.

51. Khodakov, A. Y.; Lynch, J.; Bazin, D.; Rebours, B.; Zanier, N.; Moisson, B.; Chaumette, P. *J. Catal.* **1997**, *168*, 16.

52. Pick, S. *Surf. Sci.* **2007**, *601*, 5571.

53. Prieto, G.; Martínez, A.; Concepción, P.; Moreno-Tost, R. *J. Catal.* **2009**, *266*, 129.

54. Mendes, F. M. T.; Perez, C. A. C.; Noronha, F. B.; Souza, C. D. D.; Cesar, D. V.; Freund, H. J.; Schmal, M. *J. Phys. Chem. B* **2006**, *110*, 9155.

55. Xiong, H.; Zhang, Y.; Liew, K.; Li, J. *J. Mol. Catal. A: Chem.* **2008**, *295*, 68.

56. Lapidus, A.; Krylova, A.; Kazanskii, V.; Borovkov, V.; Zaitsev, A.; Rathousky, J.; Zukal, A.; Jancalkova, M. *Appl. Catal.* **1991**, *73*, 65.

57. Zhang, J.; Chen, J.; Ren, J.; Sun, Y. *Appl. Catal., A* **2003**, *243*, 121.

58. Venugopal, A.; Aluha, J.; Scurrell, M. S. *Catal. Lett.* **2003**, *90*, 1.

59. Kumar, N.; Jothimurugesan, K.; Stanley, G. G.; Schwartz, V.; Spivey, J. J. *J. Phys. Chem. C* **2010**, *115*, 990.

Chapter 6: Conclusions and Future Work

6.1. Conclusions

6.1.1. Role of Tin

Tin functions as a dispersant for copper and cobalt species. The increased dispersion in turn increases the reducibility of copper and decreases that of cobalt. On well-reduced catalysts ($CuSn/SiO_2$ and $CuCoSn/SiO_2$), the smaller particle size translates into increased CO uptakes. With tin addition, new CO species adsorbed on tin-interacting copper sites are observed by DRIFTS. On cobalt, linear CO adsorbs more strongly when tin is present. In CO hydrogenation, tin addition decreases CO conversion and shifts selectivity toward lighter products by depressing chain growth of surface hydrocarbons.

6.1.2. Role of Copper

The primary role of copper is to promote cobalt reduction. An unintended consequence is that substantial tin reduction also takes place when copper is present. The increased degree of reduction increases the binding strength of CO to cobalt, which makes associative and dissociative CO adsorption more likely to occur at the same cobalt sites. Thus, ethanol selectivity is higher on $CuCo/SiO_2$ than on Co/SiO_2. Copper also suppresses deactivation of cobalt sites.

CO adsorbed on the copper sites tends to desorb below CO hydrogenation temperatures, though Sn stabilizes it somewhat. Moreover, the CO conversions of Cu/SiO_2 and $CuSn/SiO_2$ are lower than those of the corresponding cobalt-containing catalysts. These results suggest that copper plays a secondary role to cobalt in CO hydrogenation.

6.1.3. Role of Cobalt

Cobalt is the main active component, on which elementary steps such as CO adsorption, dissociation, and insertion take place. Simplified schemes showing the essential structural and reductive properties of cobalt, as influenced by the presence of copper and tin, are shown in Figure 6.1. In Co/SiO_2, the calcination produces Co_3O_4 crystallites, which convert to CoO during reduction; this intermediate partially reduces to Co^0 during the typical H_2 pretreatment at 400°C. Upon addition of tin ($CoSn/SiO_2$ and $CuCoSn/SiO_2$), relatively smaller particles of a cobalt-tin mixed spinel phase, Co_2SnO_4, form in addition to Co_3O_4. These highly dispersed Co_2SnO_4 particles show increased stability towards reduction. In particular, no evidence of metallic cobalt is observed after reduction of $CoSn/SiO_2$ at 400°C. Copper addition ($CuCo/SiO_2$) accelerates reduction of Co^{2+} species in particular, such that complete conversion to Co^0 is achieved with the standard pretreatment. Copper also counteracts the tendency of tin to stabilize cobalt against reduction. The combined effects of copper and tin ensure that cobalt is both well reduced and highly dispersed on $CuCoSn/SiO_2$.

The presence of additives influences the electronic state of cobalt, which in turn affects the strength of the cobalt-CO bond (Table 6.1). For example, weak molecular adsorption of CO takes place mainly on $Co^{\delta+}$ sites on Co/SiO_2. This catalyst gives high oxygenate yields but low selectivity due to the fact that these $Co^{\delta+}$ sites are not necessarily in atomic proximity to the sites responsible for direct CO dissociation. CO adsorbs more strongly on the well-reduced Co^0 sites of $CuCo/SiO_2$ and $CuCoSn/SiO_2$. This alters the balance and proximity between associatively and dissociatively adsorbed CO in a way that favors CO insertion and selective formation of ethanol.

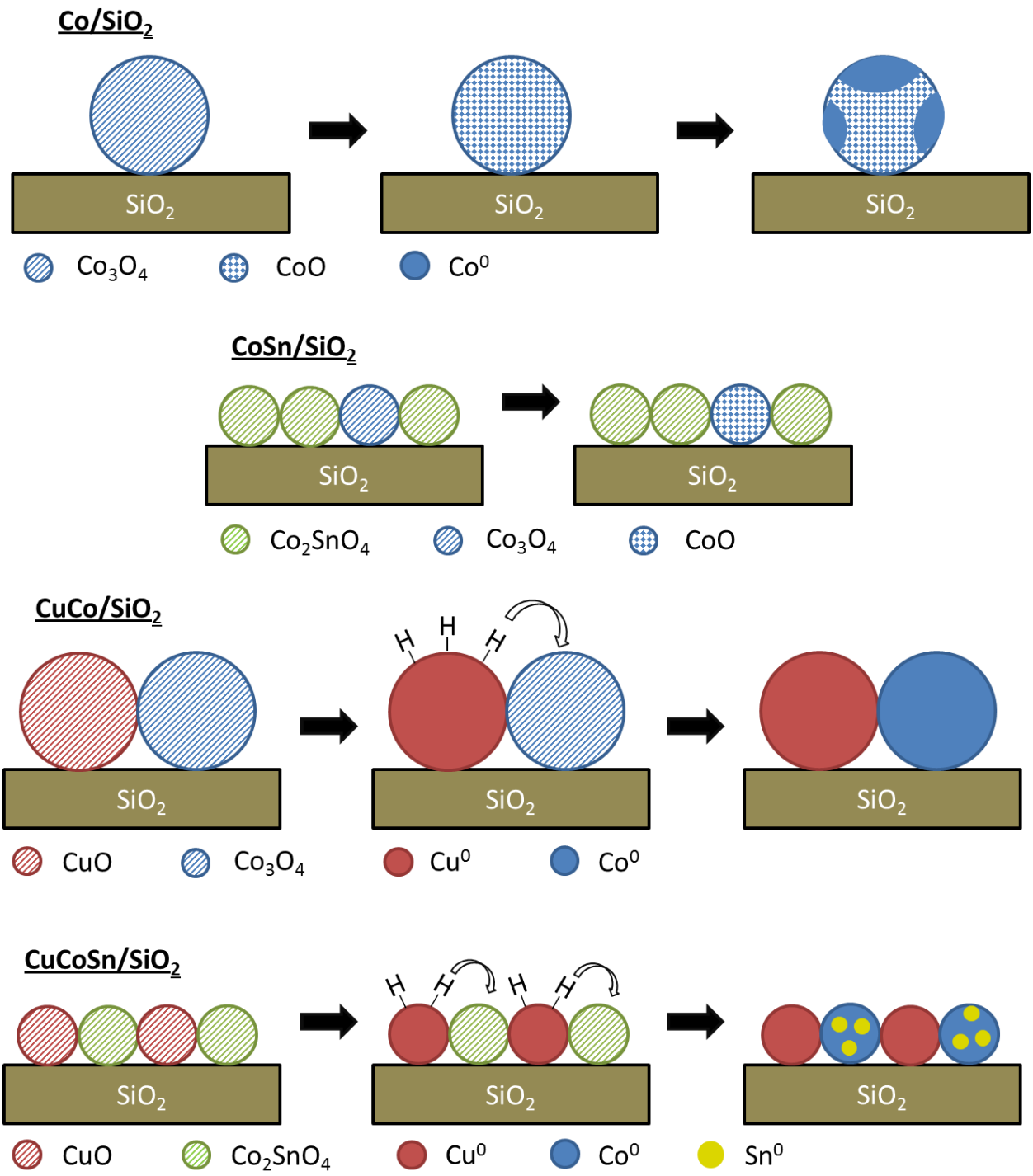

Figure 6.1. Schemes representing reduction of Co/SiO_2, $CoSn/SiO_2$, $CuCo/SiO_2$, and $CuCoSn/SiO_2$ (top to bottom). In each scheme, the calcined state of the catalyst is illustrated at the left, and the state after reduction at 400°C is shown at the right.

The high dispersion and increased population of linearly adsorbed CO on $CuCoSn/SiO_2$ tend to isolate dissociated CO from like species; this contributes to increased ethanol selectivity and reduced C_{2+} hydrocarbon selectivity on this catalyst compared to $CuCo/SiO_2$.

Addition of copper or tin reduces the activity of cobalt for CO hydrogenation. One reason is that Co/SiO_2 contains sites capable of direct CO dissociation and very active for formation of hydrocarbons; these sites are blocked or prevented from forming by copper and tin.

Table 6.1. Summary of the effects of copper and tin addition on cobalt dispersion, reducibility, and CO adsorption sites.

Catalyst	Structure after reduction at 400°C	CO adsorption on the active sites
Co/SiO_2	Low dispersion Partial reduction to Co^0	Linear CO on $Co^{\delta+}$ Dissociated CO on unique Co^0 sites (e.g., coordinatively unsaturated ones)
$CoSn/SiO_2$	High dispersion No reduction to Co^0	No CO adsorbed
$CuCo/SiO_2$	Low dispersion Complete reduction to Co^0	Linear CO on Co^0 Dissociated CO on Co^0
$CuCoSn/SiO_2$	High dispersion Complete reduction to Co^0	Linear CO on Co^0 Dissociated CO on Co^0

6.2. Future Work

6.2.1. Optimization of the Catalyst Composition

Because cobalt is the most active component of the copper-cobalt-tin system, the key to boosting activity appears to be raising the proportion of cobalt relative to copper and tin. The composition needs to be chosen so that the high dispersion and reducibility of cobalt are maintained.

The dramatic promotion of reduction by copper causes complete reduction of both cobalt and tin in $CuCoSn/SiO_2$. When copper is excluded ($CoSn/SiO_2$), cobalt and tin are prevented from reducing by the strong interaction between them. This interaction is demonstrated by XANES. Thus, Sn and Co in these catalysts are either totally reduced or totally oxidized. The intended combination of Co^0 and $Sn^{\delta+}$ it seems could not be prepared using these compositions. In order to generate these sites, the copper-to-cobalt ratio in $CuCoSn/SiO_2$ could be reduced.

Tin could also be replaced by other oxophilic promoters that could be expected to promote CO dissociation and insertion. For example, ZrO_2 acts as both a rate promoter and a chain growth promoter when added to Co/SiO_2 Fischer-Tropsch catalysts[1-3], though in these studies, the higher alcohols were not quantified. However, the use of ZrO_2 as a support results in increased higher alcohol selectivity compared to such materials as MgO, La_2O_3, CeO_2, and TiO_2[4,5].

6.2.2. High Pressure Activity, Selectivity, and DRIFTS Studies

DRIFTS studies conducted at 10 bar would allow for a more direct comparison with the activity/selectivity results at the same pressure. Moreover, the higher pressure might allow for the formation of alcohols in quantities detectable by the associated MS. Correlating this

information with the DRIFTS results might provide further insight into the origin of these oxygenates.

The effect of pressure on CO conversion and ethanol selectivity is another potential avenue for research. This and other process variables (space velocity, feed ratio, etc.) need further study, particularly for the tin-containing catalysts, which are not well known.

6.3. References

1. Ali, S.; Chen, B.; Goodwin, J. G. *J. Catal.* **1995**, *157*, 35.
2. Feller, A.; Claeys, M.; van Steen, E. *J. Catal.* **1999**, *185*, 120.
3. Moradi, G. R.; Basir, M. M.; Taeb, A.; Kiennemann, A. *Catal. Commun.* **2003**, *4*, 27.
4. Mouaddib, N.; Perrichon, V.; Primet, M. *J. Chem. Soc. Faraday T. 1* **1989**, *85*, 3413.
5. Mouaddib, N.; Perrichon, V.; Martin, G. A. *Appl. Catal., A* **1994**, *118*, 63.

Appendix A: Permission to Use Copyrighted Materials

A.1. Permission to Use Figure 2.1

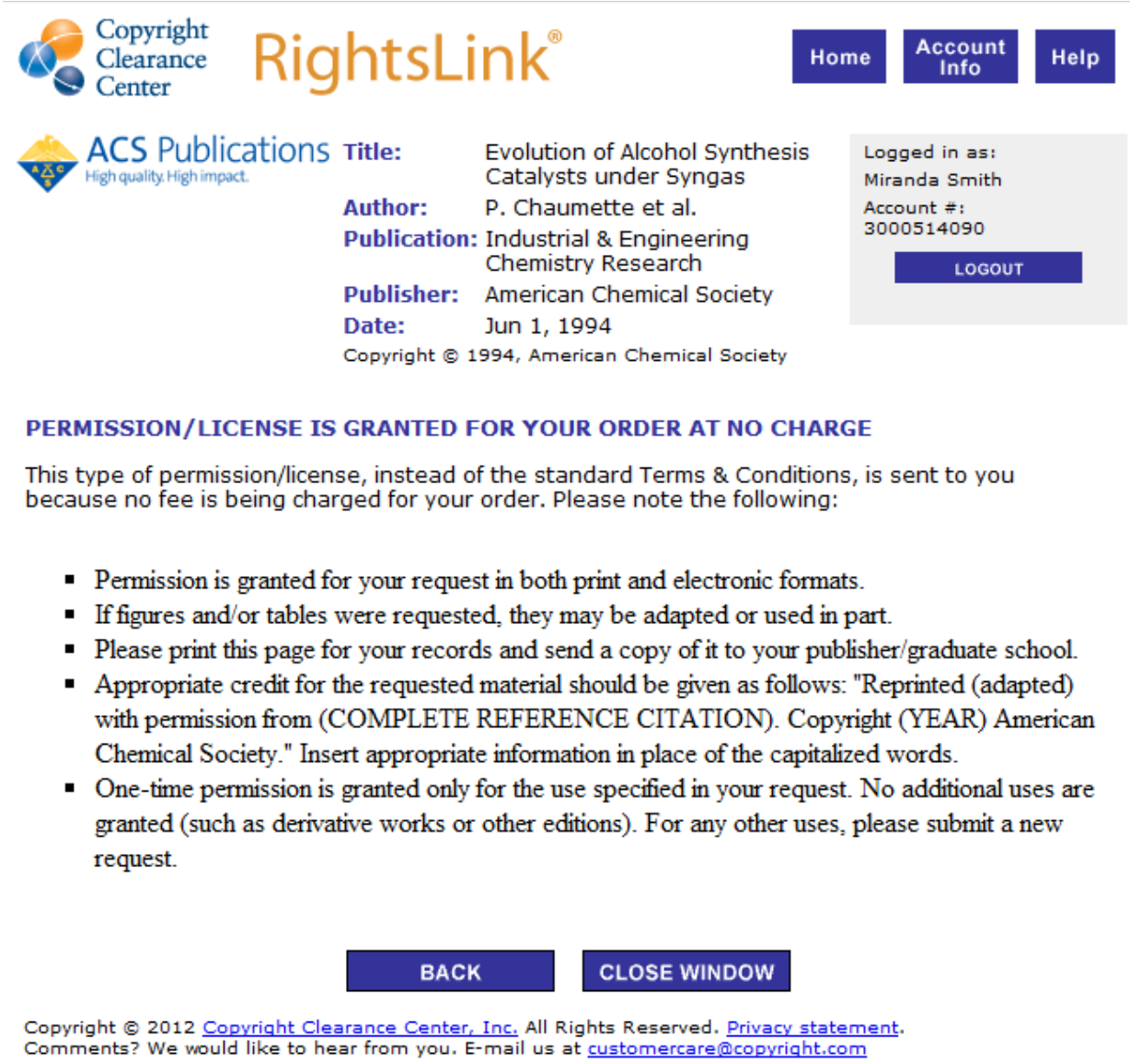

Copyright Clearance Center RightsLink®

Home | Account Info | Help

ACS Publications
High quality. High impact.

Title: Evolution of Alcohol Synthesis Catalysts under Syngas
Author: P. Chaumette et al.
Publication: Industrial & Engineering Chemistry Research
Publisher: American Chemical Society
Date: Jun 1, 1994
Copyright © 1994, American Chemical Society

Logged in as:
Miranda Smith
Account #:
3000514090
LOGOUT

PERMISSION/LICENSE IS GRANTED FOR YOUR ORDER AT NO CHARGE

This type of permission/license, instead of the standard Terms & Conditions, is sent to you because no fee is being charged for your order. Please note the following:

- Permission is granted for your request in both print and electronic formats.
- If figures and/or tables were requested, they may be adapted or used in part.
- Please print this page for your records and send a copy of it to your publisher/graduate school.
- Appropriate credit for the requested material should be given as follows: "Reprinted (adapted) with permission from (COMPLETE REFERENCE CITATION). Copyright (YEAR) American Chemical Society." Insert appropriate information in place of the capitalized words.
- One-time permission is granted only for the use specified in your request. No additional uses are granted (such as derivative works or other editions). For any other uses, please submit a new request.

BACK | CLOSE WINDOW

Copyright © 2012 Copyright Clearance Center, Inc. All Rights Reserved. Privacy statement.
Comments? We would like to hear from you. E-mail us at customercare@copyright.com

A.2. Permission to Use Figure 2.2

SPRINGER LICENSE
TERMS AND CONDITIONS

Apr 15, 2012

This is a License Agreement between Miranda L Smith ("You") and Springer ("Springer") provided by Copyright Clearance Center ("CCC"). The license consists of your order details, the terms and conditions provided by Springer, and the payment terms and conditions.

All payments must be made in full to CCC. For payment instructions, please see information listed at the bottom of this form.

License Number	2890221449629
License date	Apr 15, 2012
Licensed content publisher	Springer
Licensed content publication	Catalysis Letters
Licensed content title	Higher Alcohol Synthesis over a K-Promoted Co_2O_3/CuO/ZnO/Al_2O_3 Catalyst
Licensed content author	Ismail Boz
Licensed content date	Apr 1, 2003
Volume number	87
Issue number	3
Type of Use	Thesis/Dissertation
Portion	Figures
Author of this Springer article	No
Order reference number	
Title of your thesis / dissertation	COPPER-COBALT CATALYSTS FOR CONVERSION OF SYNGAS TO ETHANOL AND HIGHER ALCOHOLS
Expected completion date	Aug 2012
Estimated size(pages)	150
Total	0.00 USD

A.3. Permission to Use Figure 2.3

ELSEVIER LICENSE
TERMS AND CONDITIONS

Apr 15, 2012

This is a License Agreement between Miranda L Smith ("You") and Elsevier ("Elsevier") provided by Copyright Clearance Center ("CCC"). The license consists of your order details, the terms and conditions provided by Elsevier, and the payment terms and conditions.

All payments must be made in full to CCC. For payment instructions, please see information listed at the bottom of this form.

Supplier	Elsevier Limited The Boulevard,Langford Lane Kidlington,Oxford,OX5 1GB,UK
Registered Company Number	1982084
Customer name	Miranda L Smith
Customer address	110 Chemical Engineering Baton Rouge, LA 70803
License number	2890231442588
License date	Apr 15, 2012
Licensed content publisher	Elsevier
Licensed content publication	Applied Catalysis A: General
Licensed content title	Conversion of syngas to C1-C6alcohol mixtures on promoted CuLa2Zr2O7catalysts
Licensed content author	Wey Chu,Roger Kieffer,Alain Kiennemann,Jean Paul Hindermann
Licensed content date	5 January 1995
Licensed content volume number	121
Licensed content issue number	1
Number of pages	17
Start Page	95
End Page	111
Type of Use	reuse in a thesis/dissertation
Intended publisher of new work	other
Portion	figures/tables/illustrations
Number of figures/tables/illustrations	1

Format	both print and electronic
Are you the author of this Elsevier article?	No
Will you be translating?	No
Order reference number	
Title of your thesis/dissertation	COPPER-COBALT CATALYSTS FOR CONVERSION OF SYNGAS TO ETHANOL AND HIGHER ALCOHOLS
Expected completion date	Aug 2012
Estimated size (number of pages)	150
Elsevier VAT number	GB 494 6272 12
Permissions price	0.00 USD
VAT/Local Sales Tax	0.0 USD / 0.0 GBP
Total	0.00 USD

A.4. Permission to Use Chapter 3

ELSEVIER LICENSE
TERMS AND CONDITIONS

Mar 23, 2012

This is a License Agreement between Miranda L Smith ("You") and Elsevier ("Elsevier") provided by Copyright Clearance Center ("CCC"). The license consists of your order details, the terms and conditions provided by Elsevier, and the payment terms and conditions.

All payments must be made in full to CCC. For payment instructions, please see information listed at the bottom of this form.

Supplier	Elsevier Limited The Boulevard,Langford Lane Kidlington,Oxford,OX5 1GB,UK
Registered Company Number	1982084
Customer name	Miranda L Smith
Customer address	110 Chemical Engineering Baton Rouge, LA 70803

License number	2874840570845
License date	Mar 23, 2012
Licensed content publisher	Elsevier
Licensed content publication	Catalysis Today
Licensed content title	Reduction processes in Cu/SiO2, Co/SiO2, and CuCo/SiO2catalysts
Licensed content author	Miranda L. Smith,Andrew Campos,James J. Spivey
Licensed content date	17 March 2012
Licensed content volume number	182
Licensed content issue number	1
Number of pages	7
Start Page	60
End Page	66
Type of Use	reuse in a thesis/dissertation
Portion	full article
Format	both print and electronic
Are you the author of this Elsevier article?	Yes
Will you be translating?	No
Order reference number	
Title of your thesis/dissertation	COPPER-COBALT CATALYSTS FOR CONVERSION OF SYNGAS TO ETHANOL AND HIGHER ALCOHOLS
Expected completion date	Aug 2012
Estimated size (number of pages)	150
Elsevier VAT number	GB 494 6272 12
Permissions price	0.00 USD
VAT/Local Sales Tax	0.0 USD / 0.0 GBP
Total	0.00 USD

A.5. Permission to Use Chapter 4

Home | Account Info | Help

Title: CO Adsorption Behavior of Cu/SiO2, Co/SiO2, and CuCo/SiO2 Catalysts Studied by in Situ DRIFTS

Author: Miranda L. Smith et al.

Publication: The Journal of Physical Chemistry C

Publisher: American Chemical Society

Date: Apr 1, 2012

Logged in as:
Miranda Smith
Account #:
3000514090

LOGOUT

PERMISSION/LICENSE IS GRANTED FOR YOUR ORDER AT NO CHARGE

This type of permission/license, instead of the standard Terms & Conditions, is sent to you because no fee is being charged for your order. Please note the following:

- Permission is granted for your request in both print and electronic formats.
- If figures and/or tables were requested, they may be adapted or used in part.
- Please print this page for your records and send a copy of it to your publisher/graduate school.
- Appropriate credit for the requested material should be given as follows: "Reprinted (adapted) with permission from (COMPLETE REFERENCE CITATION). Copyright (YEAR) American Chemical Society." Insert appropriate information in place of the capitalized words.
- One-time permission is granted only for the use specified in your request. No additional uses are granted (such as derivative works or other editions). For any other uses, please submit a new request.

BACK | CLOSE WINDOW

Appendix B: Proof of Principal Authorship

B.1. Chapter 3

Catalysis Today 182 (2012) 60–66

Contents lists available at ScienceDirect

Catalysis Today

journal homepage: www.elsevier.com/locate/cattod

Reduction processes in Cu/SiO_2, Co/SiO_2, and $CuCo/SiO_2$ catalysts

Miranda L. Smith, Andrew Campos, James J. Spivey*

Cain Department of Chemical Engineering, Louisiana State University, 110 Chemical Engineering, South Stadium Rd., Baton Rouge, LA 70803, USA

ARTICLE INFO

Article history:
Received 10 May 2011
Accepted 10 July 2011
Available online 16 September 2011

Keywords:
XANES
XRD
TPR
Copper
Cobalt
Reduction

ABSTRACT

Cu/SiO_2, Co/SiO_2, and bimetallic $CuCo/SiO_2$ catalysts have been synthesized and their reduction behavior characterized by TPR, *in situ* XRD, and *in situ* XANES. In Cu/SiO_2, a two step reduction process, $CuO \rightarrow Cu_2O \rightarrow Cu^0$, occurred. Two forms of the intermediate Cu_2O with different degrees of reducibility were observed. Addition of cobalt to Cu/SiO_2 resulted in formation of an amorphous fraction of CuO that was more easily reducible than crystalline CuO. Cobalt addition also prevented formation of the less reducible form of Cu_2O. Addition of copper to Co/SiO_2 increased the reducibility of Co_3O_4, and to greater extent of the intermediate CoO, which in the monometallic Co/SiO_2 was less readily reduced due to interaction with the support.

1. Introduction

Catalysts based on copper and cobalt have been studied for hydrogenation of CO to mixtures of ethanol and higher alcohols. This reaction is thought to occur by a dual site mechanism: CO associatively adsorbed on one type of site is inserted into surface hydrocarbon species arising from CO dissociation on the other site [1,2]. Hydrogenation of the resulting intermediate yields the alcohol. The site pairs mainly responsible for alcohol synthesis are often proposed to be Cu^0 and Co^0 in close interaction or proximity [1,3,4], but have occasionally been identified as $Co^0/Co^{\delta+}$ pairs, with copper maintaining this state of reduction [5]. In fact, the nature of the active centers may depend on the activation conditions applied to the catalyst [6]. Therefore, it is important to understand reduction processes in both copper–cobalt catalysts and their monometallic counterparts.

Bulk unsupported CuO normally reduces in a single step to Cu^0, without formation of a Cu_2O intermediate [7,8]. Copper oxide becomes reducible at lower temperature when supported on silica than when unsupported, due to increased dispersion and greater reactivity toward H_2 [9–11]. Sometimes multiple peaks are observed during temperature programmed reduction (TPR) of Cu/SiO_2 catalysts. In such cases, some authors associate the lower temperature peak with reduction of a CuO phase of low crystallinity and small particle size, presumably forming Cu^0 directly [11–14]. Others claim small CuO particles should interact with SiO_2, hindering reduction [10]. Moreover, if the area ratio of these TPR peaks is ~1:1, then the possibility of a sequential reduction, $CuO \rightarrow Cu_2O \rightarrow Cu$, must also be considered.

Co/SiO_2 catalysts typically reduce in two steps: $Co_3O_4 \rightarrow CoO \rightarrow Co^0$ [15–17]. The second step, in particular, is impeded by support interactions that become important when the particle size is small [15]. Divalent cobalt species show increasing difficulty of reduction in the following order: Co^{2+} with little support interaction, Co^{2+} having slightly stronger interaction with SiO_2, cobalt hydrosilicates, and cobalt silicate [16]. Cobalt silicate, which is favored by high-pH preparation conditions, shows a TPR maximum at about 900 °C [16].

TPR of unsupported, coprecipitated, air-calcined oxides of cobalt and copper shows that the presence of copper promotes the reduction of Co_3O_4 [18]. $CuCo/SiO_2$ catalysts usually show a single TPR peak at lower temperature than is typical for reduction of cobalt oxides [19–21]. Different authors have assumed a strong interaction between CuO and Co_3O_4 [18,19,21] or even formation of a $Cu_xCo_{3-x}O_4$ phase [18,20] to explain the promoting effect of copper on cobalt reduction.

Catalyst reduction pathways depend on preparation method, thermal treatment, and metal loading and can be quite complex even in monometallic systems. Addition of a second metal complicates the system even further. Therefore, a thorough characterization of the activation process is a prerequisite for understanding the nature of active species in each catalyst. The objective of this work is to apply complementary characterization techniques (TPR, *in situ* XRD, and *in situ* XANES) to study the effects of copper and cobalt upon each other during reduction of SiO_2-supported catalysts.

* Corresponding author. Tel.: +1 225 578 3690; fax: +1 225 578 1476.
E-mail address: jjspivey@lsu.edu (J.J. Spivey).

0920-5861/$ – see front matter © 2011 Elsevier B.V. All rights reserved.
doi:10.1016/j.cattod.2011.07.026

B.2. Chapter 4

THE JOURNAL OF PHYSICAL CHEMISTRY C

Article

pubs.acs.org/JPCC

CO Adsorption Behavior of Cu/SiO_2, Co/SiO_2, and $CuCo/SiO_2$ Catalysts Studied by in Situ DRIFTS

Miranda L. Smith, Nitin Kumar, and James J. Spivey*

Cain Department of Chemical Engineering, Louisiana State University, 110 Chemical Engineering, South Stadium Road, Baton Rouge, Louisiana 70803, United States

ABSTRACT: The mode of CO adsorption is an important factor in directing the selectivity of CO hydrogenation toward methanol, hydrocarbons, or higher alcohols. Here, we report results on three catalysts: Cu/SiO_2, Co/SiO_2, and $CuCo/SiO_2$. Infrared spectroscopic studies on Cu/SiO_2 and $CuCo/SiO_2$ show similar CO adsorption behavior on copper sites, in terms of adsorption frequency and stability, regardless of the presence or absence of cobalt. The CO species adsorbing on copper is not thermally stable at typical CO hydrogenation reaction temperatures. For CO to adsorb on cobalt sites on either Co/SiO_2 or $CuCo/SiO_2$, temperatures above ambient are required. In general, linearly adsorbed CO binds more strongly to the cobalt sites of $CuCo/SiO_2$ than of Co/SiO_2. Thus, on $CuCo/SiO_2$, CO is more likely to dissociate at the same sites where it linearly adsorbs, leading to increased probability of CO insertion and ethanol formation. A second type of site on Co/SiO_2 is responsible for direct CO dissociation, leading to high activity and hydrocarbon selectivity on this catalyst, as well as faster deactivation.

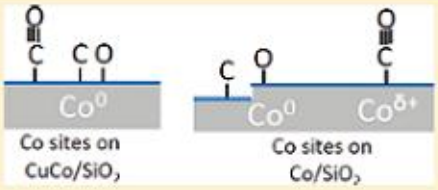

1. INTRODUCTION

The reaction of syngas to produce ethanol and higher alcohols is a possible route for converting a variety of feedstocks to useful transportation fuels and fuel additives. An active, selective catalyst is necessary. Since their inception in the early 1980s,[1] catalysts based on copper and cobalt have received continuing attention for this reaction.[2−10] These modified Fischer−Tropsch catalysts are attractive because they mimic the mechanism of the highly ethanol-selective Rh-based catalysts[11] but have a lower cost.

The mechanism of higher alcohol synthesis on copper−cobalt catalysts requires one site capable of CO dissociation and chain growth, together with a site that adsorbs CO molecularly.[12,13] C−C bond formation between a surface hydrocarbon group and adsorbed CO forms the surface intermediate leading to higher alcohols. However, direct hydrogenation of the adsorbed C_xH_y or CO species, without coupling of the two, yields hydrocarbons or methanol, respectively.

Most literature dealing with the active sites of copper−cobalt catalysts assigns cobalt as the site for CO dissociation and copper as the main site for molecular adsorption and CO insertion.[14−17] A few studies[18,19] have also proposed that Co^0/Co^{n+} are appropriate site pairs.

Fourier transform infrared (FTIR) spectroscopy is particularly well suited to study the interaction of CO with a catalyst surface. This technique has been applied to CO adsorption on copper−cobalt catalysts.[17,20−23] These past studies usually aimed at identifying the types of surface sites on the catalyst. For example, a shift in the frequencies of CO adsorbed on copper and cobalt in opposite directions upon combining these elements has been taken as evidence for a CuCo surface alloy.[17]

The usual approach in such experiments is to collect spectra of the irreversibly adsorbed species after carefully controlled CO dosing at ambient or subambient temperature, followed by evacuation or flushing with subsequent heating.[17,20−23] The advantages of this procedure are (1) reduction of the spectral contribution of the gas phase CO signal and (2) minimization of coverage effects on the vibrational frequency of adsorbed CO. However, these conditions are necessarily far removed from the working environment of the catalyst.

The application of FTIR spectroscopy to study the direct exposure of a catalyst to syngas is rarely reported,[24−26] still less so for copper−cobalt systems.[25] Considering the important role of the CO adsorption mode in directing the selectivity of the reaction, it would be instructive to follow by FTIR the effects of adsorption and changing reaction conditions on the CO bond, instead of using the technique *exclusively* as a site probe.

The objectives of this work are to study the effect of combining copper and cobalt on CO adsorption under syngas flow at different temperatures and to relate this information to the activity/selectivity of the catalysts.

2. EXPERIMENTAL METHODS

2.1. Catalyst Preparation. The catalysts (Cu/SiO_2, Co/SiO_2, and $CuCo/SiO_2$) were prepared by the incipient wetness technique. Nitrate precursors in aqueous solution were used. The catalysts were dried overnight at 100−105 °C and calcined in a tube furnace at 500 °C (after ramping at 4 °C/min from room temperature) for 2 h.

Received: February 6, 2012
Published: March 12, 2012

Appendix C: Instrumentation of AMI 200R-HP Reactor and Shimadzu GC-2014

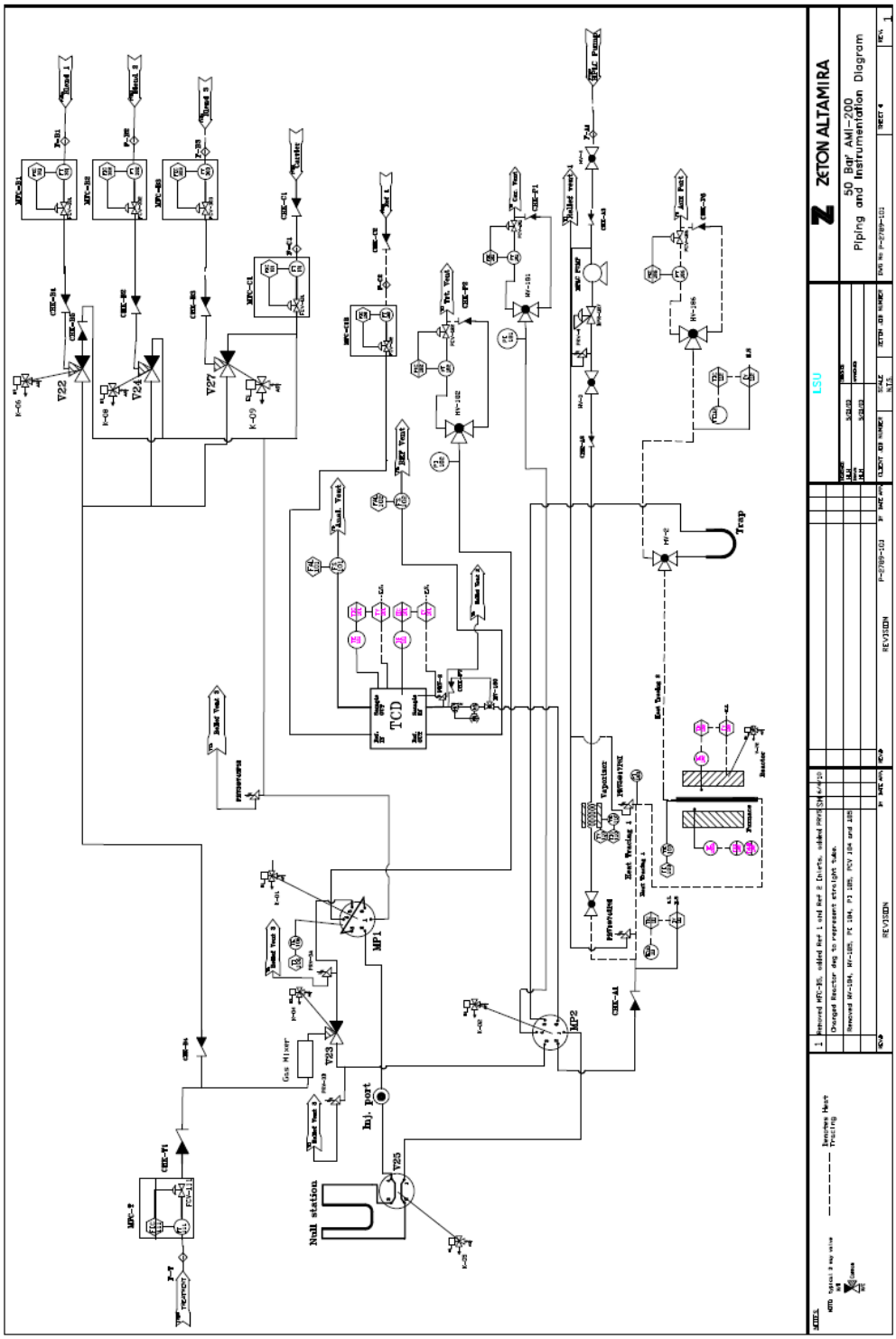

Figure C.1. Piping and instrumentation diagram of the AMI-200R-HP.

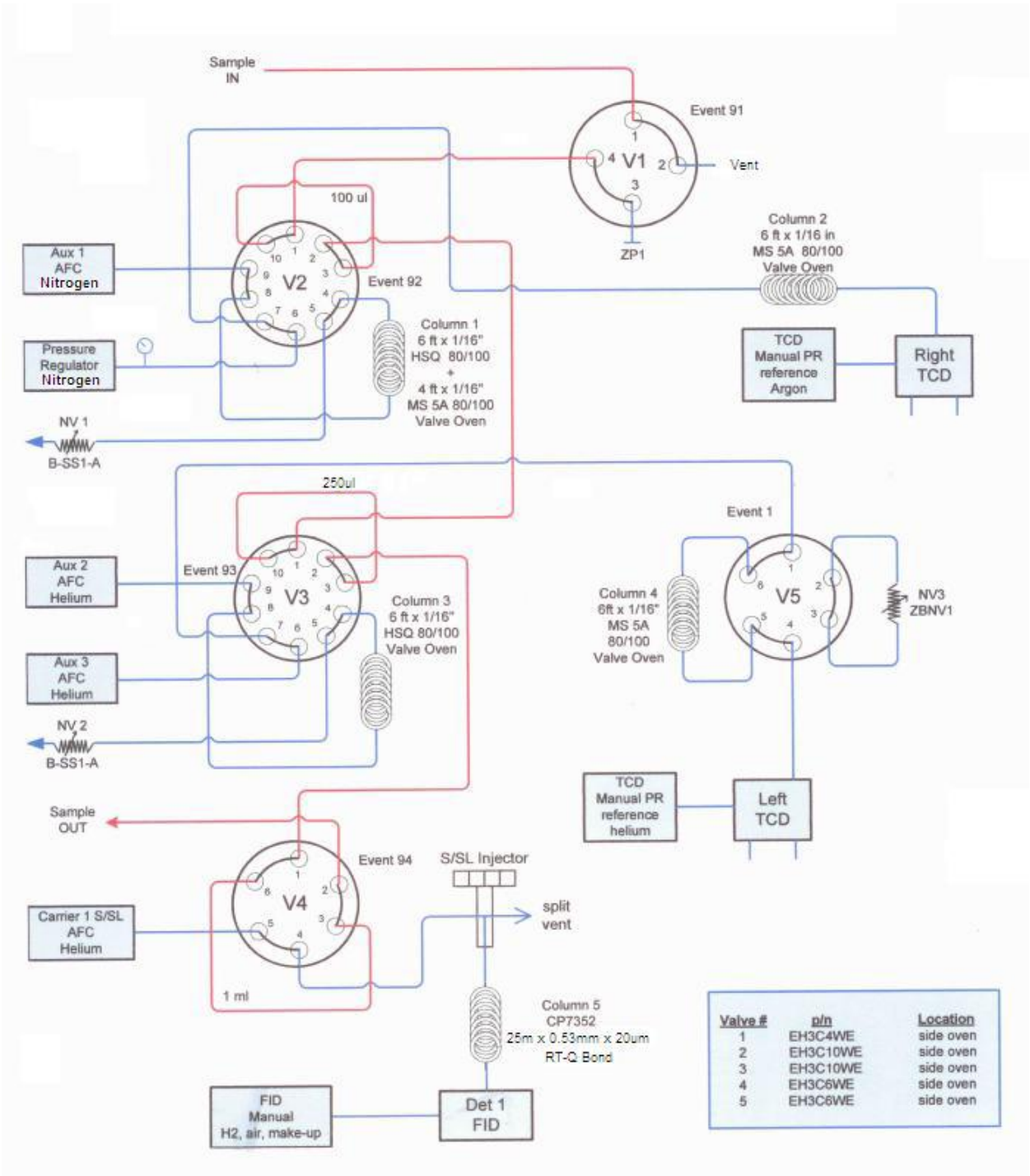

Figure C.2. Plumbing diagram of the Shimadzu GC-2014 GC/TCD/FID.

Table C.1. Settings applied to the split/splitless injector (operated in split mode) of the Shimadzu GC-2014.

Temperature	200°C
Pressure	6.1 psi
Total Flow	49.7 mL/min
Column Flow	8.11 mL/min
Linear Velocity	61.7 cm/s
Split Ratio	5.0

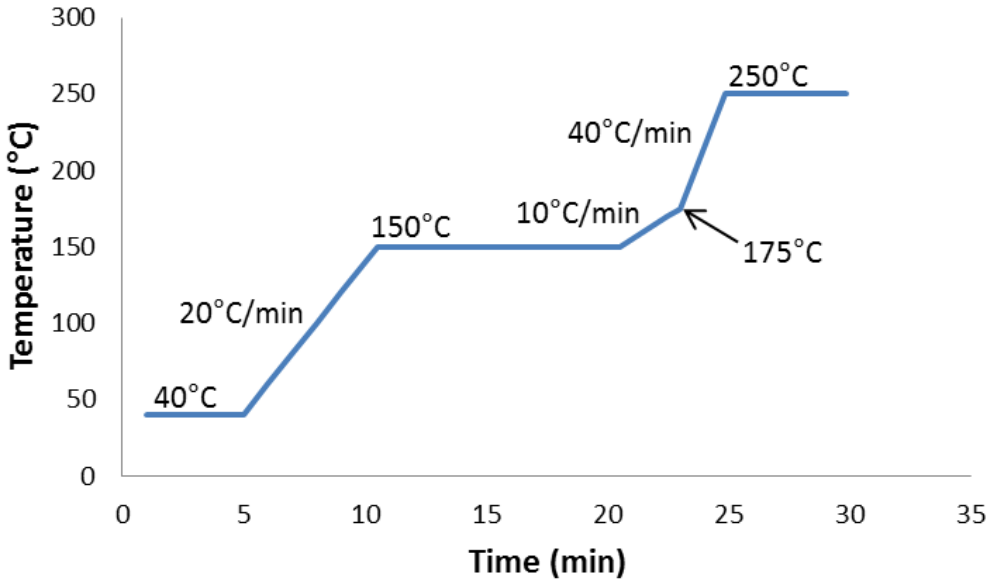

Figure C.3. Timed temperature program for the GC-2014 oven, which houses the Restek Rt®-Q-BOND column (25 m × 0.53 mm × 20 µm), which is connected to the FID.

Table C.2. Detector settings for the Shimadzu GC-2014.

	FID	Left TCD	Right TCD
Temperature	250°C	250°C	250°C
Sampling Rate	40 msec	240 msec	240 msec
Current	--	100 mA	40 mA

Vita

Miranda Smith is a native of Pearl River, Louisiana. She earned a Bachelor of Science in Chemical Engineering from Mississippi State University in 2008. She is pursuing a Doctor of Philosophy in Chemical Engineering at Louisiana State University for work on CO hydrogenation to ethanol and higher alcohols. She expects to graduate in August 2012.